STARS

Electronic Theses and Dissertations, 2004-2019

2007

Discrete Surface Solitons

Sergiy Suntsov
University of Central Florida

DISCRETE SURFACE SOLITONS

by

SERGIY SUNTSOV
B.S. Kiev National Taras Shevchenko University, Kiev, 1993
M.S. University of Central Florida, 2007

A dissertation submitted in partial fulfillment of the requirements
for the degree of Doctor of Philosophy
in the College of Optics and Photonics
at the University of Central Florida
Orlando, Florida

Spring Term
2008

Major Professor: George I. Stegeman

ABSTRACT

Surface waves exist along the interfaces between two different media and are known to display properties that have no analogue in continuous systems. In years past, they have been the subject of many studies in a diverse collection of scientific disciplines. In optics, one of the mechanisms through which optical surface waves can exist is material nonlinearity. Until recently, most of the activity in this area was focused on interfaces between continuous media but no successful experiments have been reported. However, the growing interest that nonlinear discrete optics has attracted in the last two decades has raised the question of whether nonlinear surface waves can exist in discrete optical systems.

In this work, a detailed experimental study of linear and nonlinear optical wave propagation at the interface between a discrete one-dimensional Kerr-nonlinear system and a continuous medium (slab waveguide) as well as at the interface between two dissimilar waveguide lattices is presented.

The major part of this dissertation is devoted to the first experimental observation of discrete surface solitons in AlGaAs Kerr-nonlinear arrays of weakly coupled waveguides. These nonlinear surface waves are found to localize in the channels at and near the boundary of the waveguide array. The key unique property of discrete surface solitons, namely the existence of a power threshold, is investigated in detail.

The second part of this work deals with the linear light propagation properties at the interface between two dissimilar waveguide arrays (so-called waveguide array hetero-junction).

The possibility of three different types of linear interface modes is theoretically predicted and the existence of one of them, namely the staggered/staggered mode, is confirmed experimentally.

The last part of the dissertation is dedicated to the investigation of the nonlinear properties of AlGaAs waveguide array hetero-junctions. The predicted three different types of discrete hybrid surface solitons are analyzed theoretically. The experimental results on observation of in-phase/in-phase hybrid surface solitons localized at channels on either side of the interface are presented and different nature of their formation is discussed.

ACKNOWLEDGMENTS

A work such as this could not have been completed or even attempted without help and support of numerous people.

First I would like to express my deepest appreciation to my advisor, Professor George Stegeman, for introducing me to the exciting world of nonlinear optics and for giving me the opportunity to conduct this research in some of the best labs; for his endless optimism; for standing by and believing in me during difficult times I sometimes had; for teaching me to see new interesting things in what I considered unimportant.

I am grateful to Professor Demetrios Christodoulides for his invaluable scientific help and motivation. Our discussions have given me a great deal of understanding of physics behind many optics phenomena.

My special thanks go to Roberto Morandotti, Greg Salamo, Marc Sorel, Richard Arès and their research groups for providing the great AlGaAs samples which made this work possible.

During 4+ years here at CREOL, I had a pleasure of making many new friends. Among them, I would like to thank Ladislav for spending many hours helping to get my first experiments running and for showing me that arriving of a night time is not the reason to call it a day. I thank Kosta for valuable theoretical support and simulations, as well as for his vivid (though sometimes annoying) spirit of controversy. I will not forget Arek for the constructive time we spent in the lab and for not complaining about burnt tires during our crazy driving lessons. I thank Jorgos for introducing me to Greek songs and for keeping me awake during

afternoon hours in the office. And I thank Sergiy for his readiness to have fun without asking extra questions.

I am indebted to my friends Roman Malendevich and Sergei Krasulya whose help and persistence made my study in the U.S. possible.

I would also like to thank my other friends Alex, Toufic, Leo, Peter, David, Mike, Ramy and Tony.

Last, but not least, I would like to recognize the unending love and support of my wife, Lyuda. No doubts, my Ph.D. efforts have cost her more than they have me.

TABLE OF CONTENTS

LIST OF FIGURES

LIST OF TABLES

LIST OF ABBREVIATIONS

1D	One-dimensional
2D	Two-dimensional
2PA	Two-photon absorption
3PA	Three-photon absorption
AlGaAs	Aluminum gallium arsenide
BPM	Beam propagation method
cw	Continuous wave
DNLSE	Discrete nonlinear Schrödinger equation
FWHM	Full width at half-maximum
GaAs	Gallium arsenide
SPM	Self-phase modulation
TE	Transverse electric
TM	Transverse magnetic

CHAPTER ONE: INTRODUCTION

In the field of physics, discrete phenomena such as the interaction of the elementary particles of matter (e.g. electrons and atoms) are usually described by quantum mechanics or particle physics. However, a quantum-mechanical approach is hardly applicable to most natural phenomena which involve billions of billions of such particles. To account for all the interaction between these objects would be an impossible task even for modern state-of-art computers. Therefore, most natural phenomena are treated using the macroscopic approaches of classical physics where a particular physical system is described by means of averaged macroscopic quantities. Nevertheless, many macroscopic systems can still be described by some type of a discrete model.

The first study of discrete dynamical systems dates back to 1939 when Frenkel and Kontorova used a discrete model to describe the motion of dislocations inside a crystal [1]. Since then, discrete models have been developed for a variety of systems in the field of physics, chemistry and biology. They have been used to describe heat transfer in lattices [2, 3], to explain vibrations in crystal lattices [4, 5], to analyze the dynamics of structural phase transitions in crystals, etc. [6, 7]. In biology, discrete nonlinear models have been used to describe the contraction of proteins [8, 9], and more recently the localization and transport of vibrational energy in different systems including DNA molecules [10]. Nonlinear localization phenomena have been also predicted in atomic lattices [11, 12] and molecular chains [13]. In 2001, Abdullaev et. al. used a discrete Schrödinger-like model to predict the existence of nonlinearly

self-trapped states in Bose-Einstain condensates [14]. Their predictions have been verified experimentally soon after [15].

Discrete periodic structures are becoming progressively more important in optics since they are at the core of the fascinating optical properties of photonic crystals, photonic crystal fibers and coupled waveguide arrays [16, 17]. One of the prime examples of these systems where a discrete model can be developed is an array of weakly coupled identical waveguides. When an optical beam propagates in a waveguide array, it excites a linear superposition of the Floquet-Bloch modes of the structure [18]. Each of these bound modes has a unique propagation constant and modal profile [19]. A more simplified approach to problems in weakly coupled arrays is to utilize the fact that in the first order band most of the energy tends to localize to the higher refractive index waveguide regions. Therefore, the total optical field can be effectively decomposed into a superposition of discrete modes associated with individual channels. Moreover, it is often possible to approximate the total optical field by analyzing only the amplitude and phase of each mode [20]. The optical energy exchange between the individual waveguides occurs due to the evanescent overlap of their modal fields and is modeled by the introduction of a coupling term into the discrete evolution equations. Linear properties of light propagation in one-dimensional (1D) waveguide chains (linear discrete diffraction) were first studied theoretically by Jones in 1965 [21] and experimentally observed several years later in gallium arsenide (GaAs) waveguide arrays [22]. The study of nonlinear optical properties of waveguide arrays started in 1988 when Christodoulides and Joseph suggested the idea that light can trap itself in a nonlinear waveguide array through the Kerr nonlinear effect forming discrete soliton (DS) [23]. An example of this non-diffracting nonlinear wave is shown in Figure 1.1.
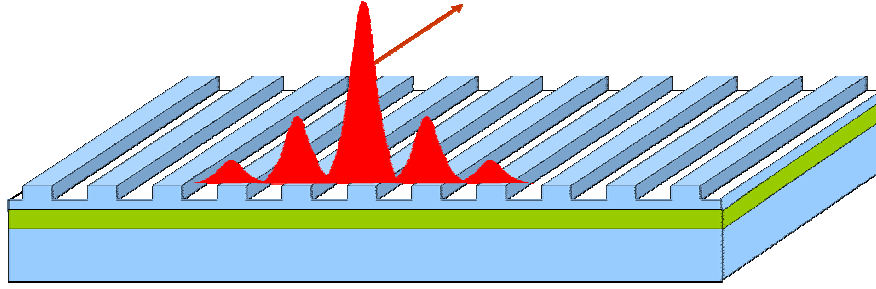
Figure 1.1: Discrete soliton in a waveguide array.

Stimulated by their work, further theoretical studies of discrete optical systems with other types of optical nonlinearity, e.g. quadratic [24], photorefractive [25], and recently more complex systems such as dissipative systems [26, 27], have been conducted. The first experimental observation of discrete solitons in Kerr media conducted by Eisenberg et. al. in 1998 [28] has triggered a wave of experimental activity in the field. To date, discrete solitons have been also experimentally observed in media with photorefractive [29], quadratic [30] and orientational nonlinearities [31].

Another class of natural phenomena that has been the subject of many studies in diverse areas of physics, chemistry and biology is surface waves [32]. In general, these waves exist along the interface between two different media and are known to display properties that have no analogue in continuous systems. Quantum surface states were first predicted in condensed matter physics by Tamm in 1932 [33]. Subsequently, Shockley has shown how such states can emerge from atomic orbitals near a surface and demonstrated that the associated surface levels can lead to surface bands in three-dimensional crystals [34, 35]. When two dissimilar semiconductor crystals are separated by an interface, new electronic states are formed in the forbidden gap between the valence and conduction bands [34]. In acoustics, an interface is well known to give rise to surface waves, in this case due to the coupling between transverse and longitudinal modes at the boundary [36]. In linear optics, perhaps the best known example of surface states are

3

surface plasmon waves, which exist at metal/dielectric interfaces [37]. In addition, Tamm-Shockley-like states were suggested in periodic layered media [38, 39] and were successfully observed in semiconductor multilayer structures [40, 41].

Material nonlinearity is another mechanism through which optical surface waves can exist [42-47]. In particular, nonlinear TE, TM, and mixed-polarization surface waves traveling along the interface between two or more dielectric interfaces were theoretically predicted and analyzed [42]. These waves are a direct outcome of nonlinearity and have no analogue whatsoever in the linear domain. They exhibit power thresholds which depend linearly on the index difference between two interfaces and require a nonlinear index change large enough to reverse the initial index contrast between the media. Nonlinear surface waves have been also studied in thin dielectric films [48] and at the interfaces between photorefractive materials [49, 50]. Yet, till recently, direct observation of nonlinear optical surface waves has been hindered by experimental difficulties such as low damage threshold of materials with high nonlinearities, compatible nonlinear media with small index differences, high losses etc. As a result, most of the activity in this area has remained theoretical.

It was recently predicted in our research group that the interface between a nonlinear waveguide array and a continuous medium can be a suitable system for the experimental observation of nonlinear surface waves, i.e. surface solitons. An example of discrete surface soliton confined to the three boundary channels is shown schematically in Figure 1.2. In such a system, the effective periodic index potential of waveguide array can be engineered with high accuracy thus greatly reducing optical power requirements and opening the horizons for the observation of a variety of new nonlinear phenomena inherent to interfaces.

4
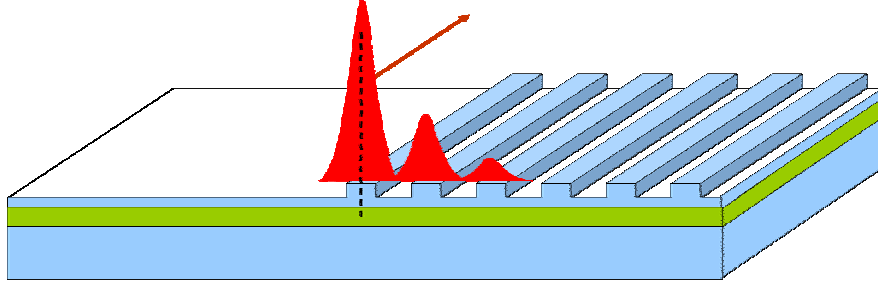
Figure 1.2: Discrete surface soliton in a semi-infinite waveguide array.

The main goal of the work presented in this dissertation was to explore experimentally for the first time surface solitons propagating along the interface between discrete and continuous media to verify theoretical predictions. These solitons were successfully demonstrated, including the family of such solitons peaked at and near the boundary, their power threshold property and the linear diffraction near the interface were studied in detail, etc.

The second goal of this work was to investigate optical modes, both linear and nonlinear (interface solitons), at the interface between two dissimilar, discrete, periodic lattices brought together to close proximity. This was again investigated successfully and both linear and nonlinear (with a power threshold) waves were identified theoretically and experimentally.

Chapter 2 of this dissertation gives a brief theoretical background necessary for understanding of linear and nonlinear wave propagation in discrete systems. In order to understand solitons at the boundaries of such discrete systems, it is first necessary to understand the linear optical properties of weakly coupled waveguides. In many ways this requires only a standard application of the usual solutions for an isolated waveguide (waveguide modes) in which light is confined in two dimensions. Here a linear array comprised of such waveguides is analyzed both via standard coupled mode theory used in integrated optics and also with Floquet-Bloch analysis borrowed from solid state physics of periodic systems. Of these, although coupled mode theory offers a great deal of insight, it is nevertheless necessary to use the Floquet-Bloch

approach to fully compare between experiment and theory. These approaches and their results are discussed in Chapter 2, including the addition of nonlinearity to predict the existence and properties of discrete surface solitons.

Fortunately AlGaAs waveguides, even in the form of coupled arrays, have been extensively studied in our group before, and the experience in dealing with them experimentally and pertinent physical data were available for the present work. Existing samples were used for the initial observation of discrete surface solitons. However, it was necessary to explore theoretically the range of sample geometries which would optimize the observations of discrete solitons at the boundary between dissimilar arrays. The details of the design, fabrication and characterization of aluminum gallium arsenide (AlGaAs) waveguide array samples, as well as the reasons why AlGaAs was chosen as a material for sample fabrication, are discussed in Chapter 3.

Chapter 4 provides a description of the experimental setup and of the high power pulsed laser system that was chosen as a light source to satisfy the power requirements set by AlGaAs samples.

Chapter 5 is dedicated to the first experimental observation of discrete surface solitons [51]. It is shown that the results agree very well with the theoretical predictions [52]. The stability of these nonlinear surface waves and their unique power threshold behavior at and near the interface are discussed in detail. The experimental results on power threshold measurements and its dependence on soliton trapping site are presented. The work was extended to the samples with different waveguide widths which allowed the dependence on coupling strength between neighboring channels to be explored.

Chapters 6 and Chapter 7 deal with the interface between two dissimilar semi-infinite waveguide lattices. In such a configuration the dispersion curves of the two neighboring arrays are shifted with respect to each other due to the detuning of the propagation constants of the waveguides constituting the arrays. Here the Brillouin zone was kept identical for the two arrays by making their center-to-center channel spacing equal. The arrays were made different by choosing the different width of their channels. This led to an asymmetry in the intra-array and inter-array coupling parameters resulting in different power transfer across the boundary and different diffraction patterns in each array. In addition, the dynamical behavior of the coupled system depends on the separation of the two lattices. As a result, there exist new linear and nonlinear wave phenomena which are not possible in regular arrays and at array/continuum interfaces.

In Chapter 6, the study of linear propagation and the possibility of linear modes of different symmetry at the hetero-interface are discussed. Sample properties needed for various linear modes were investigated and regions of modes' existence identified numerically. Modes with π-out-of-phase fields in neighboring channels were predicted and observed experimentally in our samples [53].

In the nonlinear regime reported in Chapter 7, such a hetero-junction between two arrays can support a new family of surface waves, namely the hybrid surface solitons predicted recently by Makris et. al. [54]. For AlGaAs samples with self-focusing Kerr nonlinearity, two different solitons are predicted with fields in-phase in neighboring channels on both sides of the boundary. Both were observed in our samples. Their unique properties and results of the experiments on their observation are presented. Also, a number of unexpected interface soliton states were discovered experimentally.

The main results of this work, as well as possible directions of future work, are summarized in Chapter 8.

CHAPTER TWO: THEORY OF ONE-DIMENSIONAL DISCRETE OPTICS

The basic theory that leads to the equations describing electromagnetic wave propagation for arrays infinitely extended in one dimension is developed in this chapter. The approximate coupled mode approach which is based on solving Maxwell's equations for isolated channel waveguides is discussed. The overlap of pairs of the individual channel evanescent fields in the weak coupling limit is then calculated. Each pair corresponds to the well-known directional coupler of integrated optics in which energy is transferred periodically with propagation distance between channels. For the infinite 1D array this leads to coupled mode equations for each channel field with a weak nearest neighbor coupling to adjacent waveguides. This approach yields approximate solutions for the dispersion relations in the first band of the periodic systems and allows simple evaluation of discrete diffraction, the way in which light spreads throughout the array.

In parallel, the exact Floquet-Bloch modes of this periodic array are developed. In contrast to the coupled mode approach, in which only the integral over the first Fourier components of the index distribution is used to obtain the coupling constants, the Floquet-Bloch approach uses the exact index distribution of the array to produce numerical dispersion relations and the corresponding fields. This turns out to be important for evaluating the threshold powers for surface solitons at the continuum-discrete boundary in Chapter 5 and crucial for finding linear modes and solitons at the interface between two dissimilar arrays.

2.1. Wave propagation in a medium

The propagation of an electromagnetic wave in a medium with no sources of the electromagnetic field is described by the following set of Maxwell's equations

$$
\begin{aligned}
\vec{\nabla} \times \vec{E} &= -\frac{\partial \vec{B}}{\partial t} \\
\vec{\nabla} \times \vec{H} &= \frac{\partial \vec{D}}{\partial t} \\
\vec{\nabla} \cdot \vec{D} &= 0 \\
\vec{\nabla} \cdot \vec{B} &= 0,
\end{aligned}
\tag{2.1}
$$

where $\vec{E}$ and $\vec{H}$ are the electric and magnetic field vectors, $\vec{D}$ and $\vec{B}$ are the electric and magnetic flux densities, respectively. For a nonmagnetic dielectric medium the flux densities are related to the electric and magnetic field vectors through the following constitutive relations

$$
\begin{aligned}
\vec{D} &= \varepsilon_0 \vec{E} + \vec{P} \\
\vec{B} &= \mu_0 \vec{H},
\end{aligned}
\tag{2.2}
$$

where ε_0 is the vacuum permittivity, μ_0 is the vacuum permeability, and $\vec{P}$ is the electric polarization induced in the medium by the electromagnetic field.

By combining Equations 2.1 and 2.2 one can obtain the *wave equation* which describes the evolution of the electric and magnetic fields of an optical wave. For the electric field the wave equation is given by

$$
\nabla^2 \vec{E} - \frac{1}{c^2} \frac{\partial^2 \vec{E}}{\partial t^2} = \mu_0 \frac{\partial^2 \vec{P}}{\partial t^2},
\tag{2.3}
$$

where $c = \dfrac{1}{\sqrt{\mu_0 \varepsilon_0}}$ is the speed of light in vacuum and $\nabla^2 = \dfrac{\partial^2}{\partial x^2} + \dfrac{\partial^2}{\partial y^2} + \dfrac{\partial^2}{\partial z^2}$.

The induced electric polarization $\vec{P}$ is the result of the interaction of light with the material it passes through, the average of the induced dipole moments of individual atoms and molecules. In general the total electric polarization induced can be written as

$$\vec{P} = \varepsilon_0 \left(\vec{\chi}^{(1)} \cdot \vec{E} + \vec{\chi}^{(2)} : \vec{E}\vec{E} + \vec{\chi}^{(3)} \vdots \vec{E}\vec{E}\vec{E} + higher\ order\ terms \right), \tag{2.4}$$

in which $\vec{\chi}^{(1)}$, $\vec{\chi}^{(2)}$ and $\vec{\chi}^{(3)}$ are the linear, second and third order susceptibilities, and, in general, they are tensors of rank 2, 3, and 4, respectively. The corresponding terms in the Equation 2.4 are the linear, second order and third order contributions to the total electric polarization.

The work presented in this dissertation focuses on third order nonlinear effects in samples made of AlGaAs material. AlGaAs exhibits non-zero second order susceptibilities but they make no contribution to the present work due to lack of phase-matching for the geometries used. The third order susceptibility dominates nonlinear effects for the AlGaAs samples. Even higher order effects in the form of three photon absorption (due to $\Im mag\{\chi^{(5)}\}$) become important at the highest powers used in this work.

It is convenient to separate $\vec{P}$ into linear and nonlinear parts

$$\vec{P} = \vec{P}^L + \vec{P}^{NL}, \tag{2.5}$$

where $\vec{P}^L = \varepsilon_0 \vec{\chi}^{(1)} \cdot \vec{E}$ and can be easily incorporated into the left side of the Equation 2.3 such that the wave equation with optical polarization along the "i-axis" becomes

$$\nabla^2 \vec{E} - \frac{n^2}{c^2}\frac{\partial^2 \vec{E}}{\partial t^2} = \mu_0 \frac{\partial^2 \vec{P}^{NL}}{\partial t^2}, \tag{2.6}$$

where $n^2 = 1 + \Re eal\left(\chi_{ii}^{(1)}\right)$ and n is the linear refractive index of a medium.

Consider the simple case of a time-harmonic optical wave propagating in the z direction and linearly polarized along the x direction. The electric field of this wave is given by

$$\vec{E}(x,y,z,t) = \frac{1}{2}\hat{x}E(x,y,z)e^{i(kz-\omega t)} + c.c. \tag{2.7}$$

Here $E(x,y,z)$ is the spatial envelope of the electric field, k is the propagation constant in the z direction, and ω is the carrier frequency of the electromagnetic wave. Assume also that the nonlinear term in Equation 2.6 can be neglected (linear propagation). Substitution of the Equation 2.7 into the wave Equation 2.6 gives

$$2ik\frac{\partial E}{\partial z} + \frac{\partial^2 E}{\partial x^2} + \frac{\partial^2 E}{\partial y^2} + \frac{\partial^2 E}{\partial z^2} + \left(k_0^2 n^2 - k^2\right)E = 0, \tag{2.8}$$

where $k_0 = \omega/c$. Often, the so-called slowly varying envelope approximation (SVEA) [55] is used for which

$$\left|\frac{\partial^2 E}{\partial z^2}\right| << k\left|\frac{\partial E}{\partial z}\right|. \tag{2.9}$$

SVEA is based on the assumption that the electric field envelope changes slowly on a wavelength scale with propagation distance z. As a result, under SVEA Equation 2.8 becomes the well known *paraxial equation of diffraction*

$$i\frac{\partial E}{\partial z} + \frac{1}{2k}\nabla_\perp^2 E + \frac{1}{2k}\left(k_0^2 n^2 - k^2\right)E = 0. \tag{2.10}$$

12

Consider now the nonlinear propagation. For the reasons discussed earlier, for AlGaAs material we keep only the $\chi^{(3)}$ contribution to the nonlinear polarization given by

$$\vec{P}^{NL} = \varepsilon_0 \overset{=}{\vec{\chi}}{}^{(3)} : \vec{E}\vec{E}\vec{E}. \tag{2.11}$$

Because the electric field was assumed to be time harmonic with a single frequency ω, the right side of Equation 2.11 yields only components at frequencies ω and 3ω. The polarization component at frequency ω in case of the single-direction polarized wave gives rise to the nonlinear phenomenon called the Kerr effect (or intensity dependent refractive index) while that at frequency 3ω is responsible for third-harmonic generation. Because nonlinear soliton phenomena in $\chi^{(3)}$ nonlinear materials occur through the Kerr effect, henceforth only contributions from the "Kerr" component of the nonlinear polarization will be considered. Therefore, by analogy with the electric field for the linear case discussed earlier and ignoring cross-polarization effects, the nonlinear polarization can be written as

$$\vec{P}^{NL}(x,y,z,t) = \frac{1}{2}\hat{x}P^{NL}(x,y,z)e^{i(kz-\omega t)} + c.c. \tag{2.12}$$

Substituting expressions for $\vec{P}^{NL}$ and $\vec{E}$ from Equations 2.6 and 2.12 into the Equation 2.11 will give the following expression for P^{NL}

$$P^{NL} = \frac{3\varepsilon_0\chi_{xxxx}^{(3)}}{4}|E|^2 E, \tag{2.13}$$

and the nonlinear analog of the paraxial equation of diffraction (Equation 2.10) becomes

$$i\frac{\partial E}{\partial z} + \frac{1}{2k}\nabla_\perp^2 E + \frac{1}{2k}\left(k_0^2 n^2 - k^2\right)E + \frac{3k_0^2\chi_{xxxx}^{(3)}}{8k}|E|^2 E = 0. \tag{2.14}$$

Usually, the nonlinearly induced change of the refractive index is quantified by introducing the parameter n_2 (called optical Kerr nonlinear coefficient) such that

$$\hat{n} = n + n_2 |E|^2. \tag{2.15}$$

Using this relation and assuming that $n \gg n_2$, Equation 2.14 can be written in exactly the same form as the linear paraxial equation of diffraction (Equation 2.10) with n replaced by $\hat{n}$. In this case, the parameter n_2 is easily found to be

$$n_2 = \frac{3\chi_{xxxx}^{(3)}}{8n}, \tag{2.16}$$

and Equation 2.14 can be rewritten as

$$i\frac{\partial E}{\partial z} + \frac{1}{2k}\nabla_\perp^2 E + \frac{1}{2k}\left(k_0^2 n^2 - k^2\right)E + n n_2 \frac{k_0^2}{k}|E|^2 E = 0. \tag{2.17}$$

In the experiments, the readily measurable quantities are power and intensity of the optical beam. Therefore, it is customary to use another definition for Kerr nonlinear coefficient [55]

$$\hat{n} = n + \hat{n}_2 I, \tag{2.18}$$

where I (units W/m^2) is the intensity of the optical beam and is related to the electric field as

$$I = \frac{n\varepsilon_0 c}{2}|E|^2. \tag{2.19}$$

Straightforward analysis of Equations 2.15, 2.18 and 2.19 gives the relation between $\hat{n}_2$ and n_2, and, with the use of Equation 2.16, the nonlinear coefficient $\hat{n}_2$ is found to be

$$\hat{n}_2 = \frac{3\chi_{xxxx}^{(3)}}{4n^2 \varepsilon_0 c}. \tag{2.20}$$

2.2. Channel dielectric waveguide

The dielectric waveguide is the basic structural element of a waveguide array. In the discrete systems considered in this dissertation, it has a ridge cross-sectional geometry shown schematically in Figure 2.1.
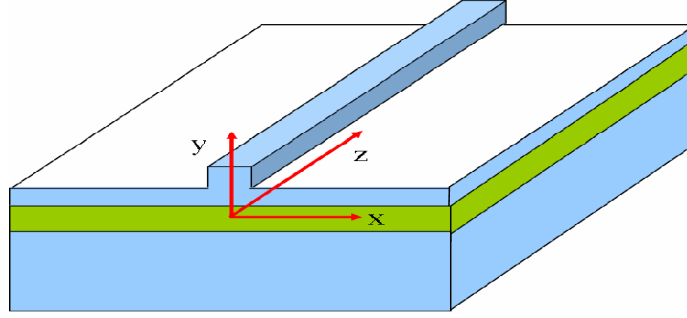
Figure 2.1: Channel ridge waveguide.

In such a waveguide, the optical field stays confined in both transverse x and y directions as it propagates along the z axis. In addition, the refractive index $n = n(x, y)$ of the waveguide is assumed to be independent of the z coordinate. It is convenient to write $n(x, y)$ as

$$n(x, y) = n_0 + \delta f(x, y). \tag{2.21}$$

Here $f(x, y)$ is the refractive index distribution function, normalized to unity, and δ is the maximum index contrast. Typically δ is of the order of $(1 - 2) \cdot 10^{-3}$, and is much smaller than the background index n_0. Therefore, the nonlinear evolution Equation 2.17 for this geometry becomes

$$i\frac{\partial E}{\partial z} + \frac{1}{2k}\nabla_\perp^2 E + k_0 \delta f(x, y)E + k_0 n_2 |E|^2 E = 0, \tag{2.22}$$

15

This equation is known as nonlinear Schrödinger equation (NLSE) for weakly guiding structures and, in general, can describe optical wave propagation for any refractive index distribution $f(x, y)$ as far as the weakly guiding limit holds. To find the beam propagation dynamics, 2D analog of the NLSE with only one transverse coordinate is usually used in numerical computer simulations.

2.3. Directional coupler

2.3.1. Coupled mode theory

Couple mode theory is an approximate and simple model for describing optical wave propagation when two or more waveguides are placed in proximity to each other. In general in an optical waveguide, there exist a number of propagating modes. These propagation modes are specific to each waveguide and satisfy the orthogonality condition. When two waveguides are brought together as shown in Figure 2.2, the optical modes of each waveguide interfere with each other [56].
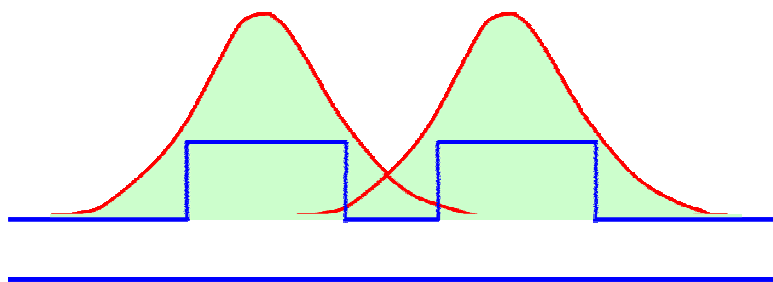
Figure 2.2: Schematic 1D refractive index distribution of two coupled waveguides with the field profiles of their fundamental modes.

The waveguide channels of the array structures discussed in this work were specially designed to be single-mode (i.e. to have only one propagating mode in each polarization at the experimental wavelength of light). The electric and magnetic field distribution of these unperturbed eigenmodes satisfy Maxwell's equations 2.1. In the case of time-harmonic fields, the latter can be written as

$$\vec{\nabla} \times \vec{E}_p = -i\omega\mu_0 \vec{H}_p$$
$$\vec{\nabla} \times \vec{H}_p = i\omega\varepsilon_0 n_p^2 \vec{E}_p ,$$

(2.23)

where $\vec{E}_p$ and $\vec{H}_p$ ($p = 1, 2$) are the eigenmodes' unperturbed fields and $n_p^2(x, y)$ is the refractive index distribution in each waveguide. Also, the guided mode fields can be written as

$$\vec{E}_p = \vec{e}_p(x, y)e^{i\beta_p z}$$
$$\vec{H}_p = \vec{h}_p(x, y)e^{i\beta_p z} ,$$

(2.24)

where $\vec{e}_p$ and $\vec{h}_p$ are the transverse modal profiles and β_p is the propagation constant of the mode. Assume that the total electromagnetic field of two coupled waveguides can be written as a superposition of these unperturbed eigenmode fields such that

$$\vec{E} = a(z)\vec{E}_1 + b(z)\vec{E}_2$$
$$\vec{H} = a(z)\vec{H}_1 + b(z)\vec{H}_2 ,$$

(2.25)

where $a(z)$ and $b(z)$ are called complex amplitudes. These total fields of the coupled structure also have to satisfy Maxwell's equations, i.e.

$$\vec{\nabla} \times \vec{E} = -i\omega\mu_0 \vec{H}$$
$$\vec{\nabla} \times \vec{H} = i\omega\varepsilon_0 n^2 \vec{E}.$$

(2.26)

Here $n^2(x, y)$ is the refractive index distribution of the entire structure.

By using Equations 2.23 – 2.26, the solution for the complex amplitudes $a(z)$ and $b(z)$ can be found. Its detailed derivation is provided in Reference [56], and for the geometry shown in Figure 2.2 the solution is given by the following coupled mode equations

$$
i\frac{da}{dz} + C_{11}a + C_{12}b\exp(i\Delta\beta z) = 0
$$
$$
i\frac{db}{dz} + C_{22}b + C_{21}a\exp(-i\Delta\beta z) = 0.
$$

(2.27)

Here $\Delta\beta = \beta_2 - \beta_1$ and

$$
C_{pq} = \frac{\omega\varepsilon_0 \int\limits_{-\infty}^{\infty}\int\limits_{-\infty}^{\infty}\left(n^2 - n_q^2\right)\vec{e}_p^{\,*}\cdot\vec{e}_q\,dxdy}{\int\limits_{-\infty}^{\infty}\int\limits_{-\infty}^{\infty}\left(\vec{e}_p^{\,*}\cdot\vec{h}_p + \vec{e}_p\cdot\vec{h}_p^{\,*}\right)_{\hat{z}}\,dxdy},
$$

(2.28)

where the pairs (p,q) are either $(1, 2)$ or $(2, 1)$, and

$$
C_{pp} = \frac{\omega\varepsilon_0 \int\limits_{-\infty}^{\infty}\int\limits_{-\infty}^{\infty}\left(n^2 - n_p^2\right)\vec{e}_p^{\,*}\cdot\vec{e}_p\,dxdy}{\int\limits_{-\infty}^{\infty}\int\limits_{-\infty}^{\infty}\left(\vec{e}_p^{\,*}\cdot\vec{h}_p + \vec{e}_p\cdot\vec{h}_p^{\,*}\right)_{\hat{z}}\,dxdy}.
$$

(2.29)

The introduction of the nonlinear polarization into Maxwell's equations 2.23 and 2.26 makes derivation of nonlinear coupled mode equations much more involved. However, for the simpler case of weak guiding, weak coupling and x-polarized electric fields, it can be shown that the nonlinear coupled mode equations are the following

$$
i\frac{da}{dz} + C_{11}a + C_{12}b\exp(i\Delta\beta z) + k_0 n_2 |a|^2 a = 0
$$
$$
i\frac{db}{dz} + C_{22}b + C_{21}a\exp(-i\Delta\beta z) + k_0 n_2 |b|^2 b = 0.
$$

(2.30)

18

Based on Equations 2.28 and 2.29, it can be shown that in the weak coupling limit $C_{11} \ll C_{12}$ and $C_{22} \ll C_{21}$. Therefore, the second terms of Equations 2.30 are usually neglected.

2.3.2. Linear directional coupler

A directional couple is formed when two waveguides are brought together such that the evanescent tail of the modal field in one waveguide overlaps with the core region of the second waveguide as shown in Figure 2.3. As a result, energy can be transferred from one waveguide to the other [19, 21, 56, 57]. The efficiency of the transfer process depends on many parameters such as extent of the modal field, separation between the waveguides and the mismatch in the propagation constants of the two guides.
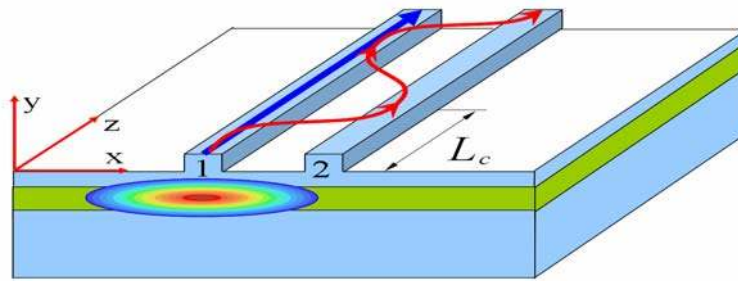
Figure 2.3: Schematic of a symmetric directional coupler in ridge waveguide geometry. At low power, there is a periodic exchange of energy between waveguides (red arrows). At high power, the waveguides are nonlinearly detuned, and no coupling occurs (blue arrow).

In the weak coupling limit, Equation 2.27 that describes the evolution of complex field amplitudes is reduced to

$$i\frac{da}{dz} + C_{12}b\exp(i\Delta\beta z) = 0$$

$$i\frac{db}{dz} + C_{21}a\exp(-i\Delta\beta z) = 0.$$

$$(2.31)$$

The analytical solution of this pair of coupled mode equations under the assumption $C_{12} \approx C_{21} = C$ (waveguides are similar but not exactly identical) is given by

$$a(z) = e^{-i\frac{\Delta\beta}{2}z}\left\{a(0)\cos(qz) + i\frac{C}{q}\left(b(0) + \frac{\Delta\beta}{2C}a(0)\right)\sin(qz)\right\}$$

$$b(z) = e^{i\frac{\Delta\beta}{2}z}\left\{b(0)\cos(qz) + i\frac{C}{q}\left(a(0) - \frac{\Delta\beta}{2C}b(0)\right)\sin(qz)\right\},$$

$$(2.32)$$

where $q = \sqrt{(\Delta\beta/2)^2 + C^2}$. Assuming that only one waveguide is initially excited, i.e. $a(0) = a_0$, $b(0) = 0$, the optical power in the channels as a function of distance z is given by

$$P_a(z) = |a(z)|^2 = a_0^2\left[1 - (C/q)^2\sin^2(qz)\right]$$

$$P_b(z) = |b(z)|^2 = 1 - P_a(z)$$

$$(2.33)$$

This solution shows that power is coupled periodically back and forth between channels as the beam propagates. However, as $\Delta\beta$ increases, these oscillations become more frequent, and a progressively smaller amount of energy is transferred from waveguide 1 to waveguide 2.

2.3.3. Symmetric nonlinear coupler

High power optical beams propagating in a nonlinear waveguide induce a nonlinear refractive index change through the Kerr effect, thus changing the propagation constant of the waveguide mode. Therefore, an optical beam launched into one channel of the nonlinear coupler changes the propagation constant mismatch $\Delta\beta$. As a result, beam propagation dynamics in

20

such a coupler at high powers is qualitatively similar to that of the mismatched linear coupler where essentially no power is transferred.

The evolution of complex field amplitudes in a symmetric nonlinear coupler (i.e. a coupler with identical waveguides) is described by the following coupled-mode equations (See Equations 2.30)

$$i\frac{da}{dz} + Cb + k_0 n_2 |a|^2 a = 0$$
$$i\frac{db}{dz} + Ca + k_0 n_2 |b|^2 b = 0. \tag{2.34}$$

This system of equations can be solved analytically in terms of Jacobi elliptic functions [58, 59]. Figure 2.4 shows the evolution of the power confined in the excited waveguide with propagation for three different powers of the incident beam. Here the propagation distance z has been normalized to the so-called coupling length $L_c = \pi/2C$ at which maximum power transfer is achieved in the linear regime. There is a critical power P_c at which total power is split equally between the waveguides after an infinite propagation distance [58]. This critical power is given by

$$P_c = \frac{8C}{k_0 \hat{n}_2} A_{eff}, \tag{2.35}$$

where A_{eff} is the nonlinear effective area of the waveguide mode which can be found as in [60]

$$A_{eff} = \frac{\left[\int\limits_{-\infty}^{\infty} \int\limits_{-\infty}^{\infty} |\vec{e}_1(x, y)|^2 dx dy \right]^2}{\int\limits_{-\infty}^{\infty} \int\limits_{-\infty}^{\infty} |\vec{e}_1(x, y)|^4 dx dy}. \tag{2.36}$$
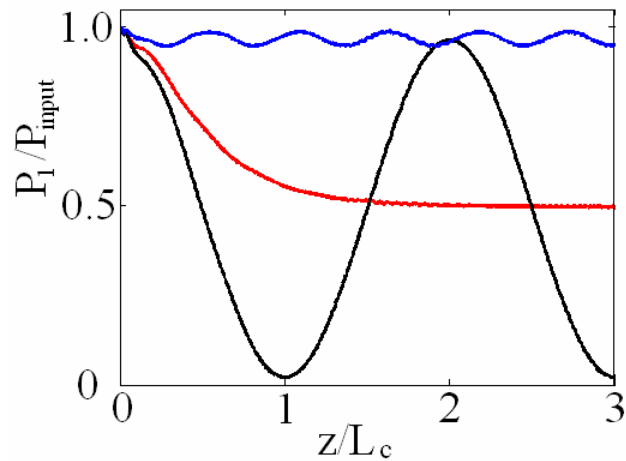
Figure 2.4: Power in the excitation waveguide as a function of the normalized propagation distance for quasi-linear propagation ($P = P_c/10$, black curve), the critical power ($P = P_c$, red curve), and high power ($P = 2P_c$, blue curve).

When the power is increased above the critical power, most of the energy stays in the excitation channel. Due to their unique nonlinear properties, nonlinear directional couplers have been the subject of a number of both theoretical [58, 59, 61–64] and experimental [65–68] studies for all-optical switching.

2.4. Array of coupled waveguides

When many identical parallel waveguides are placed equidistantly close to each other, they form a waveguide array as shown in Figure 2.5. The waveguides of the array are brought sufficiently close such that light is weakly coupled between channels as it propagates down the array.
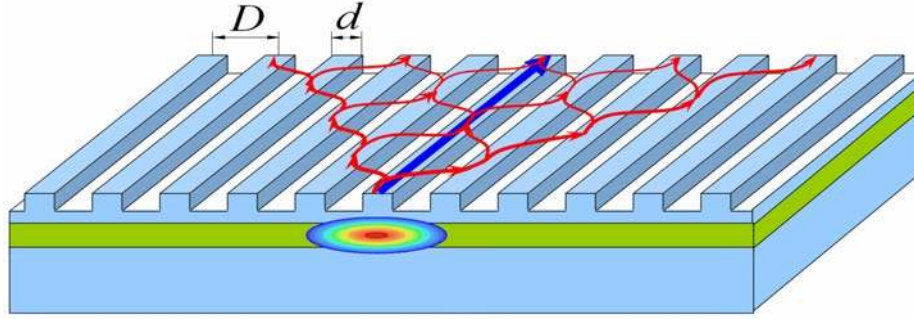
Figure 2.5: Schematic of a ridge waveguide array and the evolution of light wave propagating inside it. At low power, light diffracts in a discrete manner due to evanescent coupling (red arrows). At high power, strong localization in the excitation channel occurs (blue arrow).

There are two common approaches to describing optical wave propagation in such a structure. One of them is to use the nonlinear paraxial Equation 2.22. Usually, in order to simplify the analysis, the two-dimensional distribution function of the waveguides $n(x, y)$ is reduced to a one-dimensional refractive index profile using the *effective refractive index method* [56, 69]. The basic idea of this method is to calculate separately the effective refractive index of the vertical slab waveguide mode for the ridge region (n_{ridge}^{eff}) and that for the region in between ridges (n_{clad}^{eff}). The one-dimensional refractive index distribution $n(x)$ of the array is then given by interchanging regions with these two indices as shown in Figure 2.6.
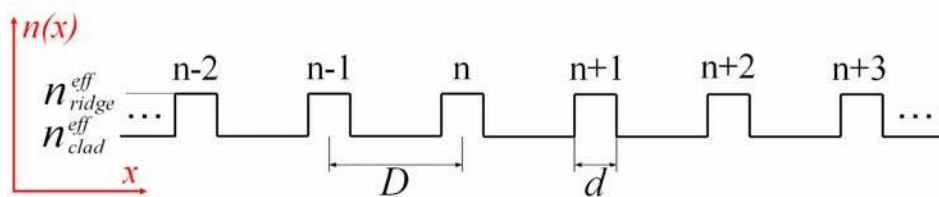
Figure 2.6: 1D refractive index potential of a waveguide array.

Now Equation 2.22 for the 1D refractive index potential, including nonlinearity, can be written as

$$i\frac{\partial E}{\partial z} + \frac{1}{2k}\frac{\partial^2 E}{\partial x^2} + k_0 \delta V(x)E + k_0 n_2 |E|^2 E = 0, \tag{2.37}$$

where $\delta = n_{ridge}^{eff} - n_{clad}^{eff}$, and the relation $n(x) = n_{clad}^{eff} + \delta V(x)$ was used.

Coupled mode theory discussed in Section 2.3 is another (approximate) approach to describe the propagation dynamics in waveguide arrays. Using this approach, the nonlinear evolution equations for the directional coupler 2.34 can be rewritten to include the coupling of each particular waveguide n (see Figure 2.6) with its neighboring $(n+1)$ and $(n-1)$ channels

$$i\frac{da_n}{dz} + C\left(a_{n+1} + a_{n-1}\right) + \gamma |a_n|^2 a_n = 0, \tag{2.38}$$

where a_n is the mode field amplitude in the nth channel and the definition $\gamma = k_0 n_2$ has been used for the Kerr nonlinear coefficient. Equation 2.38 is known as *discrete nonlinear Schrödinger equation* (DNLSE) [70].

2.4.1. Linear diffraction

In the linear regime, the following set of equations describes the evolution of the mode field amplitudes in a waveguide array

$$i\frac{da_n}{dz} + C\left(a_{n+1} + a_{n-1}\right) = 0. \tag{2.39}$$

In order to gain an understanding of the beam diffraction dynamics inside the array, consider two distinct cases: excitation of a single waveguide and infinite plane wave excitation.

Excitation of a single waveguide

When only one channel labeled $n = 0$ of the waveguide array is excited $(a_{n=0} = a_0,\ a_{n\neq0} = 0)$, the infinite set of ordinary differential Equations 2.39 can be solved analytically in terms of Bessel functions [21, 22]. The analytical solution is given by

$$a_n(z) = i^n a_0 J_n(2Cz), \tag{2.40}$$

where $J_n(x)$ is a Bessel function of the nth order. The evolution of the intensity of the optical beam described by Equation 2.40 is shown in Figure 2.7.
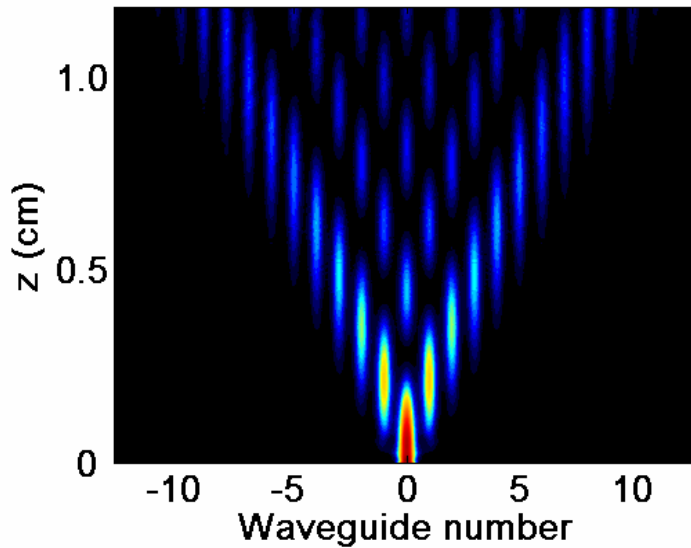
Figure 2.7: Discrete diffraction in a waveguide array for single channel excitation.

The striking difference between this diffraction pattern and diffraction in a continuous medium is clearly visible. While in a homogeneous medium the intensity maximum of the diffracting beam stays centered at the position of the input beam, for a discrete system most of the power is concentrated in the two intensity side lobes.

Diffraction of a plane wave

In the discrete case, the channels' modal field amplitudes for an infinite "plane wave" with constant amplitude in each channel can be defined as

$$a_n(z) = a_0 \exp(ink_x D)\exp(iqz), \tag{2.41}$$

where $k_x D$ (D is the inter-channel spacing) is the relative phase difference between adjacent waveguides and q is the contribution to the propagation constant β (of an isolated waveguide) due to discreteness. Substituting Equation 2.41 into Equation 2.39 yields the following dispersion relation [3, 23]

$$q = 2C\cos(k_x D). \tag{2.42}$$

Hence, the corresponding longitudinal wavevector k_z is related to its transverse component as

$$k_z = \beta + 2C\cos(k_x D). \tag{2.43}$$

Equation 2.43 is known as the *dispersion relation* for a 1D array [71, 72]. Its plot, reduced to the first Brillouin zone, is shown in Figure 2.8.
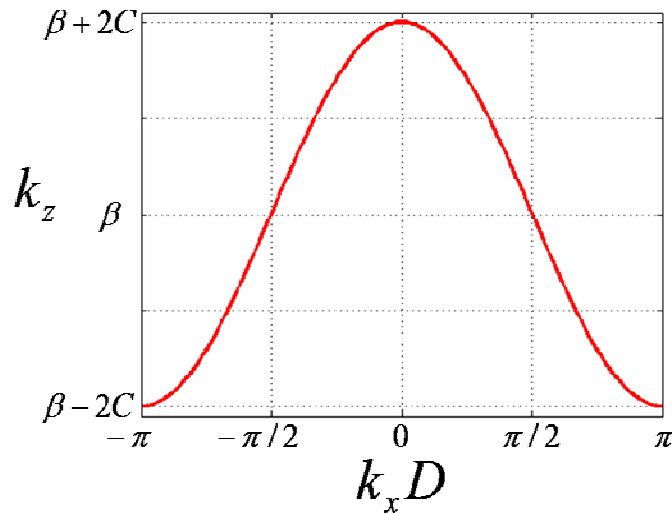
Figure 2.8: Dispersion relation of a 1D waveguide array.

Usually, in order to describe the diffraction of optical beams with a finite spatial extent, the dispersion relation given by Equation 2.43 is expanded around the central spatial frequency of the beam's wavepacket. By analogy with diffraction in the continuous media, it can be shown that for a particular transverse (Bloch) wavevector k_x, the transverse velocity v_x and diffraction coefficient D_x are given by [73]

$$v_x = \frac{\partial k_z}{\partial k_x} = -2CD\sin(k_x D)$$
$$D_x = \frac{\partial^2 k_z}{\partial k_x^2} = -2CD^2\cos(k_x D) \tag{2.44}$$

One of the most important consequences of discreteness is that the cosine dependence of the diffraction parameter D_x on the normalized transverse momentum $(k_x D)$ makes it possible to access both the normal $(D_x < 0)$ and anomalous $(D_x > 0)$ diffraction regimes. This is in clear contrast to the diffraction in continuous media where diffraction is always normal. Moreover, "diffractionless" propagation is possible when $k_x D = \pi/2$ [71].

2.4.2. Bloch waves and band diagram of a waveguide array.

The dispersion relation of a waveguide array can also be obtained from the linear analogue of wave Equation 2.37 using Floquet-Bloch analysis. Solving the wave equation by assuming Bloch wave solutions of the form

$$E(x,z) = E_{k_x}(x)\exp(ik_x x)\exp(ik_z z) \tag{2.45}$$

gives multiple values of k_z for each value of the transverse momentum k_x. This means that the propagation eigenvalues k_z form multiple *bands* of the periodic structure [41, 74, and 75]. The

band diagram of a typical waveguide array is shown in Figure 2.9(a). The validity of this approach has been confirmed experimentally by Mandelik et. al. in 2003 who demonstrated the excitation of the higher order bands in AlGaAs arrays [75, 76].
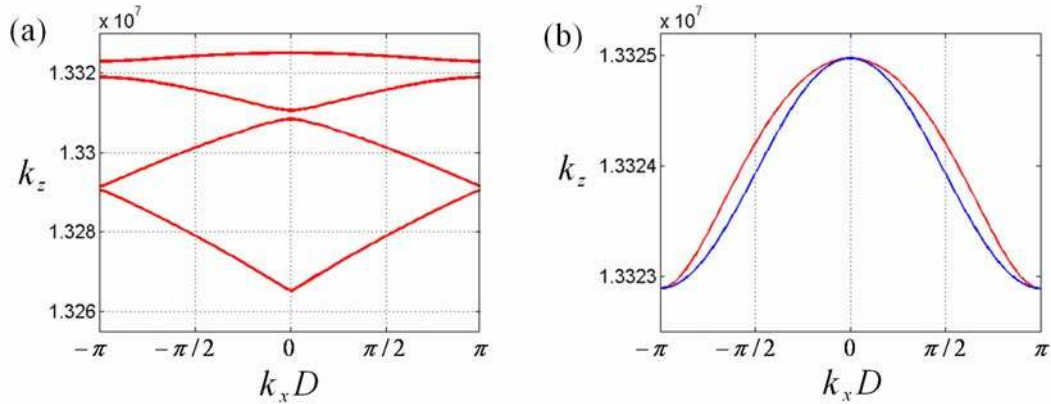
Figure 2.9: (a) Band diagram of a typical waveguide array with the four lowest order bands shown. (b) The first Floquet-Bloch band (red curve) and dispersion relation obtained based on discrete model (blue curve).

The coupled mode theory describes only approximately the propagation within the first band of the band diagram, the upper curve in Figure 2.9(a). The comparison of the first band of the band diagram with the discrete model dispersion relation is given in Figure 2.9(b). It is clear that the shape of the first Bloch band, although periodic, deviates from the cosine behavior found for the discrete model. This deviation is a result of the approximations used in coupled mode theory derivations.

2.4.3. Nonlinear propagation and solitons

To gain an understanding of nonlinear propagation dynamics and to see the difference relative to the linear propagation case, consider again single waveguide excitation. Figure 2.10 shows the simulated intensity of the cw optical wave for three different propagation regimes. At low input power as shown in Figure 2.10(a), the discrete diffraction pattern is obtained when most of the power finally escapes the excited channel. When the power is increased to the critical power P_c (Figure 2.10(b)), the propagation dynamics changes, and power escape rate from the excited channel decreases significantly. Finally, at even higher power level (Figure 2.10(c)), almost all energy stays confined in a single waveguide.
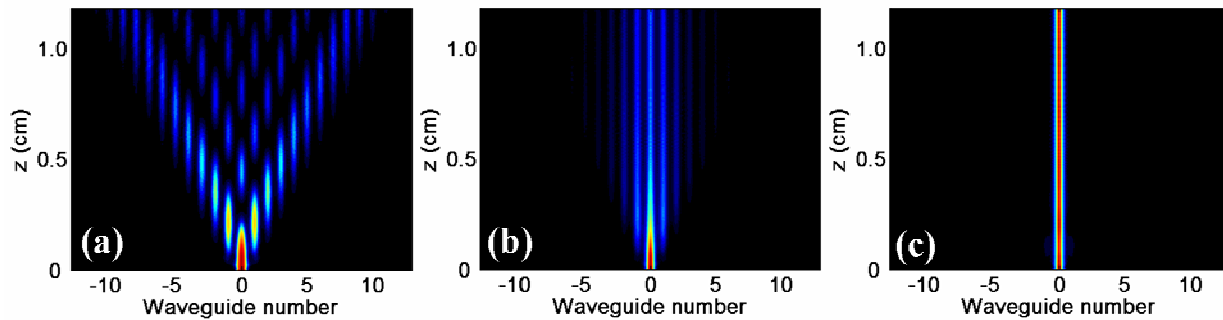
Figure 2.10: Simulated intensity as would be seen from the top of the waveguide array under single channel excitation at (a) $P_c/10$, (b) P_c and (c) $2P_c$ incident power levels.

To summarize the results presented in Figure 2.10, the evolution of the power confined in the excitation waveguide for the optical power levels of Figure 2.10 is shown in Figure 2.11.
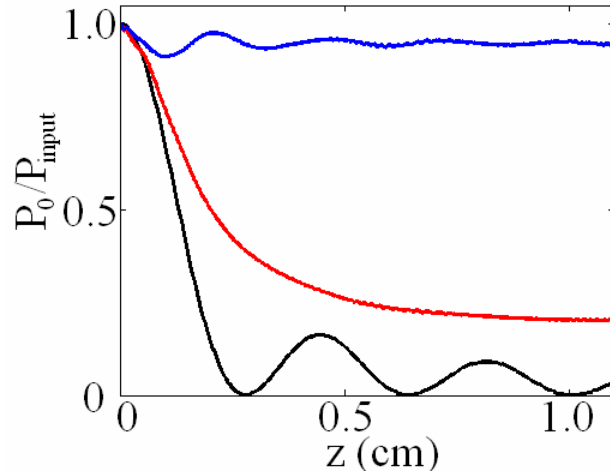
Figure 2.11: Power remaining in the excitation waveguide for single channel excitation as a function of the propagation distance for quasi-linear propagation ($P = P_c/10$, black curve), the critical power ($P = P_c$, red curve), and high power ($P = 2P_c$, blue curve).

Discrete solitons

The nonlinear localization behavior observed in Figure 2.10c suggests the possibility of non-diffracting stationary solutions to the DNLSE, known as spatial solitons.

As was discussed earlier, the nonlinear evolution of the envelope of the complex modal field amplitudes can be accurately described by the DNLSE of Equation 2.38. Because the solutions to DNLSE cannot be found analytically, a so-called continuum approximation is used to find the discrete field envelope of soliton waves [23]. First the substitution to DNLSE for modal field amplitudes of the form

$$a_n = u_n \exp(i\,2C\,z) \tag{2.46}$$

is implemented. After this substitution, the DNLSE becomes [23]

$$i\frac{du_n}{dz} + C\left(u_{n+1} + u_{n-1} - 2u_n\right) + \gamma|u_n|^2 u_n = 0. \tag{2.47}$$

30

Under the continuum approximation, we replace DNLSE by the continuous NLSE by applying the following Taylor series expansion:

$$u_{n\pm 1} = u \pm D\frac{\partial u}{\partial x} + \frac{D^2}{2}\frac{\partial^2 u}{\partial x^2},$$

(2.48)

where u_n was replaced by u. Applying this expansion to Equation 2.47, one can obtain the following continuous evolution equation for the field envelope

$$i\frac{du}{dz} + CD^2\frac{\partial^2 u}{\partial x^2} + \gamma|u|^2 u = 0.$$

(2.49)

Assuming the soliton solution to the Equation 2.49 of the form

$$u = \varphi\exp(i\mu z),$$

(2.50)

the approximate discrete field envelope φ_n and the nonlinear eigenvalue μ are found to be [23, 77, 78]

$$\varphi_n = A_0\,\text{sech}\frac{n}{w_0},$$

(2.51)

where $A_0 = \sqrt{\dfrac{2C}{\gamma w_0^2}}$ is the peak amplitude, $\mu = \dfrac{C}{w_0^2}$ is the nonlinear eigenvalue, w_0 is the width of the soliton expressed in units of the inter-channel spacing, and n is the channel number when the soliton is assumed to be centered on $n = 0$ channel. The full width at half-maximum (FWHM) of the discrete field envelope is given by

$$\Delta N = 2w_0\,\ln\!\left(2 + \sqrt{3}\right) \approx 2.63\,w_0.$$

(2.52)

The soliton propagation of the discrete envelope for $w_0 = 1.2$ is shown in Figure 2.12.
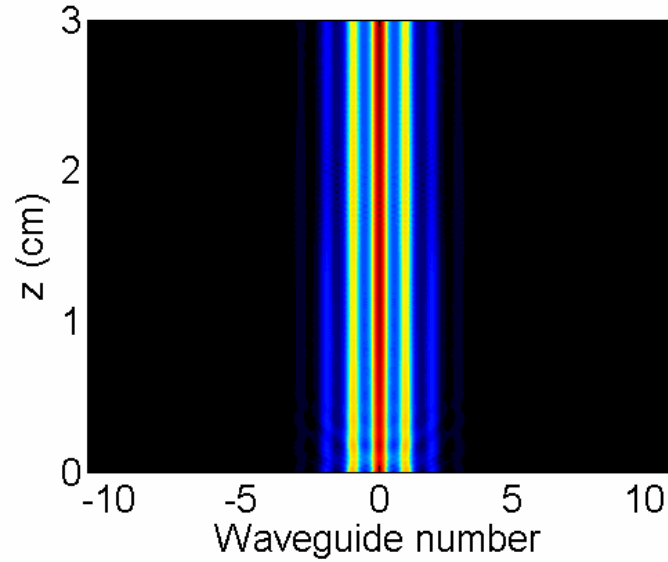
Figure 2.12: Simulation of the diffractionless propagation of a discrete soliton in a waveguide array.

This continuum approximation is valid only for sufficiently wide discrete soliton solutions, i.e. when the variation of the modal field amplitudes is relatively slow over a number of waveguides. For the single channel solitons and for those only a few channels wide, a numerical approach is used.

The discrete soliton shown in Figure 2.12 is of the bright, in-phase type, i.e. the fields in adjacent channels are all in-phase with each other. The nonlinear eigenvalue μ of such solution is located at the center of the Brillouin zone ($k_x D = 0$ in Figure 2.8). Another type of bright soliton is the so-called "staggered" soliton with a π phase shift between the modal field peak amplitudes in adjacent waveguides (i.e. $k_x D = \pi$ for this type). Both in-phase and staggered types are further split into odd, even, and twisted soliton sub-groups depending on the phase structure of their discrete field envelope [79]. The most common ones with relatively strong localization (existing in up to 5 channels) are shown in Figure 2.13 [80]. Many are unstable or

require a defocusing ($n_2 < 0$) nonlinearity. For example, the soliton shown in Figure 2.12 is of the odd type because the maximum of its envelope is centered on a waveguide site. In regular waveguide arrays with positive material nonlinearity ($n_2 > 0$) only the in-phase bright solitons are possible with all fields in phase. However, as will be discussed later, bringing the two dissimilar arrays together creates a hetero-junction where a new family of hybrid solitons with more complicated phase profiles of their field envelopes is found [54].
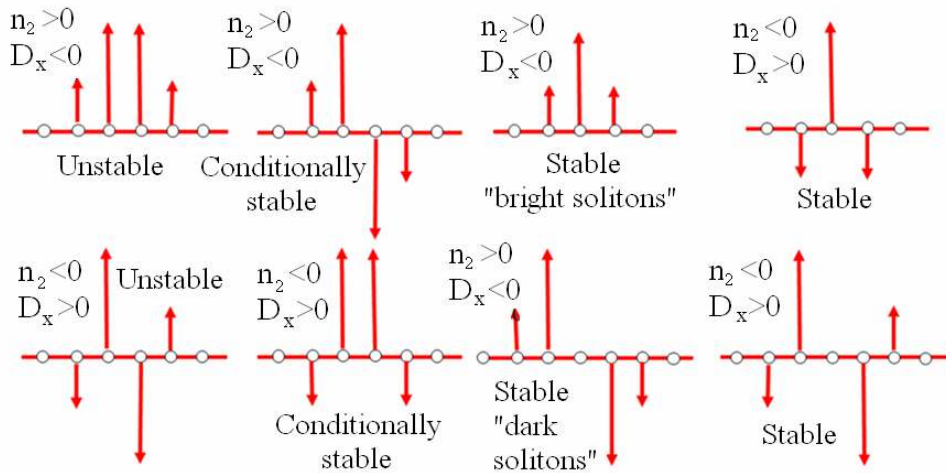
Figure 2.13: Strongly localized soliton solutions to the discrete nonlinear wave equation. The even solutions with maxima located between two equal magnitude neighboring channels which are either in phase or out of phase are both unstable. The twisted solutions are only stable for strong confinement. The remaining solutions are all stable.

CHAPTER THREE: SAMPLES

In this chapter we discuss many of the properties of the AlGaAs samples used in the observing discrete solitons in general. Of importance here are the material properties, the fabrication techniques used to make arrays, and the essential characterization of the samples including the coupling constants etc. The detailed modeling needed to study discrete surface solitons is left to Chapter 5, and the modeling of the hetero-structures to Chapters 6 and 7.

3.1. AlGaAs material properties

There were two main reasons for the choice of aluminum gallium arsenide (AlGaAs) as the material for sample fabrication. The first one is that the AlGaAs nonlinear properties make it an excellent material for nonlinear optics experiment. The Kerr nonlinear coefficient $\hat{n}_2$ of AlGaAs is about $1.5 \cdot 10^{-17} \, m^2 / W$ at a wavelength around $1.55 \mu m$, as measured in waveguides similar to those studied here [81]. For example, it is approximately three orders of magnitude higher than that of fused silica. The second reason for AlGaAs choice is the availability of the mature manufacturing technology for this semiconductor material which allows for fabrication of high quality waveguides. Different AlGaAs samples used in the experiments had linear losses in the range $0.6 - 1.1 \, dB / cm$ (linear absorption coefficient $\alpha = 0.14 - 0.25 \, cm^{-1}$). The nonlinear two-photon absorption (2PA) losses in the samples can

be reduced by using excitation at a wavelength $1.55 - 1.6 \mu m$ with photon energies below the half of the band gap energy of semiconductor material. While in this wavelength region 2PA still plays a role due to band tail states, the 2PA coefficient decreases rapidly with a wavelength increase and was considered to be negligible in our samples [81]. Therefore, below the half band gap, three-photon absorption (3PA) appeared to become the dominant nonlinear absorption mechanism and the limiting factor on the maximum power in the experiments. The 3PA coefficient of AlGaAs material at the wavelengths in the vicinity of $1.55 \mu m$ was

$$\alpha_3 \approx 0.05 \pm 0.02 \, cm^3 / GW^2 \text{ [82]}.$$

3.2. Design and fabrication

The basic sample fabrication procedure can be described as follows. First, molecular beam epitaxy (MBE) was used to deposit various $Al_x Ga_{1-x} As$ layers on a $GaAs$ wafer by Gregory Salamo's group at the University of Arkansas to grow a multilayer, single mode slab waveguide. The growth direction was along the [001] crystal axis. The channel waveguides were formed along the [011] axis by standard photolithography and reactive ion etching. The first set of samples (regular waveguide arrays) was fabricated by Marc Sorel's group at the University of Glasgow and the two-array hetero-junction samples were made by Richard Ares's research group at the University of Sherbrooke, Canada.

The AlGaAs waveguide array cross-sectional design is shown in Figure 3.1. In this design, a $1.5 \mu m$ thick core layer of $Al_{0.18} Ga_{0.82} As$ is sandwiched between the lower index $Al_{0.24} Ga_{0.76} As$ layers. The thickness $4 \mu m$ of the lower cladding layer was chosen to be sufficiently large to isolate the guiding layer from the $400 \mu m$ thick $GaAs$ substrate which had

the highest refractive index in the sample's composition. As was already discussed earlier, the guiding of light in the structure is achieved under the unetched ridges due to the local higher effective refractive index of the slab waveguide modes.
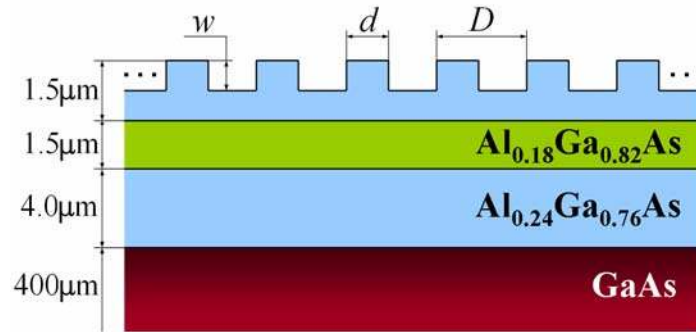
Figure 3.1: AlGaAs waveguide array design (schematic cross-section).

A microscope image of the actual sample with $d = 4 \mu m$, $D = 10 \mu m$ and $w = 0.72 \mu m$ is shown in Figure 3.2.
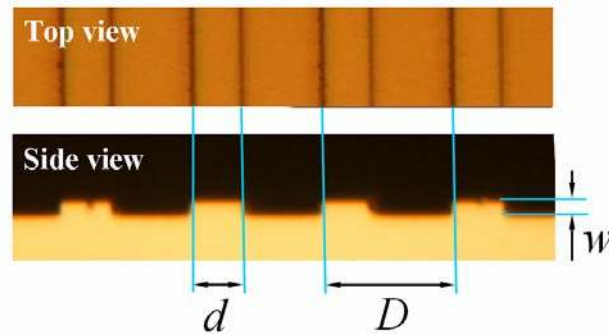
Figure 3.2: Optical microscope image of a real sample.

With these parameters, the intensity profile of the fundamental transverse-electric (TE) mode of an isolated waveguide has an elongated in *x*-direction shape as shown in Figure 3.3.
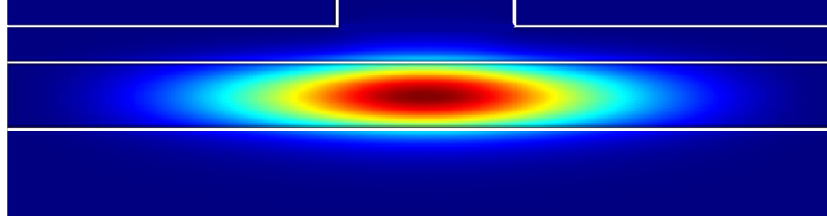
Figure 3.3: Calculated intensity of the fundamental mode of a ridge waveguide. The locations of the waveguide ridge and of the core layer are indicated by white lines.

In order to check the validity of the weakly guiding approximation (i.e. $\delta << n_{clad}^{eff}$) for the AlGaAs ridge array, its effective refractive index contrast δ for the 1D periodic index potential as a function of the etch depth w was calculated. The results shown in Figure 3.4 indicate that even with the cladding layer completely removed in between the guides (corresponds to $w = 1.5 \mu m$), the index contrast $\delta \approx 0.006$ is still much smaller than $n_{clad}^{eff} \approx 3.29$. The etch depths of the available samples were $0.72 \mu m$ and $1.1 \mu m$ which correspond to $\delta \approx 7.5 \cdot 10^{-4}$ and $2 \cdot 10^{-3}$, respectively.
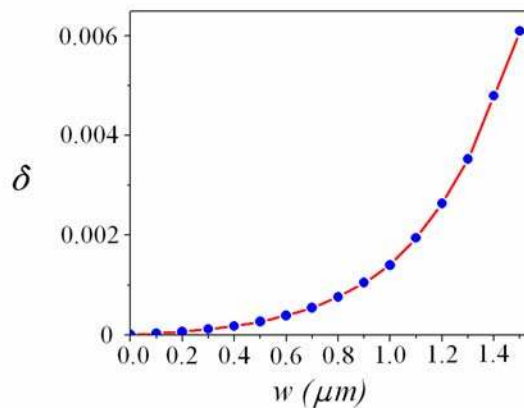
Figure 3.4: Calculated effective refractive index contrast as a function of the etch depth.

3.3. Sample characterization

Coupling constant

The coupling constant C of an array of coupled waveguides can be extracted by fitting the experimentally measured low power discrete diffraction pattern with the analytical solution given by Equation 2.40. An example of the best fit for the $1.35mm$ long sample with $d = 4.4\mu m$, $D = 10\mu m$ and $w = 1.1\mu m$ is shown in Figure 3.5. The measured diffraction pattern agrees well with the coupled mode theory calculations. As a result, using this method, the coupling constant can be found with an accuracy of about $2 - 3\%$.
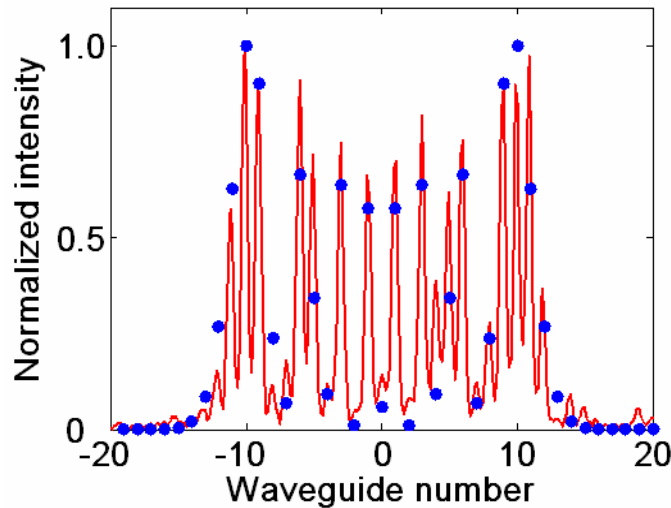
Figure 3.5: Measured discrete diffraction pattern (red curve) and the best fit with the analytical solution (dots) using value $C = 430m^{-1}$ for the coupling constant.

Dispersion relation

The dispersion relation of the first Bloch band of the array's band diagram can be experimentally obtained by exciting the array with a wide beam at low power. Then the relative phase shift

38

$\Delta \theta = k_x D$ between the adjacent channels is changed continuously within the range $(-\pi, \pi)$ by tilting the beam with respect to the array's entrance facet, and the output intensity is recorded. Because the propagation direction inside the array is given by the normal to the dispersion curve, the beam's output position will trace the shape of its first derivative dk_z / dk_x. The results of the corresponding experiment are shown in Figure 3.6. One can clearly see the deviation of the measured shape from the sinusoidal behavior of the first derivative for the discrete model. The experimental results are in much better agreement with the calculations based on the Bloch wave analysis as discussed in Chapter 2. In agreement with the Floquet-Bloch model, the zero diffraction point lies at larger than $\pi/2$ values of the relative phase $\Delta\theta$ which correspond to zero slope in Figure 3.6. Nevertheless, in most cases the coupled mode equations give a sufficiently accurate description of wave propagation dynamics in waveguide arrays.
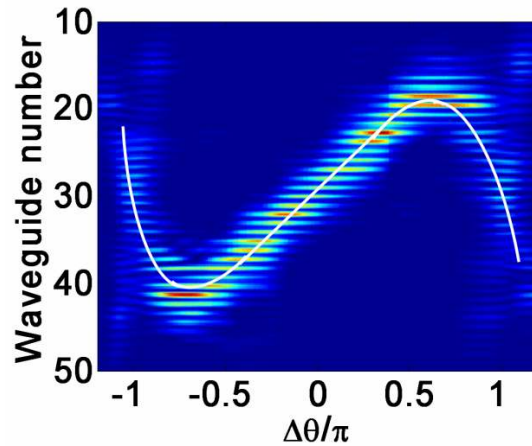
Figure 3.6: Measured derivative of the first Bloch band's dispersion relation. The white curve shows the approximate position of the output beam center.

Sample losses

Linear losses in the samples can be found using the Fabry-Pérot resonance technique [83, 84]. This approach utilizes the fact that an isolated single waveguide can be considered as a low finesse resonator with equal reflectivity at its end facets. From the standard analysis for a lossy resonator, the transmitted power of a Fabry-Pérot type waveguide is given by

$$P_t = P_{in} \frac{(R-1)^2}{(R-1)^2 \exp(\alpha L) + 2R\left[1 - \cos\left(\frac{4\pi L n_{eff}}{\lambda_0}\right)\right]}, \qquad (3.1)$$

where P_{in} is the incident optical power, $R = (n_{eff} - 1)^2 / (n_{eff} + 1)^2$ is the Fresnel power reflection coefficient at each of the waveguide's facets, α is the linear loss coefficient, and L is the waveguide length. As can be seen from the Equation 3.1, the dependence of the transmitted power on wavelength has an oscillating behavior. It is straightforward to show that the loss coefficient is given by

$$\alpha = -\frac{1}{L}\ln\left(\frac{1}{R}\frac{y-1}{y+1}\right), \qquad (3.2)$$

where $y = \sqrt{P_t^{max} / P_t^{min}}$ (P_t^{max} and P_t^{min} are the maximum and the minimum of the transmitted power, respectively). In the experiment, light from a low power cw source (HP81680A diode laser) was launched into an isolated waveguide, and the variation in the transmitted power was measured while the input wavelength was scanned within a narrow range around $1.55\mu m$. The recorded transmitted power for the sample with $w = 1.1\mu m$ is shown in Figure 3.7.
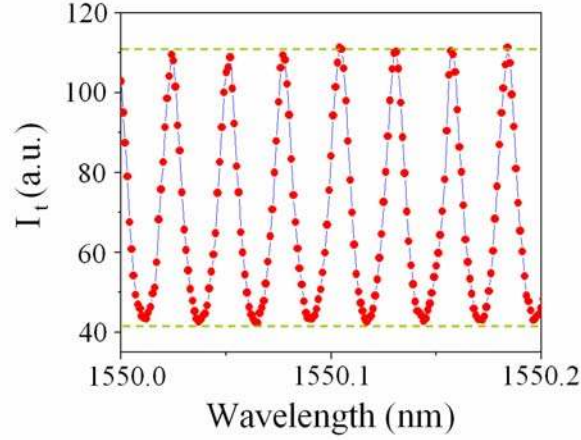
Figure 3.7: Throughput of an isolated waveguide as a function of the input beam wavelength.

Based on the throughput data and assuming the calculated value of the Fresnel power reflection at the waveguide's facets $R \approx 0.29$, the value $\alpha = (0.15 \pm 0.01)\,cm^{-1}$ (or $(0.65 \pm 0.04)\,dB/cm$) for the linear propagation losses was extracted.

Other parameters used in simulations of the nonlinear propagation in waveguide arrays are: effective mode area $A_{eff} \approx 14-19\,\mu m^2$ (depends on the width of the waveguide ridge) and the Kerr nonlinear coefficient $\gamma = k_0 \hat{n}_2 / A_{eff} \approx 3.3-4.5\,m^{-1}W^{-1}$ for $\hat{n}_2 = 1.5 \cdot 10^{-17}\,m^2 W^{-1}$. Assuming the two-photon absorption (2PA) to be negligible for the reason discussed earlier in this section, the three-photon absorption (3PA) coefficient $\alpha_3 \approx 0.04\,cm^3/GW^2$ was found by fitting the nonlinear transmission curve to be in good agreement with the data found in the literature [82].

CHAPTER FOUR: EXPERIMENTAL SYSTEM

The use of the AlGaAs system for experimental investigation requires the power levels at the sample input facet of the order of 1kW. Given that beam shaping etc. would necessitate a factor of 2 - 4 additional power this is clearly not available at 1550nm from any CW sources. Hence it is necessary to use a pulsed laser which considerably complicates the analysis of soliton effects since all of the predictions are for cw cases. Furthermore, such large cw powers would also lead to considerable heating, possibly leading to the sample damage. Thus, the usual 80-100MHz mode-locked lasers could also give problems due to the thermal load of high repetition rate pulses. Given all of these considerations, an OPG-OPA system operating at KHz repetition rates was a reasonable choice as the laser source. In this chapter, the laser system, as well as the other experimental apparatus required for experiments on solitons in arrays, is described.

4.1. <u>OPA tunable high power laser source</u>

A Spectra-Physics optical parametric amplifier (OPA) pumped by a laser/amplifier source was the system of the choice. The system layout and the typical operation parameters of its individual components are shown in Figure 4.1 and Table 1.
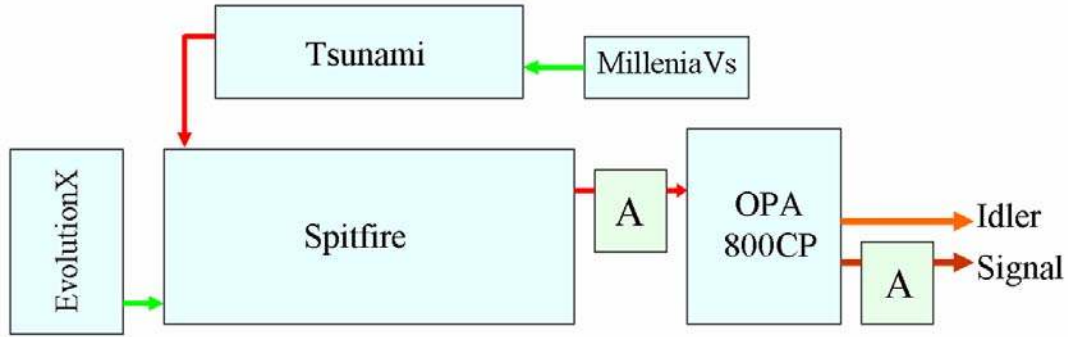
Figure 4.1: Optical source layout showing all of the major components. The typical operating parameters are given in Table 1.

Table 1: Typical operation parameters used in the experiments.

	Average power	Wavelength	Pulse duration	Repetition rate
MilleniaVs	4.4W	532nm	cw	-
Tsunami	800mW	783nm	150fs	79MHz
EvolutionX	6W	527nm	200ns	1kHz
Spitfire	700mW	783nm	1ps	1kHz
OPA 800CP: Signal beam Idler beam	40mW 30mW	1550nm 1582nm	1ps	1kHz

The system contains a Ti:Sapphire pulsed mode-locked femtosecond laser (Tsunami) pumped by an intracavity doubled neodymium yttrium vanadate (Nd:YVO) cw laser (MilleniaVs), a Q-switched neodymium yttrium lithium fluoride (Nd:YLF) intracavity doubled laser (EvolutionX), a Ti:Sapphire regenerative amplifier (Spitfire), and an optical parametric amplifier (OPA 800CP). Also, two custom-made autocorrelators were used to monitor the duration of pulses from both the Spitfire and the OPA 800CP. Despite the fact that the Tsunami output itself has peak powers of the order of tens of kilowatts, its achievable fundamental wavelength range (690

43

- 1080nm) does not cover the required experimental wavelengths of 1500 - 1600nm. Therefore, wavelength extension to the latter region is accomplished through the use of an OPA. A more detailed description of the laser system elements is given below.

Nd:YVO laser (MilleniaVs)

The MilleniaVs is a solid state, high power, visible cw laser that can provide more than 5W of the green light at a wavelength 532nm. The gain medium of this laser is a Nd:YVO rod pumped by two 13W laser diode bars. Fiber-coupling and delivering of the astigmatic beam from the diode bars transforms it to a round beam suitable for an efficient end-pumping geometry. This also allows the diode bars to be located in the power supply thus giving a very compact design and reducing the heat load on the laser head. The non-critically phase-matched lithium triborate (LBO) crystal placed within the laser cavity is used to convert the light at fundamental wavelength 1064nm to 532nm through a second harmonic generation (SHG) nonlinear process.

Ti:Sapphire laser (Tsunami)

The Tsunami is a solid-state mode-locked Ti:Sapphire laser. Its laser medium, a titanium-doped sapphire, is capable of tunable laser operation over a broad range of near infrared wavelengths from 690nm to 1080nm, and a range of pulse durations continuously variable from 80ps to less than 50fs. Our Tsunami is pumped by a MilleniaVs and produces 150fs long pulses at a 79MHz repetition rate. The operating wavelength was chosen to be 783nm. The regenerative mode-locking technique is used to convert the laser from cw to pulsed operation. Similar to the most common active mode-locking technique [85], it utilizes an acousto-optic modulator (AOM) as a mode-locking element which is placed inside the optical cavity and provides the required

periodic modulation of the cavity losses. However, unlike active mode-locking, the RF signal used to drive the AOM is obtained not from a separate RF generator but delivered from the laser cavity. A small part of the laser beam is deflected to a photodiode, and the detected signal is used to drive the AOM. This removes the requirement for the exact match of RF and the cavity round-trip frequency because the drive signal to the AOM changes accordingly with the cavity length.

The mode-locked pulse shortening in the Tsunami occurs through a combination of positive group velocity dispersion (GVD) and self-phase modulation in the Ti:Sapphire rod. Ideally, for the shortest pulse formation, the round-trip time in the cavity must be frequency independent within the pulse bandwidth. Therefore, in order to achieve near transform-limited pulses, positive GVD of the cavity elements is compensated by using prism pairs, a standard GVD compensation technique.

The Tsunami's output serves as the seed beam for the Spitfire.

Nd:YLF laser (EvolutionX)

The EvolutionX is a diode-pumped, Q-switched, intra-cavity frequency doubled Nd:YLF laser. Its gain medium (Nd:YLF rod) is pumped by four laser diodes which allows to achieve very efficient pumping because almost all spectrum of pump light falls within the absorption bandwidth of the gain medium. The laser resonator is Q-switched at the repetition rate of 1kHz using an acousto-optic modulator [86] which results in a train of ~200ns long pulses. Similar to the MilleniaVs, the fundamental wavelength 1053nm of the EvolutionX is efficiently frequency doubled to produce green light via a LBO crystal placed within the laser cavity.

The output of the EvolutionX is used as a pump for the Spitfire.

45

Regenerative amplifier (Spitfire)

The Spectra-Physics Spitfire is a regenerative amplifier designed to amplify single pulses from a mode-locked Ti:Sapphire laser. Input pulses of energy only a few nano-joules are typically amplified to milli-joule levels, which represents an overall amplification of the order of 10^6. Usually in amplifiers, the maximum output energy is limited by pulse distortion through the nonlinear interaction of light with the amplifier gain medium and by the damage threshold of optical elements. However, the use of chirped pulse amplification (CPA) technique makes it possible to avoid these detrimental effects. In CPA, the pulse to be amplified is temporally stretched in order to reduce its peak power, then amplified, and finally recompressed to close to its original duration. Therefore, the Spitfire consists of three main elements, namely a pulse stretcher, an amplifier, and a pulse compressor.

In the stretcher, the seed pulse from the Tsunami is stretched by as much as 10000 times using a bulk grating system. The Spitfire regenerative amplifier contains a Ti:Sapphire crystal as a gain medium pumped by the 200ns long pulses from EvolutionX. The amplification of a seed pulse takes place when the seed pulse passes through the gain medium. Since the one-pass amplification is only about a factor of 3 - 4, the Ti:Sapphire crystal is placed into a cavity with two mirrors, thus allowing the amplified pulse to pass multiple ($\sim 15-20$) times through the gain medium while the much longer pump pulse is present. In order to introduce the seed pulse into the resonator and to switch the amplified pulse out of the cavity, two Pockel's cells (electro-optic switches) are placed inside it. The first Pockel's cell is used to switch the seed pulse into the amplifier cavity, and the timing of the second one is adjusted to switch the amplified pulse

out of the resonator after a sufficient number of round trips. Finally in the Spitfire pulse compressor, the high energy amplified pulse is recompressed to the $\approx 1 ps$ duration.

Optical parametric amplifier (OPA 800CP)

As pointed out earlier in this section, the need for conversion of the Tsunami wavelength to the 1550nm wavelength region necessitates the use of an optical parametric amplifier. The OPA 800CP is a two stage, white light seeded optical parametric amplifier pumped by the output from the Spitfire regenerative amplifier. In the OPA 800CP, a small part of the pump is directed to pass through the Sapphire plate where a super-continuum (so-called white light) is generated through a variety of nonlinear processes including self-phase modulation, self-focusing, Raman shift and other higher order nonlinear phenomena. The white light is pre-amplified in a Beta-Barium Borate (BBO) crystal using about 10% of the pump power through the nonlinear second order parametric process. The amplified signal and idler beam wavelengths are determined by the phase-matching angle of the BBO crystal. The pre-amplified signal is then amplified with the remaining ~90% of power during the second pass through the nonlinear crystal. Finally, the signal and idler beams are separated using a polarizing beam splitter. The OPA 800CP allows continuous tuning of the signal wavelength within the range 1100 − 1570nm. The wavelength of the idler beam which is given by the relation $\lambda_{Idler} = 1/(1/\lambda_{Spitfire} - 1/\lambda_{Signal})$ spans from 1570nm to approximately 2800nm.

Output pulse parameters

The duration of the OPA output pulses was measured by a custom-made autocorrelator using the collinear interferometric second harmonic autocorrelation technique [87, 88]. The measured

autocorrelation and its envelope calculated based on the 1ps long pulse (FWHM) are shown in Figure 4.2(b). For the transform-limited Gaussian pulse, the duration of 1ps corresponds to a spectrum of 3.53nm FWHM. The measured OPA spectrum shown in Figure 4.2(a) has a slightly higher bandwidth of 4nm FWHM which indicates the presence of a small residual chirp.
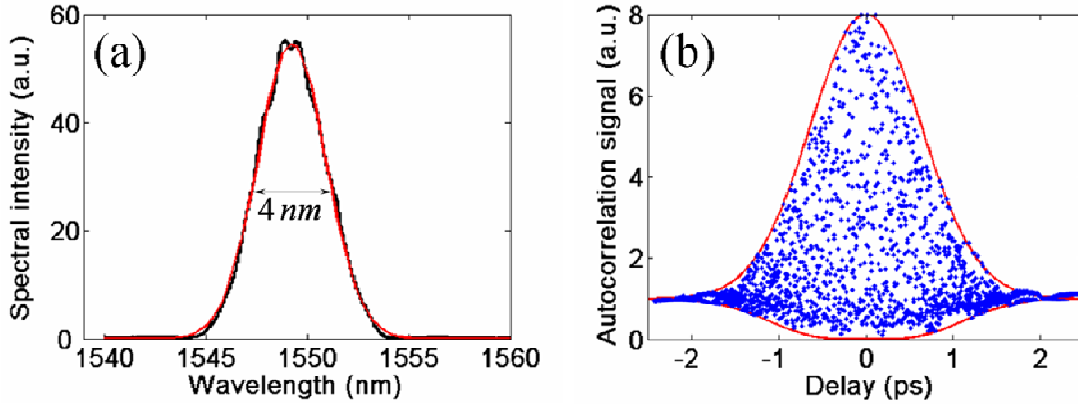
Figure 4.2: Output of OPA 800CP (a) Measured spectrum (black curve) and Gaussian fit (red curve). (b) Measured interferometric autocorrelation (blue dots) and calculated autocorrelation envelope for a 1ps long pulse (red curve).

4.2. Experimental setup

The experimental setup for the observation of discrete solitons in AlGaAs waveguide array samples is shown in Figure 4.3. The signal beam from the OPA 800CP described above is used as a light source for the experiments. First, directly after the exit aperture of the OPA, about 4% of the input power is split off the main beam with a beam sampler and is used for the OPA diagnostics (to monitor the spectrum and the pulse train stability (using a photodiode connected to an oscilloscope). Then the main part of the beam is spatially filtered to reduce spatial beam distortions. The spatial filter consists of a lens L1 with a focal length equal to 7.5cm, and a

100μm diameter ceramic pinhole. The beam is then collimated using the lens L2 with the same focal length as that of L1.
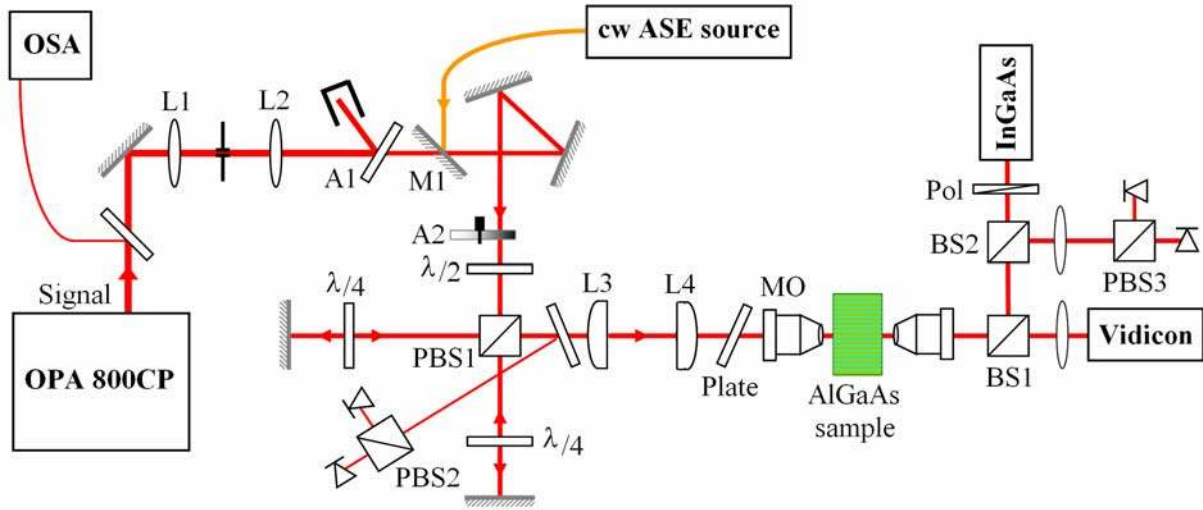
Figure 4.3: Experimental setup.

After the spatial filter, the peak power of the signal beam is ~20MW. For typical experiments the maximum required peak power right before the sample does not exceed 5kW. Therefore, taking into account losses in the optics downstream, the OPA beam power needs to be reduced by three orders of magnitude. This is done by using a reflective attenuator A1 which directs about 99% of the power to a low backscatter laser beam trap, and a variable attenuator A2.

After the attenuator A1, a flip mirror M1 is placed in the beam path. In the position when the beam from OPA is blocked, this mirror allows the introduction of the low peak power, cw radiation from an amplified spontaneous emission (ASE) source. This beam is collinear with the OPA beam and is used for coupling light into the waveguide array during initial aligning.

The polarization of the beam is then adjusted with a half-wave plate. The polarizing beam splitter PBS1 is introduced into the beam path to generate two orthogonally polarized beams when needed for certain experiments. After recombining the orthogonally polarized beams again

in PBS1, a small part of the beam is split off with a beam sampler for the power monitoring purposes. The two polarizations are separated by the beam splitter PBS2 and detected by germanium photodiodes. The photodiodes' signals are directed to lock-in amplifiers synchronized to the repetition rate of the OPA which provides a significant suppression of the uncorrelated noise.

The beam input into the sample is shaped using a pair of cylindrical lenses L3 and L4, and the in-coupling microscope objective MO with a 40x magnification. The available lens set includes 50, 100, 150, 200, 250, 300, 500 and 1000mm focal length cylindrical lenses. The orientation of the cylindrical lenses is chosen such that the beam spatial parameters are not changed in the vertical direction, i.e. normal to sample surface. The FWHM of the beam intensity in vertical direction is therefore defined by the strength of the in-coupling objective MO, and is adjusted to be ~2μm thus matching the vertical profile of the waveguide mode. The choice and the position of the cylindrical lenses L3 and L4 are defined by the experimental requirements to the horizontal beam cross-section which (with the available set of lenses) can be set within the range between 2μm and more than 300μm. Furthermore, a plane parallel glass plate is placed in front of the in-coupling objective. The horizontal rotation of this plate shifts the beam sideways which results in a change of the propagation direction of the input beam after the in-coupling objective and hence in a change of the input phase difference between adjacent channels. The glass plate is mounted on a rotation motorized stage. This is particularly useful for the experiments which require the continuous controlled tilting of the input beam with respect to the sample's entrance facet (i.e. the continuous variation of the relative phase between the adjacent channels).

The sample itself is mounted on a five axis translation stage. This gives the possibility to adjust not only the XYZ position of the sample but also to align the axis of the one-dimensional array with the horizontal axis of the asymmetric input beam. The output facet of the sample is imaged onto two cameras using a non-polarizing 50/50 beam splitter BS1 and an additional lens. The less sensitive Hamamatsu vidicon camera is usually used only for visual monitoring of the output intensity during alignment procedures. Another 50% of the power is directed to a highly sensitive InGaAs line array camera (Roper Scientific OMA V) with 512 pixels. This power is also used to monitor the output power in either polarization by introducing additional beam splitters BS2 and PBS3. A polarizer mounted right in front of the InGaAs camera in used to take images in different polarizations.

CHAPTER FIVE: DISCRETE SURFACE SOLITONS

After the experimental observation of discrete solitons inside the nonlinear waveguide lattices [27-31], the question arose whether discrete nonlinear surface waves (surface solitons) can exist at the edge of a semi-infinite waveguide array. And in 2005 the possibility of such nonlinear states had been demonstrated theoretically [52].

In this chapter the theory of surface solitons at the boundary between a 1D discrete and a 1D continuous medium is developed. The key properties of these solitons are first identified and then investigated experimentally.

5.1. Introduction

To analyze the problem of nonlinear surface waves, consider a semi-infinite Kerr-nonlinear lattice shown schematically in Figure 5.1.
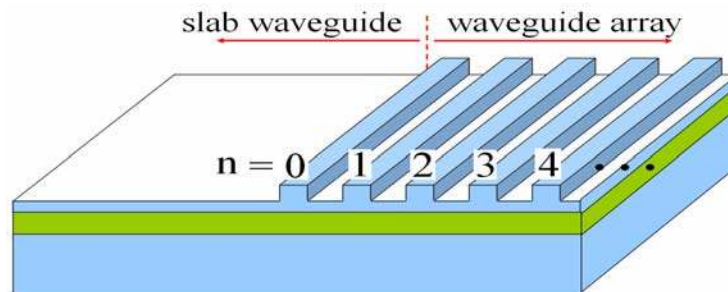
Figure 5.1: The schematic of a semi-infinite waveguide array.

The DNLSE that describes the evolution of complex modal field amplitudes for this system can be written as

$$i\frac{da_0}{dz} + Ca_1 + \gamma|a_0|^2 a_0 = 0, \quad (n = 0)$$
$$i\frac{da_n}{dz} + C(a_{n+1} + a_{n-1}) + \gamma|a_n|^2 a_n = 0, \quad (n \geq 1),$$

(5.1)

where the first equation describes the envelope of the peak field in the channel at the edge of the array ($n = 0$ waveguide site) and the second one is applied at every other site $n \geq 1$. Of course, these equations are valid only for the first band in the coupled mode approximation which is adequate for this purpose. The ridges formed in the upper cladding lead to an effective refractive index to the right of the boundary larger than that to the left. Hence, the fields associated with the channel waveguides exhibit a higher effective refractive index than that experienced by any propagating modes in the 1D slab waveguides, i.e. the propagation wavevectors for the array region are larger than those of the slab waveguide. As a result, at the boundary, there is no coupling between the slab waveguide modes and the array modes, and the boundary channel field decays exponentially with distance into the slab region with the decay constant approximately that for a single isolated channel. However, this boundary channel does couple via its evanescent field to its nearest neighbor channel.

Consider the linear behavior of this system first. Similar to the case of an infinite waveguide lattice, the spatial impulse response of this semi-infinite system (i.e. when only one, the mth channel of the array is excited) can be obtained in closed form in terms of Bessel functions using coupled mode theory [52]

$$a_n(z) = a_0\left[i^{n-m}J_{n-m}(2Cz) + i^{n+m}J_{n+m+2}(2Cz)\right].$$

(5.2)

The resulting propagation dynamics for the excitation of the first ($m = 0$), the second ($m = 1$) and the third ($m = 2$) waveguides of the array is shown in Figures 5.2(a) - (c), respectively. As one can see, these discrete diffraction patterns differ considerably from that in an infinite lattice. The difference arises from the boundary reflection which results in an additional (higher order Bessel function) term in the analytical solution given by Equation 5.2.
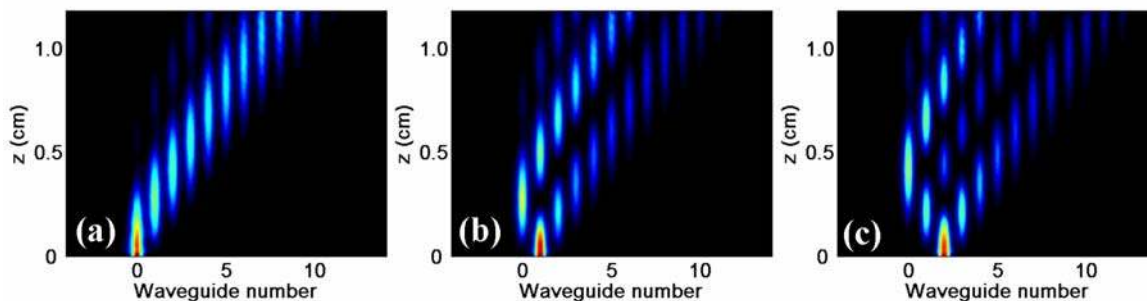
Figure 5.2: Simulated discrete diffraction when (a) the first, (b) the second, and (c) the third waveguides of a semi-infinite array are excited.

It is noteworthy that in the linear response regime, the system under consideration cannot support any linear surface waves since the background index of the slab waveguide underlying the array is the same as that of the outer slab waveguide region.

To gain an understanding of nonlinear propagation in a semi-infinite waveguide array, consider again the single waveguide excitation of the boundary $n = 0$ channel. Figure 5.3 shows the simulated intensity of an incident cw optical wave for three different propagation regimes. In the low input power regime shown in Figure 5.3(a), the discrete diffraction pattern associated with the analytical solution of Equation 5.2 is obtained. Most of the power escapes the excitation channel. When the power is increased to the critical power P_c as defined previously for a two-channel nonlinear directional coupler in Equation 2.35, the propagation dynamics (Figure 5.3(b))

changes with more than half of the total power confined in the boundary channel. Finally, at a power level twice the critical power (Figure 5.3(c)), almost all the energy stays localized in the excited waveguide. Such nonlinear localization behavior suggests the possibility of discrete surface solitons, the non-diffracting stationary solutions to the DNLSE of Equation 5.1.
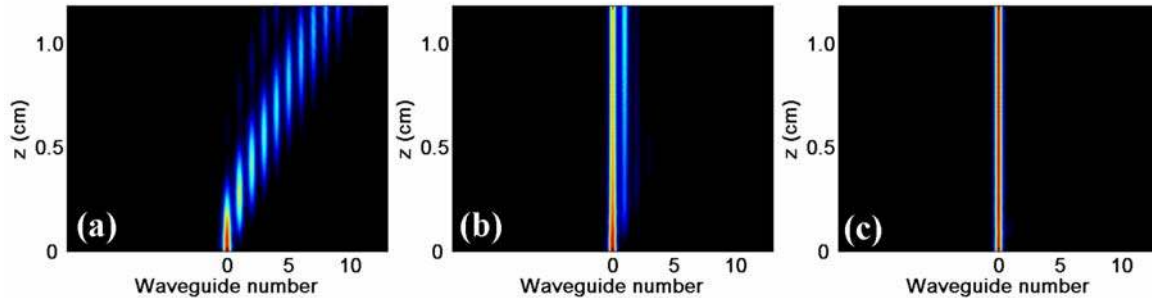
Figure 5.3: Simulated propagation in a semi-infinite array when the first ($n = 0$) channel was excited at (a) $P_c/10$, (b) P_c, and (c) $2P_c$ power levels.

To summarize the results presented in Figure 5.3, the evolution of the power confined in the excitation waveguide as a function of distance is shown in Figure 5.4. While these results are qualitatively similar to those of Figure 2.11 for an infinite lattice, two quantitative differences are easily identifiable. To be specific, for the low power case the power escape rate from the excited channel is much faster for a semi-infinite lattice. Also for the semi-infinite case at the critical power, about three times more power stays in the excited guide (~60% versus ~20% in an infinite lattice).
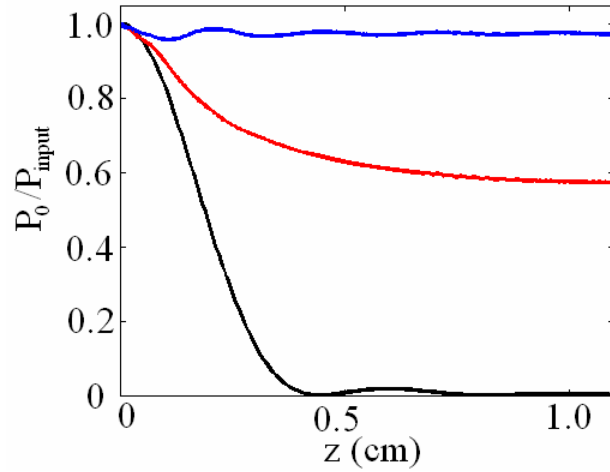
Figure 5.4: Power remaining in the excitation ($n = 0$) channel as a function of the propagation distance for quasi-linear propagation ($P = P_c/10$, black curve), the critical power ($P = P_c$, red curve), and high power ($P = 2P_c$, blue curve).

Discrete nonlinear surface waves in a semi-infinite lattice can be numerically found using relaxation methods by assuming a stationary solution to the Equation 5.1 of the following form

$$a_n = u_n \exp(i\mu Cz) \tag{5.3}$$

where $\mu \geq 2$ is the normalized nonlinear propagation eigenvalue. Because the nonlinearity for AlGaAs is of the self-focusing type ($n_2 > 0$), one searches for in-phase solutions, i.e. all the fields u_n are taken to be positive [52]. Figure 5.5 shows the total power $P = \sum_n |a_n|^2$ carried by the soliton solutions peaked at the boundary channel versus the eigenvalue μ. This plot indicates that the $P - \mu$ curve exhibits a minimum which, in turn, implies that discrete nonlinear surface waves can exist only above a certain power threshold. Below the power threshold no surface waves can be supported. The power threshold behavior of discrete surface solitons will be discussed in detail later in this chapter.

56
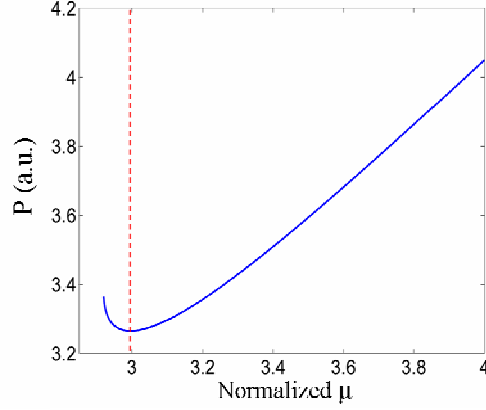
Figure 5.5: Normalized total power versus eigenvalue μ for an in-phase surface soliton solution peaked at the $n = 0$ waveguide site. The red dashed line defines the minimum μ for stable propagation.

Linear stability analysis reveals that the surface wave solutions are only stable to the right of the minimum of $P - \mu$ curve, i.e. in the region where $dP/d\mu > 0$, in agreement with the well-known Vakhitov-Kolokolov criterion for continuous media [89, 90]. In the stable branch, the localization of soliton solutions increases with soliton power and the evanescent field decays into the continuous low index region. All these properties of discrete nonlinear surface waves mirror closely those of surface solitons between continuous media [42-48].

5.2. First Observation of discrete surface solitons

For the experimental observation of highly confined discrete surface solitons, the setup described in Chapter 4 was configured to excite a single boundary channel of a 1cm long AlGaAs array containing 101 waveguides. Other parameters of the sample were the following: period $D = 10 \mu m$, channel width $d = 4 \mu m$, and etch depth $w = 0.72 \mu m$. The coupling constant

for the TE polarized light was found to be $C = 730m^{-1}$. Therefore, the length of the sample corresponds to approximately 4.5 discrete coupling lengths.

In the first set of experiments, the input beam was focused onto the boundary $n = 0$ channel of the AlGaAs waveguide array, and the intensity distributions at the sample's end facet were recorded. The variation of the normalized output intensity across the array as a function of the input beam peak power is shown in Figure 5.6.
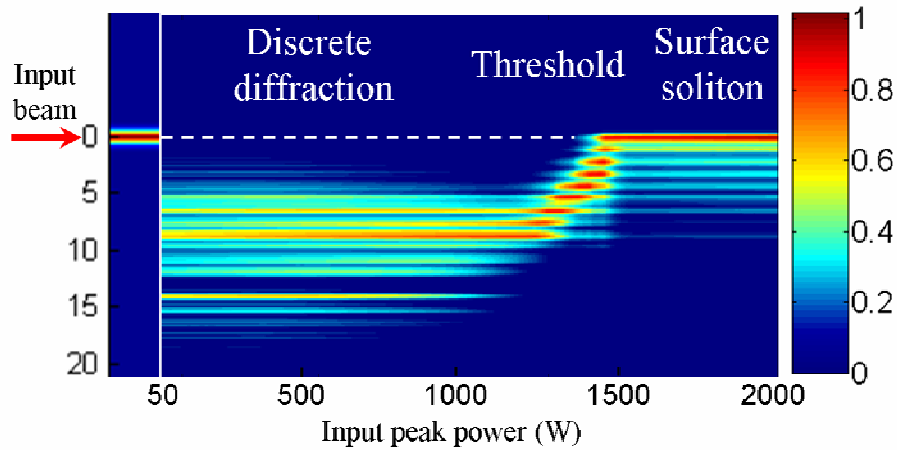
Figure 5.6: Intensity distributions recorded at the sample's output facet versus peak power of an input beam injected into the $n = 0$ channel. The output data was sampled for each power by the software, the maximum intensity channel identified, the color of that channel was set to red (maximum), and the remaining data at that power was renormalized.

There are three clear regions to the response. The discrete diffraction associated with the linear response of the array persists until the threshold power is reached. In the threshold region there is a rapid collapse of power towards the excitation channel. Finally, a discrete surface soliton is formed with most of its energy localized in the boundary channel. Some fraction of the incident power still remains in the discrete diffraction pattern due to the pulsed nature of the excitation.

Even though the experiments were carried out with pulses, a rapid collapse was found to occur above 1.2kW, a clear indication of the threshold behavior expected of surface solitons.

Given the fact that the experiments utilized ultra-short (1ps) pulses and that the waveguides are not only dispersive but also exhibit three-photon absorption, the beam dynamics in both space and time was simulated using the following NLSE [51]

$$i\frac{\partial E}{\partial z} + \frac{1}{2k}\frac{\partial^2 E}{\partial x^2} - \frac{k^{''}}{2}\frac{\partial^2 E}{\partial T^2} + k_0\delta V(x)E + k_0 n_2 |E|^2 E + i\hat{\alpha}_3 |E|^4 E = 0, \qquad (5.4)$$

where $k^{''} = 1.3 \cdot 10^{-24} m^{-1} s^2$ is the normal group velocity dispersion coefficient of AlGaAs at a wavelength of $1.55\mu m$, T is a time coordinate moving at the group velocity of the wave, $\delta \approx 7.5 \cdot 10^{-4}$ (obtained from Figure 3.4 using $w = 0.72\mu m$), and $\hat{\alpha}_3 = \alpha_3 n^2 \varepsilon_0 / 8\mu_0$ ($\alpha_3 = 0.04 cm^3 GW^{-2}$ is the 3PA coefficient). The simulation results and the experimental intensity patterns for three different input power levels are presented in Figure 5.7. Overall the agreement between experiment and theory is very good.
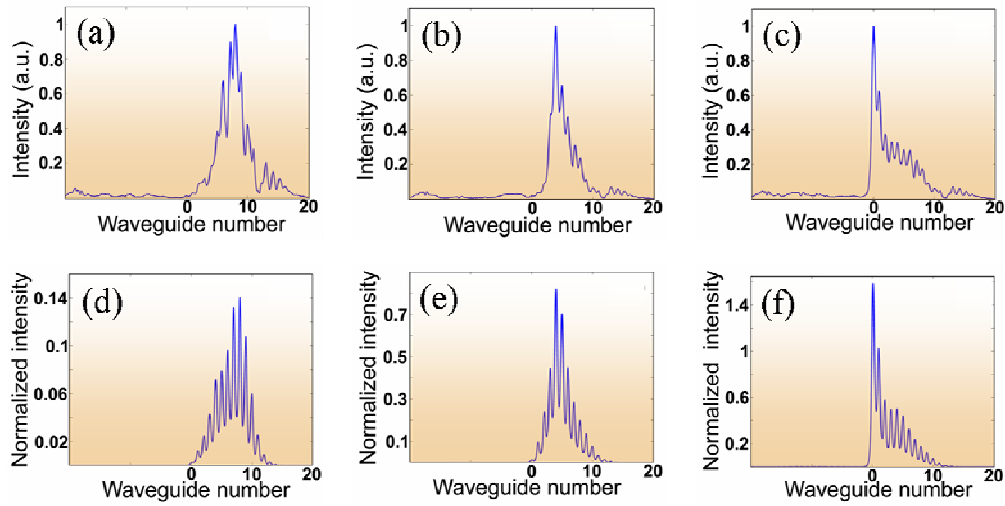
Figure 5.7: Measured output intensity when the boundary channel of the waveguide array was excited with a beam of (a) 450W (low power), (b) 1300W and (c) 2100W peak power. (d) - (f)

59

are the corresponding simulated intensities for 280W (low power), 1260W and 2200W of input power, respectively.

Another set of experiments was done to verify that the surface soliton is a nonlinear eigenmode at the interface using a wide, strongly asymmetric input beam of approximately 50μm FWHM. The beam was injected into two different positions of the AlGaAs array, namely with the maximum of the beam profile in the middle of the array, and the maximum located at the boundary waveguide site. In the latter case the steep side of the beam intensity profile was facing the edge of the array in order to prevent a significant amount of radiation from leaking into the continuous region. The corresponding measured output intensities, as well as input beam shape and position, are shown in Figures 5.8(b), (c). Also, for comparison, the experimental result for a wide symmetric input beam injected in the middle of the array is given in Figure 5.8(a).
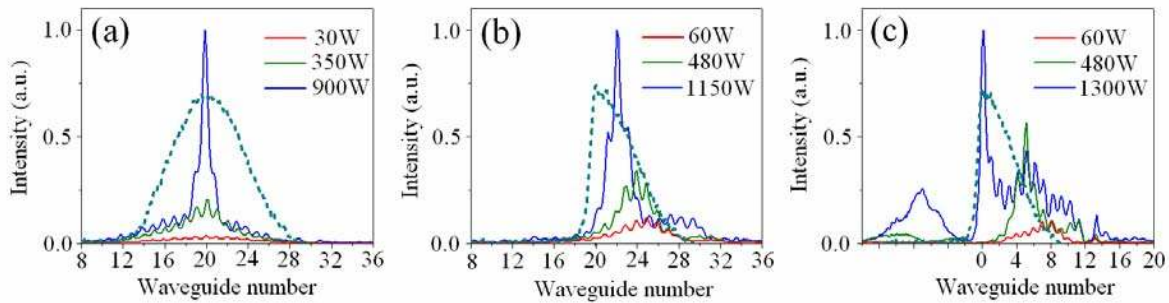
Figure 5.8: Measured output intensity patterns when (a) a wide symmetric beam is injected into the middle of the array, (b) an asymmetric beam is injected in the middle of the array, and (c) the peak of the asymmetric input beam is aligned with the first ($n = 0$) channel site. Outputs for three different powers for each case are shown. Input beam intensity is identified by dashed curve.

Figure 5.8(a) shows that, as power is increased, the well-known symmetric discrete soliton centered on the input beam peak is formed. Unlike this, for the asymmetric input beam (Figure 5.8(b)) the resulting discrete soliton is centered two waveguide sites away from the position of the maximum of input intensity, near the centroid position of the input energy. However, when such a beam is injected near the interface as shown in Figure 5.8(c), a discrete surface soliton is always formed at the first channel site. This proves that discrete surface solitons are indeed the nonlinear eigenmodes near the interface. Note that the sharp falling edge of the input beam was not steep enough to prevent the excitation of modes in the slab waveguide. The input power in case (c) was increased further to well above the discrete surface soliton threshold. The results shown in Figure 5.9 for this case (i.e. 2200W of peak power) indicate that a second discrete soliton is formed at the position of the secondary broad peak of the intensity pattern for input power of 1300W.
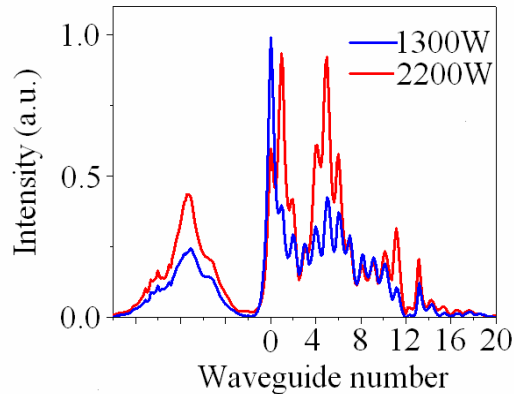
Figure 5.9: Measured output intensity patterns when the peak of the asymmetric input beam is aligned with the first ($n = 0$) channel site and the input power is increased from 1300W to 2200W.

This occurs because there is now more than enough power in the input beam to form two discrete solitons. Since the two solitons are coherent and in-phase with each other, they attract and hence the surface soliton is shifted by one channel inside the array.

5.3. Power threshold measurements

In this section the key property of discrete surface solitons, i.e. the existence of a power threshold is investigated in detail. As was already mentioned in the previous section, a rapid collapse of the diffraction pattern toward the excitation channel in Figure 5.6 is a clear indication of the threshold behavior expected of surface solitons. Moreover, theory predicts that solutions of the DNLS Equation 5.1 can be obtained for solitons localized at other waveguide sites, e.g. at the $n = 1, 2, 3$ etc. channels. The cw power threshold of these solutions goes to zero as n (the site where the soliton peak resides) increases. Therefore, the purpose of the experiments described in this section was to measure the threshold's dependence on the distance away from the boundary as well as its correlation to the inter-channel coupling strength.

The initial observation of discrete surface soliton formation was performed with TE polarization. However, the simulations showed that the thresholds for soliton formation were smaller for the TM polarization. Experiments were performed with TM polarization, and strongly localized discrete surface solitons with single channel excitation were also observed in that case. A comparison of the results for the evolution of the solitons for the two polarizations is shown in Figure 5.10. It was consistently found that the threshold power for TM case was lower than for TE, in agreement with the simulations. Given the influence of three photon absorption discussed later in this chapter, the TM polarization was chosen for most of the experiments.
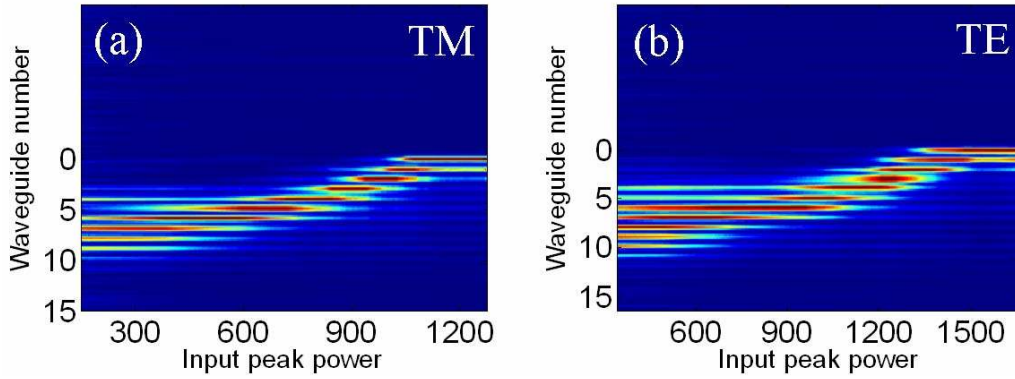
Figure 5.10: The evolution with input power of the intensity distribution across the array measured at the output facet for (a) TM and (b) TE polarized inputs when the boundary ($n = 0$) channel was excited.

New AlGaAs samples, 1.35cm long waveguide arrays, each consisting of 50 weakly coupled ridge waveguides and surrounded on both sides by a 1D slab waveguide were fabricated for these experiments. Several arrays with constant period $D = 10 \mu m$ but different widths of the waveguide ridges, namely $d = 2.4$, 3.4, 4.4 and $5.4 \mu m$, were fabricated. The etch depth was $w = 1.1 \mu m$ which corresponds to the index contrast $\delta \approx 2 \cdot 10^{-3}$, three times larger than in the first experiment discussed above. In order to understand how the waveguide width affects the inter-channel coupling constant, the intensity profiles of the TM fundamental modes of isolated waveguides were simulated. The modal intensity profiles for the $2.4 \mu m$ and $4.4 \mu m$ wide waveguides are shown in Figure 5.11. It is clearly seen that the mode profile for the $2.4 \mu m$ channel is more spread out in a horizontal direction. Therefore, when two $2.4 \mu m$ waveguides are brought to close proximity with each other, they will experience a higher evanescent mode-field overlap than the two $4.4 \mu m$ wide guides (given that the center-to-center

separation is kept constant). This, in turn, will result in a higher coupling constant for an array with $2.4\mu m$ wide channels.
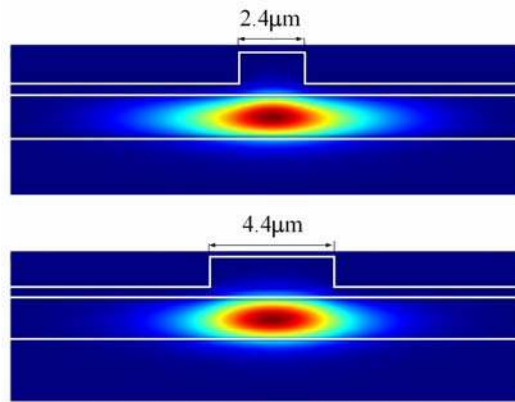
Figure 5.11: Intensity profile of the fundamental mode of a single waveguide for $d = 2.4\mu m$ (top) and $d = 4.4\mu m$ (bottom).

A systematic study of the dependence of the coupling constant and of the mode effective area on ridge width was performed. The coupling constants in the available samples were found using the technique described in Section 3.3, i.e. the diffraction patterns for single channel excitation were recorded at low powers in the middle of each array and the coupling constants were obtained by fitting these patterns with analytical solution given by Equation 2.40. The effective area was calculated using Equation 2.36. The obtained results are presented in Table 2.

Table 2: The coupling constant and effective mode area for the four ridge widths.

Ridge width (μm)	Coupling constant (m^{-1})	Effective mode area (μm^2)
2.4	520	17.0
3.4	445	14.8
4.4	420	14.2
5.4	430	14.4

The comparison of measured and calculated values for the coupling strength in Figure 5.12 shows the excellent agreement between calculations and experiment. Note that there is a minimum in the coupling constant at a ridge width of approximately $4.5\,\mu m$.
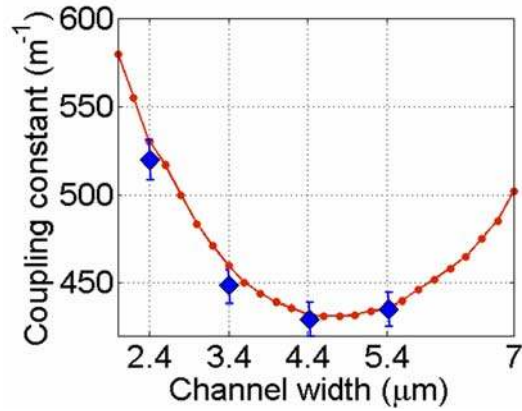
Figure 5.12: The dependence of the coupling constant C on the ridge width for the fixed center-to-center channel spacing of 10μm. Data given by diamonds ◆, and calculations by the red curve.

Based on these array parameters the curves which define the existence region for discrete surface solitons were calculated for solitons peaked at channels at varying distance (channel number) from the interface. An example is given in Figure 5.13(a) for the 4.4μm ridges. As

65

expected, the threshold powers, shown by squares in Figure 5.13(b), fall with increasing channel number and approach asymptotically the power required to form discrete solitons deep inside the array.
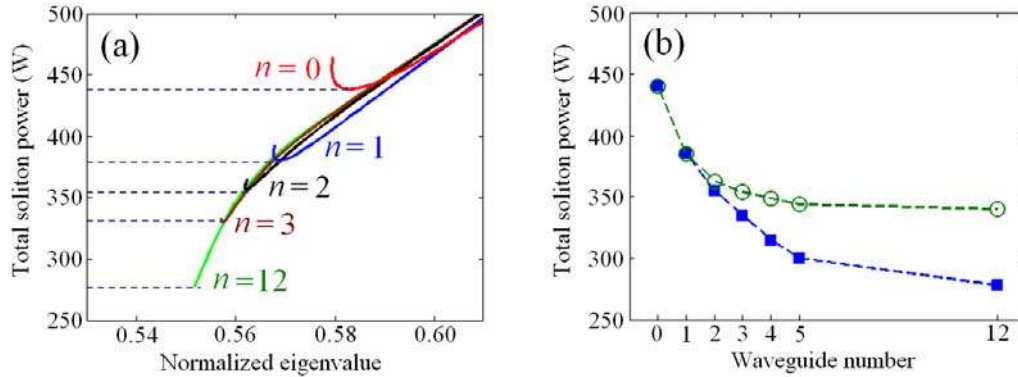
Figure 5.13: (a) The existence curves of discrete solitons centered on various channels "n" versus the nonlinear wavevector shift. (b) Threshold powers corresponding to the minima of the existence curves (squares □), and the powers of essentially single channel surface solitons (circles O), versus waveguide number.

The corresponding soliton fields at the threshold are shown in Figure 5.14, and give a great deal of insight into the threshold behavior. For $n = 0$, the solitons are strongly confined to the boundary channel and the fields are strongly asymmetric because they decay exponentially with the single channel decay constant into the 1D slab waveguide. As the channel number at which the soliton fields peak is increased, the fields become both progressively wider and more symmetric. By $n = 12$, the fields are completely symmetric and indistinguishable from those deep inside the array. As the total power of the solitons for $n \geq 1$ is increased, they move up the curves in Figure 5.13(a), eventually acquiring a confinement equivalent to the case $n = 0$, but with more symmetric envelopes.

66
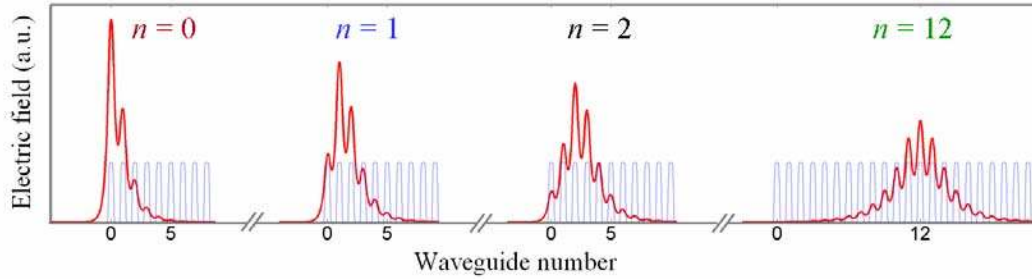
Figure 5.14: The calculated electric field distributions of discrete surface solitons peaked at different channels "*n*", at power threshold.

There are problems associated with identifying the threshold power in the experiments. First, the use of pulses leads to "smearing" of the results because temporal pulse contains a distribution of powers ranging from zero to the peak power. This leads to "tails" in the output distributions which can make it difficult to differentiate solitons from the low power linear diffraction which "reflects" off the boundary, see Figure 5.2. Second, the solitons broaden at threshold with increasing "*n*" and for each "*n*" slowly collapse in width with increasing power. This makes it difficult to define a single criterion for "threshold". Third, in the limit of discrete spatial solitons spanning many channels, equivalent to the continuum limit for Kerr spatial solitons in 1D slab waveguides, the product of the soliton power and soliton width is a constant. Although in the discrete case the confinement of the surface soliton also increases with increasing power, the theoretical power-width relationship for the excitation of discrete solitons a few channels wide is not analytical.

Hence we adopted a different philosophy to show that the presence of the surface results in power thresholds which decrease for surface solitons peaked on channels progressively further from the boundary. Note that the fields at the threshold powers for the *n* = 0 and 1 already correspond to a soliton strongly confined to one channel. We define the threshold power for a

strongly confined soliton as the minimum input power at which the peak output intensity in the excitation channel exceeds 3 times that of its adjacent secondary channels. We calculated the cw power required for generating such strongly confined discrete surface solitons. This is equivalent to moving up the existence curves to higher powers as identified in Figure 5.15(a) where the criterion for strong confinement was satisfied at the points **A**, **B** etc. In Figure 5.13(b), this gave another (green circles) total power versus channel number curve. Note that for the first few values of "n" this condition corresponds quite closely to the actual power threshold minimum. On the other hand, for $n \geq 2$ this definition starts to deviate progressively more from the theoretical power threshold, see Figure 5.13(b).
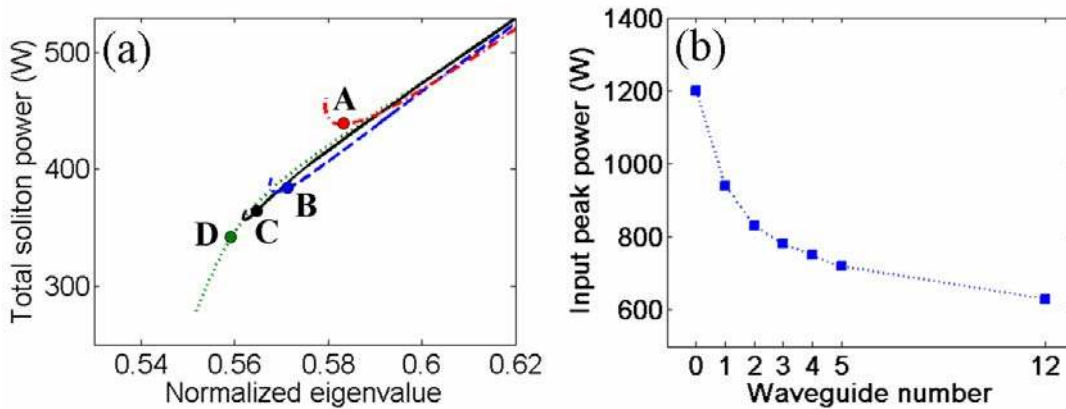
Figure 5.15: (a) Total power for steady state (cw) surface soliton solutions peaked at $n = 0$ (red dash-dot curve), $n = 1$ (blue dashed curve), $n = 2$ (black curve), and $n = 12$ (green dotted curve) channels. The location of the "single channel" discrete solitons are identified by the points A ($n = 0$), B ($n = 1$) etc. (b) Calculated input peak power required for the formation of a "strongly localized discrete soliton" versus channel number.

However, when the effects of pulse propagation, GVD, linear and nonlinear loss are taken into account in BPM simulations, the predicted curve for this "strongly localized discrete soliton"

68

threshold shown in Figure 5.15(b) resembles very closely that for the minima of the P - μ curves in Figure 5.13(b). In the pulsed case the required peak powers are higher since only a single channel is excited and this power must be shared by all the channels defining the soliton and by the "diffraction tails". This "strongly localized surface soliton" threshold was adopted as the experimental parameter to measure. The calculated intensity distributions of these solitons (corresponding to the points **A**, **B** etc in Figure 5.15(a)) are shown in Figure 5.16, and indeed it was found relatively easy to identify these intensity distributions experimentally.
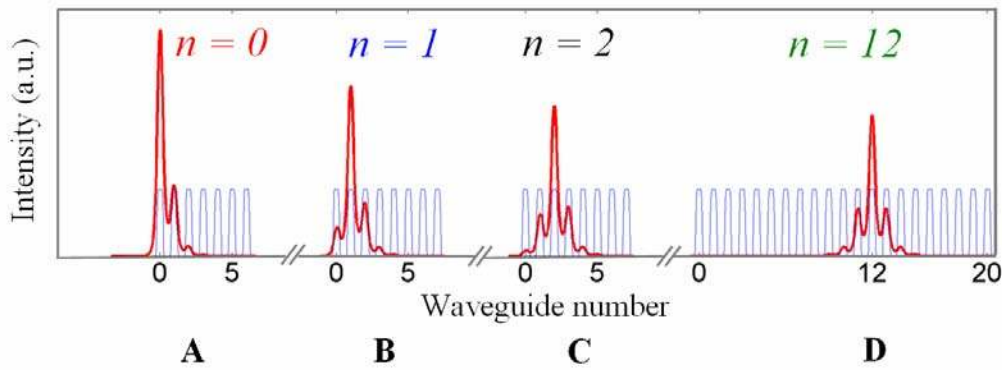
Figure 5.16: The intensity distributions associated with the "single channel" discrete solitons as a function of channel number.

In the experiment the first six ($n = 0 - 5$) and the $n = 12$ channels were individually excited and the intensity distributions at the sample's end facet were recorded. As the input power was increased, the soliton states were identified by almost complete confinement of power in the excitation channel. Examples of the measured output patterns associated with the single channel solitons localized at the $n = 0$, 2 and 12 channels for the array with $d = 4.4 \mu m$ are shown in Figures 5.17(a) - (c), respectively. Note that in all three cases the solitons are strongly confined. Just as in the results of Figure 5.6 for the $n = 0$ channel, further increase in the incident power did

not produce significantly better confinement. These experimental results were in excellent agreement with the soliton intensities obtained from BPM simulations, see Figures 5.17(d) – (f).
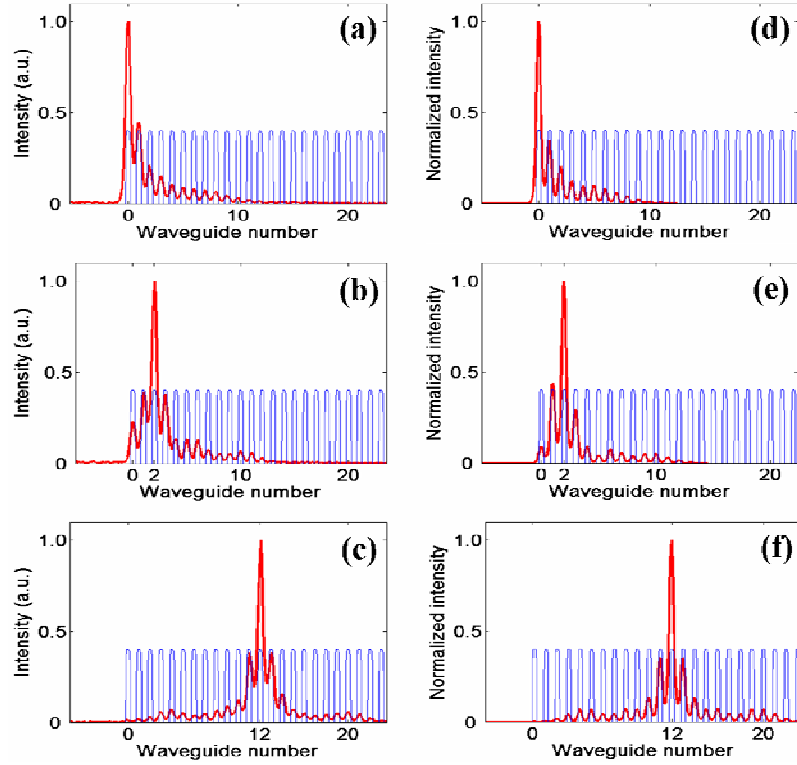
Figure 5.17: Recorded output intensities corresponding to strongly localized discrete solitons when the (a) $n = 0$, (b) $n = 2$, and (c) $n = 12$ channels of the AlGaAs array were excited with the peak power of 1250W, 920W and 660W, respectively. (d) - (f) are the corresponding BPM simulated intensities.

A comparison of the measured and calculated (Figure 5.15(b)) input peak powers for the excitation of strongly localized surface solitons is shown in Figure 5.18, and the agreement is excellent. It is also important to realize that the Kerr nonlinear and 3PA coefficients used in the calculations are themselves only known to an accuracy of $\pm 10\%$.
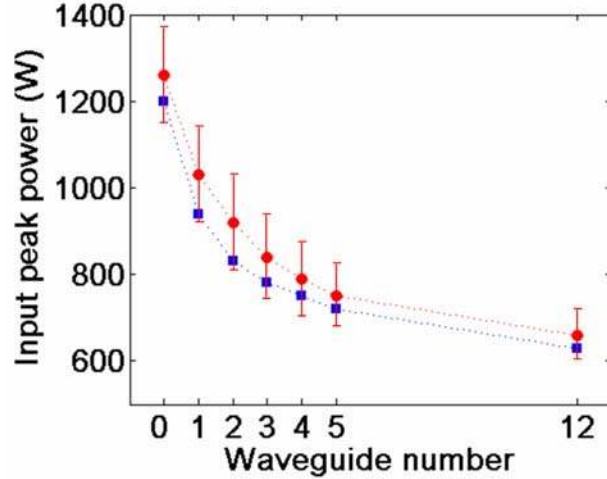
Figure 5.18: Measured (circles) and calculated (squares) input peak powers as a function of a soliton localization site for an array with $d = 4.4 \mu m$.

Note that the experimental powers required for the excitation of these surface solitons are higher by a factor of approximately 2 - 2.5 than the threshold powers defined in Figure 5.13(b). This is a consequence of many factors, first of all the pulsed nature of the experiment and nonlinear losses. The total linear losses in our 1.35cm long AlGaAs samples measured using the Fabry-Pérot technique (see Section 3.3 of Chapter 3) were found to be approximately 18%. As the measured throughput of the samples has shown, at high input powers the dominant absorption mechanism was the nonlinear 3PA loss. This is quantified in Figure 5.19 which shows the net throughput as a function of the input peak power in the surface soliton experiment for the array with $d = 4.4 \mu m$ (the corresponding intensity evolution with input power was shown in Figure 5.10(a)).
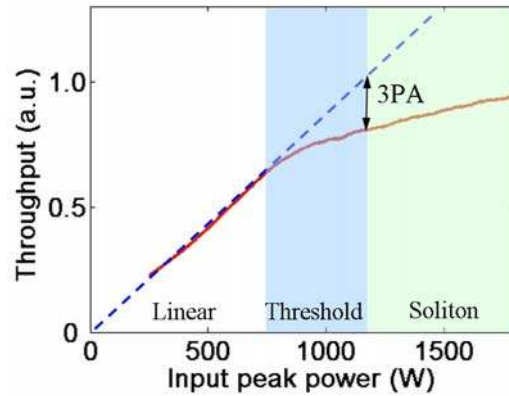
Figure 5.19: Throughput measurements (red curve) for the array with 4.4μm wide ridges. Linear slope is indicated by a dashed line.

Until the threshold region is reached, the slope of the throughput curve is constant which corresponds to the linear regime without 3PA. This is expected because in this region discrete diffraction process results in spreading of power over many channels thus prohibiting the formation of high intensities necessary for significant 3PA. In the threshold region, where the narrowing of the intensity pattern occurs, the 3PA becomes noticeable. Finally, above 1200W the discrete surface soliton is formed with most of its power localized in a single waveguide. At this point about 25% of the input power is lost because of 3PA as indicated by the deviation of the throughput curve from the linear slope in Figure 5.19. The progressively faster nonlinear loss growth at powers beyond 1200W explains why the confinement of surface solitons is not improved significantly with further increase in input power. All these three factors, i.e. the fraction of power in discrete diffraction due to the pulsed nature of the excitation (~30%), linear losses (~18%), and the 3PA nonlinear losses (~25%) more than double the power requirements for observation of discrete surface solitons.

Similar experiments were performed in each of the other three waveguide arrays listed in Table 2 with different channel widths for the $n = 1 - 5$ and 12. A summary of the experimental

results for the input power required for clean "strongly localized soliton" formation is given in Figure 5.20(a). There the peak input power is plotted versus soliton waveguide site for four different channel widths. It is clear for each ridge width, that the soliton generation condition for $n \geq 4$ (and corresponding input power level) is essentially the same as measured for the soliton deep inside the array ($n = 12$). This is a consequence of strong confinement so that the solitons peaked at the $n \geq 4$ channels are only weakly influenced by the presence of the boundary. To study the correlation of power thresholds with the coupling strength, the variation of the calculated and measured coupling constant with the ridge width is given again in Figure 5.20(b).
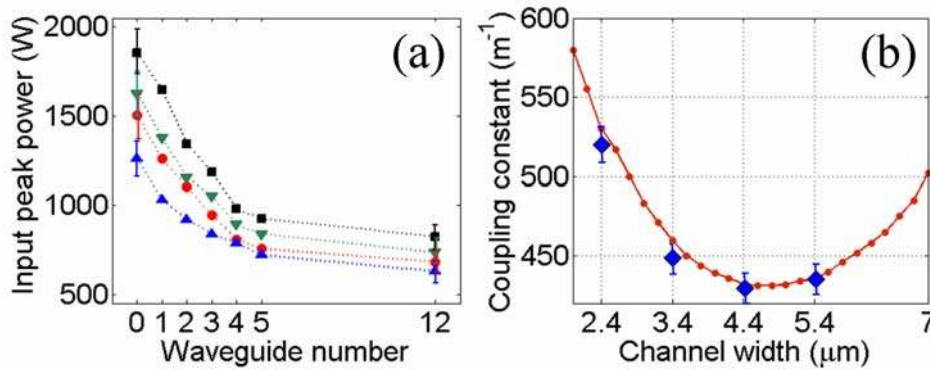
Figure 5.20: (a) Input peak power required for a strongly localized soliton formation versus localization site for the samples with $d = 2.4 \mu m$ (squares), $3.4 \mu m$ (circles), $4.4 \mu m$ (triangles), and $5.4 \mu m$ (inverted triangles). (b) Calculated (dots) and experimentally found (rhombi) inter-channel coupling constants as a function of the ridge width.

It is noteworthy that for the soliton in each particular channel the corresponding input power level was the lowest for $d = 4.4 \mu m$, and the highest for $d = 2.4 \mu m$, as indicated in Figure 5.20(a). This is not surprising because, as shown in Figure 5.20(b), of all four array geometries these two arrays have the smallest and the highest coupling constants ($430 m^{-1}$ and

$520 m^{-1}$, respectively). And in general, the stronger the coupling between adjacent waveguides the higher the input power necessary for nonlinearity to decouple the excitation channel from its neighbors and form a soliton. This implies that the power threshold is inversely proportional to the coupling length. However, the result for a ridge width of $5.4 \mu m$ belies such a simple interpretation since the threshold power for this case rose much faster than the increase in the coupling constant. The effective mode area also rises (Table 2) for this case, but not enough to explain the large increase in threshold power. Hence, additional factors must play a role with the most probable one being the approximate nature of the coupled mode analysis.

CHAPTER SIX: LINEAR MODES AT A HETERO-JUNCTION OF TWO ARRAYS

The recent advances in fabrication technologies have allowed manufacturing of artificially structures materials (called meta-materials) where light propagation properties can be strongly affected and even controlled [91]. Photonic crystals are probably the most prominent example of a meta-material where such properties as diffraction and refraction of light wave can be varied to a large extent [92, 93]. A waveguide array is another example of a meta-material and exhibits many new phenomena due to its unique diffraction properties. To date, the unique linear optical properties of waveguide arrays such as anomalous diffraction, multiple allowed bands, Bloch oscillations, the discrete Talbot effect etc. have been reported [73, 75, 94, 95]. Furthermore, the disruption of translational symmetry by a defect buried in an "infinite" waveguide array has been predicted and observed to lead to "defect" modes [96 – 98].

In previous chapters, only single arrays comprised of identical waveguides were considered. This chapter will focus on the linear properties of the interface between two dissimilar waveguide arrays, i.e. a *waveguide array hetero-junction*. More specifically, the existence of *linear* propagating optical modes located in *k*-space in the band gaps of the composite structure are studied both theoretically and experimentally for the first time.

6.1. Theory of linear interface modes

Consider a 1D waveguide array hetero-junction shown in Figure 6.1(a). This structure is composed of two dissimilar semi-infinite waveguide arrays joined together and separated by the gap d_g. The scanning electron microscope (SEM) image of the real 2D cross-section of such a hetero-junction is given in Figure 6.1(b). As before, to simplify the theoretical analysis, this 2D geometry is reduced to the 1D geometry of Figure 6.1(a) using the effective refractive index method described in Section 2.4.
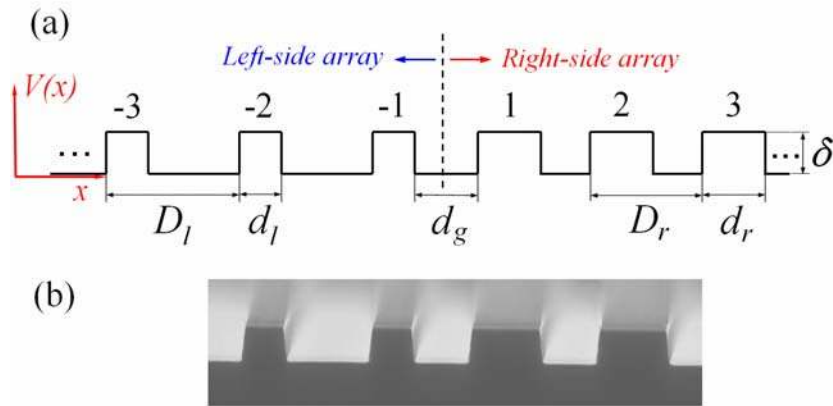
Figure 6.1: (a) A 1D refractive index potential of a two-array hetero-structure. (b) SEM image of the AlGaAs sample facet.

The system of linear coupled mode equations that describes the evolution of complex modal field amplitudes for this structure can be written as

$$i\frac{da_n}{dz} + C_\ell\left(a_{n+1} + a_{n-1}\right) = 0 \quad (n \le -2)$$

$$i\frac{da_{-1}}{dz} + C_\ell a_{-2} + C_{\ell \to r}a_1 = 0 \quad (n = -1)$$

$$i\frac{da_1}{dz} + C_{r \to \ell}a_{-1} + C_r a_2 = 0 \quad (n = 1) \tag{6.1}$$

$$i\frac{da_n}{dz} + C_r\left(a_{n+1} + a_{n-1}\right) = 0 \quad (n \ge 2),$$

where we have four different coupling constants: C_ℓ (between neighboring channels of left-side array), C_r (between channels of right-side array), $C_{\ell \to r}$ (between the two interface channels from left to right) and $C_{r \to \ell}$ (between the two interface channels from right to left). The two interface channels are sufficiently different so that the coupling coefficients from left to right, and from right to left, differ significantly [56]. Because the analytical solution of Equation 6.1 could not be found, the linear propagation within and between the two arrays was analyzed using the following paraxial equation of diffraction

$$i\frac{\partial E}{\partial z} + \frac{1}{2k}\frac{\partial^2 E}{\partial x^2} + k_0\delta V(x)E = 0, \tag{6.2}$$

where $E(x,z)$ is the slowly varying electric field envelope, δ is the effective refractive index contrast, and $V(x)$ is the normalized index potential.

The spatial impulse response for the single channel excitation of the boundary waveguides of the two arrays was found using the BPM code based on Equation 6.2. The hetero-junction samples were originally designed for observation of the interface discrete surface solitons discussed in the next chapter, and the design considerations will be described there. The following composite structure parameters which reflect the available samples were used in the simulations: the period of each array $D_\ell = D_r = 10\mu m$, the channel widths $d_\ell = 2\mu m$ and

77

$d_r = 5\mu m$, $\delta = 2 \cdot 10^{-3}$, and the spacing between the two arrays $d_g = 5$, 3 and $2\mu m$. Note that by using the same inter-channel spacing within the two arrays, the size of their Brillouin zones is kept identical. The simulated beam propagation dynamics for excitation of the single boundary channels for three different values of the inter-array spacing is shown in Figure 6.2.
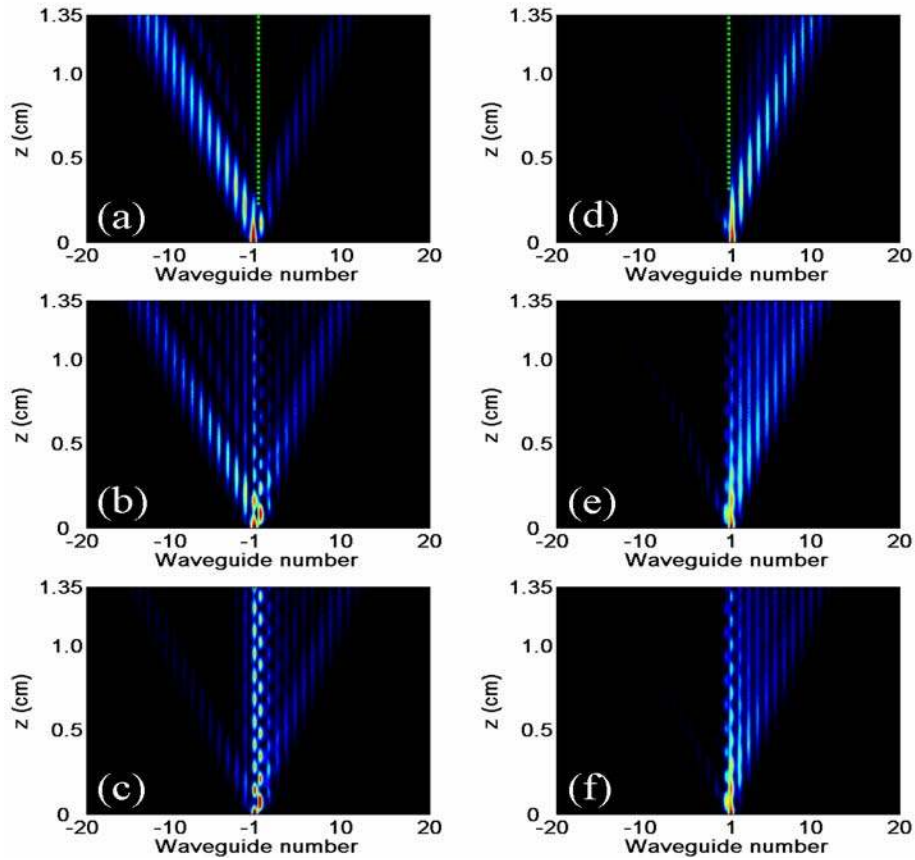
Figure 6.2: BPM simulation of the beam propagation for the excitation of a single boundary channel on the left (a) - (c) and on the right (d) – (f) from the interface. The inter-array spacing is $d_g = 5\mu m$ (a), (d); $3\mu m$ (b), (e); and $2\mu m$ (c), (f).

Clearly for $d_g = 5\mu m$ (Figures 6.2(a) and (d)), the tunneling across the gap between the two arrays is negligible and the discrete diffraction patterns are almost identical to that shown in

Figure 5.2(a) for the array-continuum interface. When the inter-array spacing is reduced to $3\mu m$, the coupling between the boundary channels becomes significant for the excitation of the boundary channel of the left-side array (Figure 6.2(b)). Note that a weak localization occurs at the interface characterized by a periodic exchange of energy between the boundary channels which dies off with propagation distance via discrete diffraction into both arrays. On the other hand, as Figures 6.2(e) shows, some coupling also occurs across the gap to the left-side array from the right-side array, leading again to a (weaker) periodic energy exchange between the boundary channels decaying only into the right-side array. Finally, further decrease of d_g to $2\mu m$ results in strong coupling between the two boundary channels with localization of power at the interface. Note that the localization is stronger for the excitation of the left array boundary channel (Figure 6.2(c)) and that in both excitation geometries the discrete diffraction occurs preferably into the right-side array. These localization results suggest that when d_g is sufficiently small the array hetero-junction can support linear optical modes propagating along the interface.

It can be formally shown via Floquet-Bloch analysis of the composite array that the band diagram of the hetero-structure involves essentially the bands of the individual semi-infinite arrays with the possible addition of linear surface modes which lie either above the highest lying band; in the gap between the bands, or below both first bands [54]. Figure 6.3(a) shows a typical calculated band structure of the array hetero-junction which can support linear surface waves. Here the first-order bands of the right- and left-side arrays are represented by the red and the blue upper curves, respectively. Also, a part of the second band of the right-side array is shown in red at the bottom of the plot.
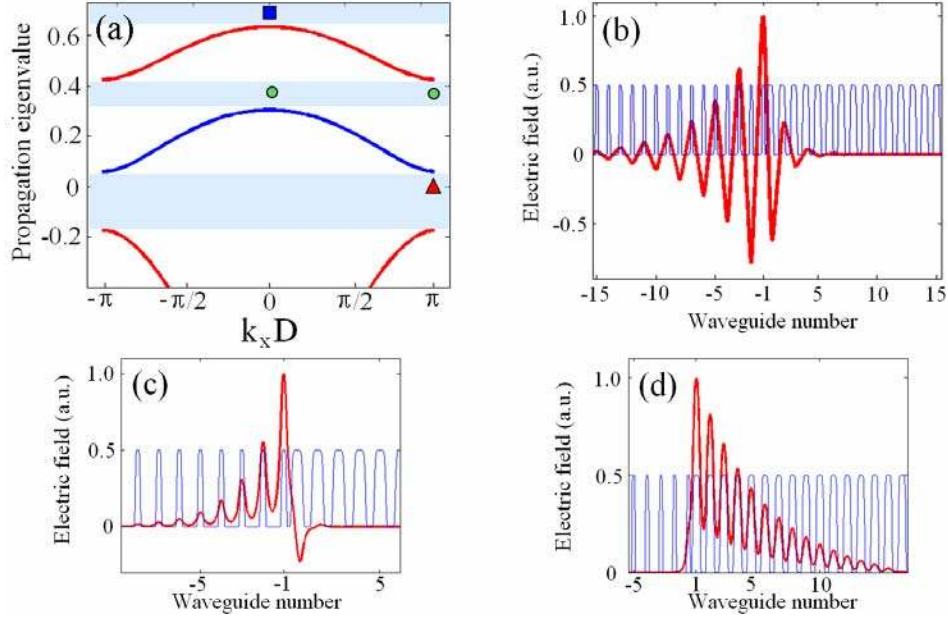
Figure 6.3: (a) Band diagram of the composite array. The locations of eigenvalues are shown for staggered/staggered (triangle), in-phase/staggered (circles), and in-phase/in-phase (square) linear modes. (b) - (d) are the corresponding electric field distributions of these modes.

In order to quantify the various electromagnetic modes supported by the composite structure, Floquet-Bloch analysis of Equation 6.2 was performed numerically. Finite difference techniques were used to identify the linear eigenmodes localized at the interface by assuming stationary solutions to the of the form

$$E(x,z) = \phi(x)\exp(i\lambda z), \tag{6.3}$$

where λ is the propagation eigenvalue of a particular mode and $\phi(x)$ is its transverse electric field profile. For the specific hetero-junction parameters mentioned above, only one interface mode was numerically found for $d_g = 2\mu m$. The mode eigenvalue indicated by a triangle in Figure 6.3(a) is located at the edge of the Brillouin zone in the gap between the first band of the left-side array and the second band of the right-side array. The electric field distribution of this

mode is shown in Figure 6.3(b). It has a staggered profile in either array (i.e. fields are π-out-of-phase in neighboring channels). The stronger the coupling between the two arrays, the deeper the mode eigenvalue lies into the gap below the first band of the left array and the narrower the envelope of the mode field distribution.

Numerical simulations have also revealed that for different hetero-junction parameters, the gaps between the bands can be tuned, and linear modes of other symmetry types are also possible. These include in-phase/in-phase (fields are in-phase in the adjacent channels in each array) and in-phase/staggered (fields in the adjacent channels are in-phase in the left-side array while staggered in the right-side array). The typical electric field distributions of these modes are shown in Figures 6.3(c) and (d) with the schematic locations of their eigenvalues given by circles and a square in Figure 6.3(a). The possibility for the existence for each type of linear interface modes was investigated numerically by varying within reasonable limits the effective index contrast δ and the spacing d_g between the two arrays. All other hetero-structure parameters were kept constant ($D_\ell = D_r = 10 \mu m$, $d_\ell = 2 \mu m$ and $d_r = 5 \mu m$). The results of the calculations are summarized in Figure 6.4. As one can see, there is a region without surface modes of any kind at all; regions where one mode type exists and regions which can support two different types of linear surface modes where the individual existence regions overlap. In this last overlap case, the appropriate surface mode can be excited by tailoring the input field to the mode structure. The location of the staggered/staggered mode discussed earlier is shown by a red dot on the diagram. The smallest array spacing in the existing samples was too large to excite the in-phase/in-phase stable mode. However, a leaky version of this mode could have been at least partially responsible for the localization seen in Figures 6.2(e) and (f). This leaky mode would have a longer tail from the boundary into the right-side array than into the left-side array,

81

resulting from the closer location of the mode eigenvalue to the top of the first band of the right-side array compared to that of the left-side array.
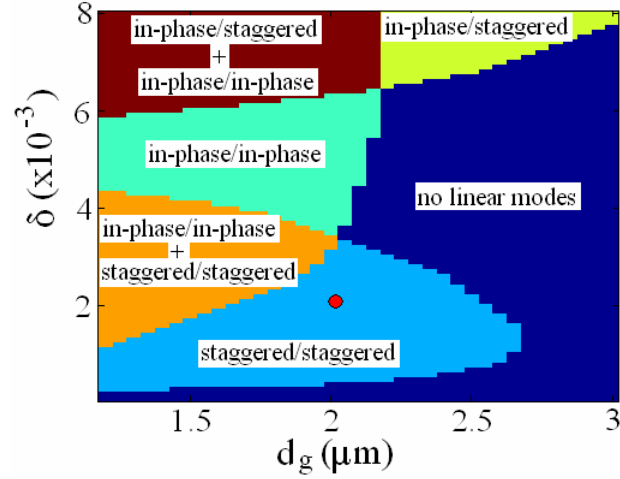
Figure 6.4: The regions of existence for interface modes with in-phase/in-phase, in-phase/staggered and staggered/staggered field distributions. The red circle identifies the sample geometry for which the surface mode is predicted in one of the available samples.

6.2. Experimental results

In fabrication, the following sample design parameters were used: $D_\ell = D_r = 10\mu m$, $d_\ell = 2\mu m$, $d_r = 5\mu m$, $w = 1.1\mu m$ (corresponds to $\delta \approx 2 \cdot 10^{-3}$), and the spacing between the two arrays $d_g = 5$, 3 and $2\mu m$. The real parameters of the AlGaAs samples measured using SEM deviated slightly from the design values in terms of ridge widths and spacing d_g. They are: $d_\ell = 2.4\mu m$, $d_r = 5.4\mu m$, and $d_g = 5.2$, 3.4 and $2.2\mu m$. However, the main experimental results on observation of the predicted linear interface mode were not significantly affected by these differences.

First, discrete diffraction under single channel excitation condition was investigated experimentally for the three available samples. Radiation at 1550nm wavelength from a low power cw source (HP81680A diode laser) was shaped spatially to match the mode profile of an isolated waveguide and focused onto the boundary channels on either side of the interface. The intensity distributions at the samples' end facets were recorded with an InGaAs line array camera. The resulting discrete diffraction patterns shown in Figure 6.5 were in excellent agreement with the simulation results of Figure 6.2. As predicted numerically, the excitation of a leaky surface wave was observed for the smallest gap.
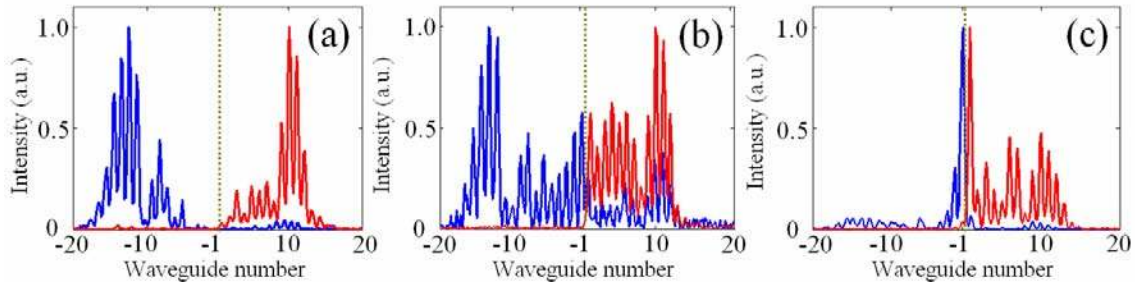
Figure 6.5: Intensities recorded at the sample's output facet for the inter-array spacing d_g = (a) $5.2 \mu m$, (b) $3.4 \mu m$, and (c) $2.2 \mu m$. The boundary channels of the left (blue curves) and of the right (red curves) arrays were excited.

To observe the stable staggered/staggered linear interface mode experimentally, the best shape of the input beam needs to be found. Apparently, despite the significant localization of energy near the interface in Figure 6.5(c), single waveguide excitation is not the best way to do this. Of course, the best approach would be to shape the input beam to match exactly the mode field profile shown in Figure 6.3(b). The simulated propagation dynamics under these input conditions is given in Figure 6.6(a) and shows stable propagation of the linear mode for a

sufficiently long distance with almost no energy radiated away form the boundary region. However, shaping the input beam exactly is a challenging task. Therefore, in order to excite the linear mode, another approach was chosen. The calculated interface mode fields are π-out-of-phase in adjacent channels and the mode envelope spreads over a number of waveguides. Hence a beam tilted to produce a relative phase of π between waveguides and several channels wide should produce good coupling to the interface mode. First we verified this approach numerically. A Gaussian beam with FWHM of 35μm and a linear phase variation across its profile was chosen as an input for the composite array with $d_g = 2.2\mu m$. The simulated propagation for a 3cm distance shown in Figure 6.6(b) revealed that after some distance the input beam evolves into the intensity distribution of the interface mode.
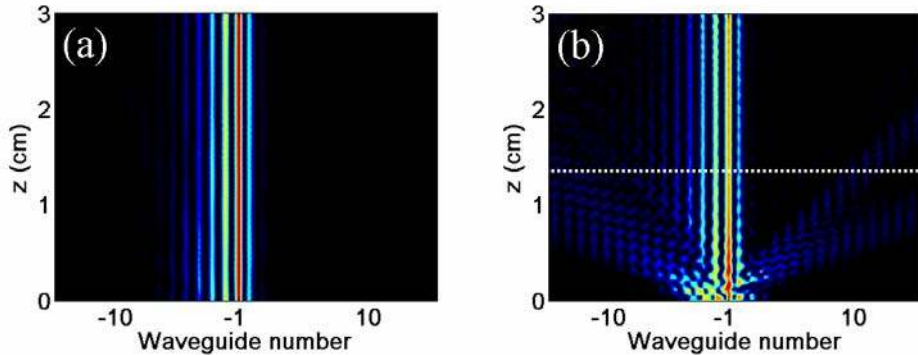
Figure 6.6: BPM simulation of (a) stable propagation of the staggered/staggered mode when the beam with the exact mode-field distribution is launched into the hetero-structure, (b) propagation dynamics of a 35μm wide tilted Gaussian beam injected at the interface location. The length of the actual sample is shown by a dotted line.

The simulations also show that the length of the real AlGaAs sample (1.35cm) indicated by a dotted line in Figure 6.6(b) would be sufficient to observe this mode.

In the experiment a Gaussian beam with FWHM of 35μm and tilted to produce a π phase difference between the adjacent channels was launched at the position of the first waveguide of the left-side array ($n = -1$) as shown by a black curve in Figure 6.7. The intensity distribution recorded at the sample's end facet is shown in red in the same plot. Its excellent agreement with the calculated intensity of the interface mode plotted in Figure 6.7(b) proves that this linear mode does indeed exist at the array hetero-junction.
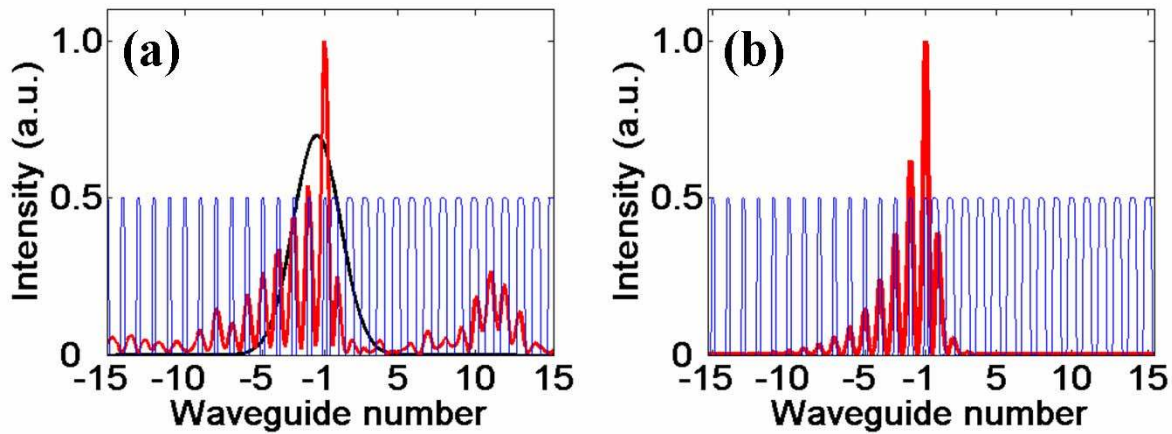
Figure 6.7: Experimentally measured (a) and calculated (b) intensity distribution associated with a staggered/staggered mode. Black curve in (a) is the intensity distribution of the input beam.

In a second set of experiments, the relative phase $\Delta\theta$ between adjacent channels was varied continuously by tilting a wide Gaussian beam (overlapping the interface) with respect to the sample's entrance facet, and the output intensity distributions were recorded. As was discussed earlier in the Section 3.3 regarding a regular waveguide lattice, this technique is known to yield the derivative of the first Bloch band's dispersion relation (the experimental results are shown in Figure 3.6). The results of the corresponding experiments for two hetero-junction samples with $d_g = 2.2 \mu m$ (proven to have an interface mode) and $d_g = 5.2 \mu m$ (predicted to

have no interface mode) are shown in Figures 6.8(a) and (b), respectively. The structure of these intensity patterns is similar because the individual waveguide arrays constituting the hetero-structures are the same. It is also more complicated compared to Figure 3.6 because the reflection off the boundary between the two arrays is now involved.
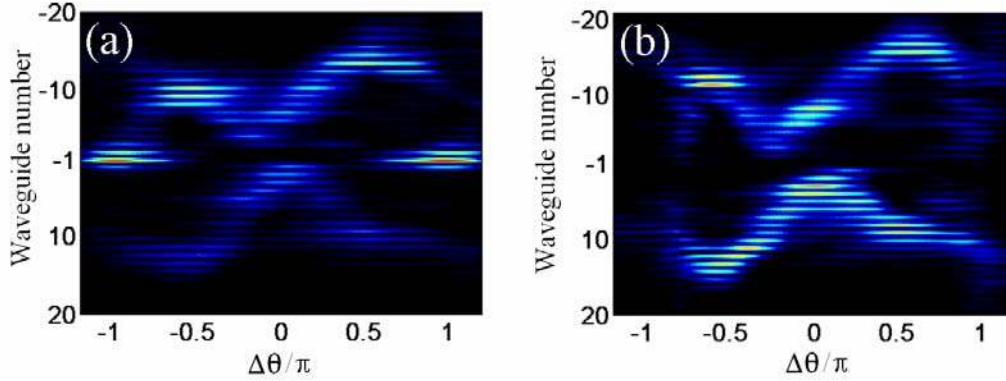
Figure 6.8: Measured output intensity of the composite array versus relative phase $\Delta\theta$ for (a) $2.2\,\mu m$ and (b) $5.2\,\mu m$ inter-array spacing.

Despite the similarity, the main difference between the two cases of different inter-array spacing is apparent. For $2.2\,\mu m$ gap between the arrays (Figure 6.8(a)), the formation of the linear mode is indicated by a strong localization of energy at the interface in the vicinity of $\Delta\theta = \pm\pi$ while at all other values of relative phase light diffracts away from the boundary. In contrast to this, Figure 6.8(b) shows that for $d_g = 5.2\,\mu m$ there were no signs of energy localization at the interface region for any value of relative phase.

These results clearly show that a linear interface mode propagating along the boundary between two dissimilar periodic structures can exist under appropriate conditions.

CHAPTER SEVEN: HYBRID INTERFACE SOLITONS

Besides the interface modes in the linear regime, the waveguide array hetero-junction can support a variety of nonlinear surface waves, namely the hybrid surface solitons predicted recently by Makris et. al. [54]. These solitons are referred to as "hybrid" because their two field components in the dissimilar arrays can propagate locked together as a composite self-trapped state, thus forming a hybrid surface soliton. It has been shown theoretically that three different types of hybrid solitons are possible with their propagation eigenvalues located inside different band gaps in the band diagram of the composite structure. In this chapter, the unique properties of these nonlinear surface waves are studied both theoretically and experimentally.

7.1. Introduction

The system under consideration in this chapter is the structure composed of two dissimilar semi-infinite waveguide arrays shown earlier in Figure 6.1. In the nonlinear regime, optical wave propagation in this system is governed by a paraxial scalar NLSE given by

$$i\frac{\partial E}{\partial z} + \frac{1}{2k}\frac{\partial^2 E}{\partial x^2} + k_0 \delta V(x)E + \gamma |E|^2 E = 0, \tag{7.1}$$

where again $E(x,z)$ is the slowly varying electric field envelope, δ is the effective refractive index contrast, $V(x)$ is the normalized refractive index potential of the composite structure, and γ is the Kerr nonlinear coefficient. The hybrid surface soliton solutions are numerically found

by using relaxation schemes based on the self-consistence method [99]. In this approach the following solutions to Equation 7.1 are assumed [54]

$$E(x,z) = \phi(x)\exp(i\lambda z), \tag{7.2}$$

where $\phi(x)$ is the transverse electric field profile and λ is the soliton eigenvalue, the nonlinear correction to the propagation constant due to nonlinearity. Using this method, three different types of hybrid surface soliton have been found. Based on the symmetry of their electric fields $\phi(x)$ and similar to the naming convention used in Chapter 6 for linear interface modes, these three soliton types are in-phase/in-phase, in-phase/staggered and staggered/staggered solitons.

To understand the difference between these three soliton solutions, it is necessary to consider the band diagram of the composite two-array structure. The typical calculated band diagram of the array hetero-junction is shown in Figure 7.1(a). Again, as in Figure 6.3(a), the first order bands of the right- and left-side arrays are represented by the red and the blue upper curves, and second band of the right-side array is partially shown in red at the bottom of the plot. It is noteworthy, that two types of hybrid soliton solutions, namely in-phase/in-phase and in-phase/staggered ones, were found for the self-focusing (i.e. $\gamma > 0$) Kerr-type nonlinearity while for the defocusing case ($\gamma < 0$) only staggered/staggered hybrid solitons exist. The nonlinear eigenvalues of in-phase/in-phase hybrid solitons shown by a square in Figure 7.1(a) were found to lie in the semi-infinite band gap above the first band of the right-side array in the center of the Brillouin zone. As a result, the soliton fields in adjacent channels are in-phase on either side of the interface. The in-phase/staggered soliton solutions have their eigenvalues inside the complete band gap between the first bands of the two arrays (circles in Figure 7(a)). The location of their eigenvalues implies that fields of the soliton's component in the left-side array are in-phase while the other part of the soliton, in the right-side array, is staggered. Finally, the eigenvalues of

staggered/staggered soliton solutions shown by triangle in Figure 7.1(a) were found to lie in the gap between the first band of the left-side array and the second band of the right-side array. The typical electric field distributions of these three types of hybrid solitons are shown in Figures 7.1(b) – (d). As was pointed out earlier, the existence of staggered/staggered solutions requires a defocusing Kerr nonlinearity. Since AlGaAs at a wavelength 1550nm has a positive Kerr coefficient, such solitons will be excluded from further discussions.
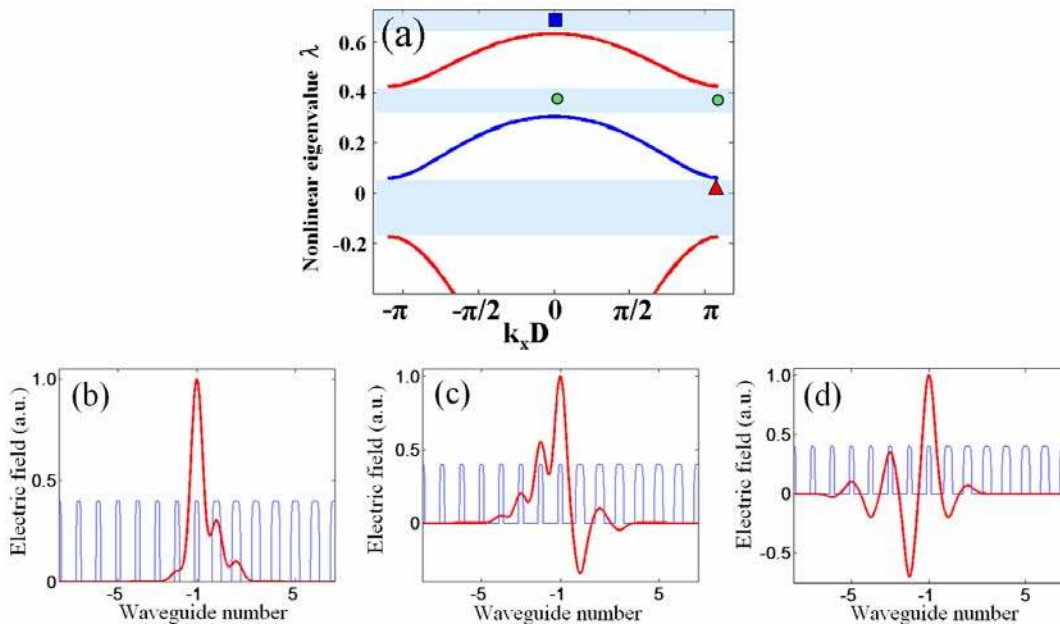
Figure 7.1: (a) Band diagram of the composite array. The locations of the eigenvalues are shown for staggered/staggered (triangle), in-phase/staggered (circles), and in-phase/in-phase (square) hybrid soliton solutions. (b) - (d) are the respective typical electric field distributions of these solutions.

It is important to note that, according to theory, in-phase/in-phase hybrid surface solitons exist regardless of the shape and relative position of the bands. However, in contrast to this universal case, in-phase/staggered solitons can only exist when the first bands of the two arrays

exhibit a minimum value of the band gap separating them. Such a band diagram was shown in Figure 7.1(a) but for a wide range of hetero-structure parameters this is not usually the case. Therefore, it is useful in the next section to establish the sample design considerations needed for observing hybrid interface solitons.

7.2. Sample design considerations

To find the condition for the existence of the gap between the two first-order bands, consider these two bands alone as shown in Figure 7.2.
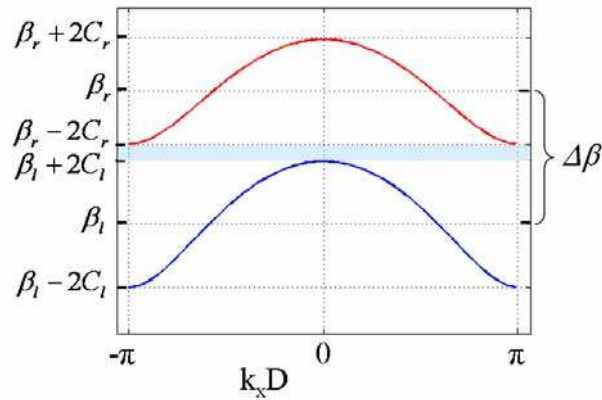
Figure 7.2: Band diagram of the composite array with only the two first order bands shown.

For the analysis, the coupled mode theory approach will be used. The dispersion relation for a 1D infinite waveguide array given by the Equation 2.43 predicts that the existence domain of the first-order band along the propagation wavevector axis (vertical axis in Figure 7.2) is centered on the value of the propagation constant β of the array's isolated waveguide and extends from $(\beta - 2C)$ to $(\beta + 2C)$. Therefore, the condition for the existence of a gap between the two bands in Figure 7.2 is given by

90

$$\beta_r - 2C_r > \beta_\ell + 2C_\ell, \tag{7.3}$$

where β_r and β_ℓ are the propagation constants, and C_r and C_ℓ are the coupling strengths of the right-side and left-side arrays, respectively. By rearranging its terms, Equation 7.3 can be rewritten as

$$\Delta\beta > 2(C_r + C_\ell), \tag{7.4}$$

Where $\Delta\beta = \beta_r - \beta_\ell$. Simple considerations suggest that all one needs to do to satisfy Equation 7.4 is to take arrays with sufficiently different ridges (to have a high $\Delta\beta$) and large enough intra-array channel spacing (to keep coupling constants small). However, in reality things are not as simple as they may seem because a number of restrictions on sample design such as maximum sample length, a single-mode condition for the waveguides etc. have to be also taken into account.

The design of the samples for the hybrid surface soliton experiments was based on the AlGaAs multilayer structure described earlier in Chapter 3. As a reminder, it consists of a 1.5µm thick $Al_{0.18}Ga_{0.82}As$ core layer sandwiched between $Al_{0.24}Ga_{0.76}As$ upper and lower cladding layers with thicknesses of 1.5µm and 4µm, respectively. For this composition the calculated effective refractive index contrast δ was found to be within the range $(0-6)\cdot10^{-3}$ depending on the etch depth of the upper cladding (see Figure 3.4). To facilitate further discussion, the key parameters of the sample geometry given in Figure 6.1(a) are reproduced here as Figure 7.3.
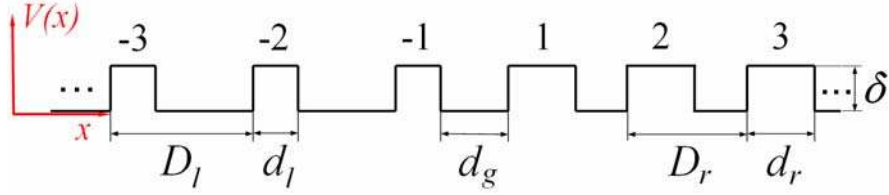
Figure 7.3: Schematic of a 1D array hetero-junction.

First the restriction on the coupling constant has to be determined. To allow for the evolution of the input beam into a soliton during propagation and to discriminate it from the discrete diffraction pattern, a sample with a length of several (minimum 3 - 4) discrete coupling lengths is usually required for the experiment. Because of fabrication limitations, the maximum length of the samples that could be fabricated was set at 1.6cm. This implies that the discrete coupling length has to be not larger than 4-5mm which, in turn, sets the minimum limit of 300 - 400m^{-1} on the coupling constants C_ℓ and C_r. Also, in order to keep the waveguides of the two arrays single-mode, the width of their ridges should not exceed ~6μm. The lower limit of approximately 2μm on the ridge width was set based on the consideration that for the narrower ridges the transverse profile of a waveguide mode deviates significantly from Gaussian profile of the input beam. Thus, for ridge width less than 2μm, an undesirable decrease of power coupling efficiency into the sample would occur.

To satisfy all the requirements just mentioned, the following parameters of the sample design were chosen: $D_\ell = D_r = (9-10)\mu m$, $d_\ell = (2-3)\mu m$ and $d_r = (4-5)\mu m$. The range of appropriate δ can be found from the condition imposed by Equation 7.4. The results of the corresponding calculations for the parameters $D_\ell = D_r = 10\mu m$, $d_\ell = 3\mu m$ and $d_r = 5\mu m$ are plotted in Figure 7.4. Here the coupling constants of the two arrays are plotted separately as a function of refractive index contrast δ (green and blue curves) and their doubled sum which

corresponds to the right side of Equation 7.4 is shown by a red curve. The black curve in this figure represents the mismatch $\Delta\beta$ in the propagation constants of the individual waveguides. It is not difficult to see that the inequality given by Equation 7.4 is satisfied in the region to the right of the intersection of the two latter curves (i.e. for $\delta > 2.2\cdot10^{-3}$). The maximum suitable value of $\delta \approx 3.2\cdot10^{-3}$ is given by the point where the coupling constant of one of the arrays falls below the 300m^{-1} limit, imposed earlier. Hence, the range of appropriate values of the effective refractive index contrast is indicated by a shaded region in Figure 7.4. Based on this data and Figure 3.4, the etch depth w, an important fabrication parameter, was found to lie within the range $(1.1-1.3)\mu m$.
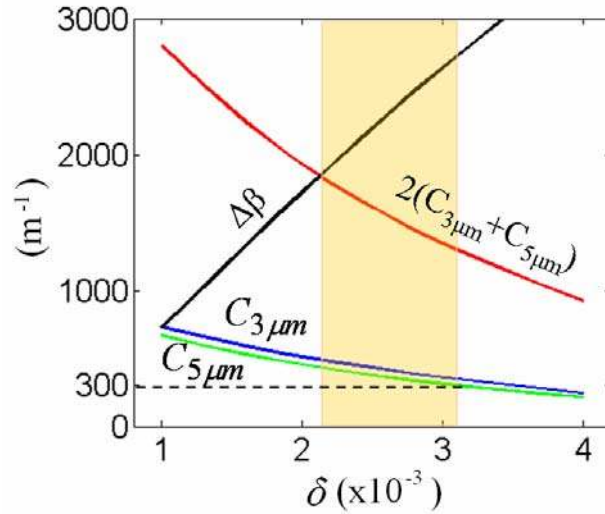
Figure 7.4: Coupling constant versus refractive index contrast for an array with $3\mu m$ (blue curve) and $5\mu m$ (green curve) wide channels. The red curve is the doubled sum of these two curves, and the propagation constant mismatch $\Delta\beta$ as a function of δ is shown by the black curve.

Taking into account all the design considerations discussed above, thirteen different AlGaAs array hetero-junctions were fabricated. Their parameters measured with a scanning electron microscope are shown in Table 3. The different values for the inter-array spacing d_g for the hetero-junctions were chosen to facilitate the observation of linear interface modes (see Chapter 6) and also to prevent their existence in the search for interface solitons with power thresholds. The length of the samples was 1.35cm, and the exact value of etch depth (height of the waveguide ridges) was measured to be 1.1µm. It was expected that within this matrix of samples, at least one would be ideal for observing discrete interface solitons of the hetero-structure.

Table 3: Parameters of the fabricated AlGaAs samples.

D_ℓ (μm)	D_r (μm)	d_ℓ (μm)	d_r (μm)	d_g (μm)
10	10	2.4	5.4	2.2
		2.4	5.4	4.2
		3.4	5.4	2.4
		2.4	4.4	3.4
		2.4	4.4	5.2
9	10	5.4	2.4	2.4
		2.4	5.4	2.4
9	9	2.4	5.4	2.2
		2.4	5.4	4.2
		2.4	4.4	2.2
		2.4	4.4	4.2
8	9	5.4	2.6	2.2
		2.4	5.6	3.0

7.3. Experimental results and discussion

For the experiments on the observation of in-phase/in-phase hybrid surface solitons, two samples with the parameters given by the 4th and 5th lines of Table 3 were chosen. Because many of the properties (i.e. the dispersion curves and power thresholds) of the hybrid solitons and discrete surface solitons, discussed in Chapter 5, are similar, again a TM polarized input beam was chosen for the experiments. The lower input power requirements for observation of hybrid surface soliton in TM versus TE polarization (regarding discrete surface solitons see Figure 5.10) helped to reduce detrimental effects of nonlinear absorption. In our samples, two different in-phase/in-phase solitons are predicted: one with its peak in the first channel of the left-side array and another one peaked in the boundary channel of the right-side array. Both were observed in the AlGaAs hetero-junction samples.

The evolution of optical wave propagating in a hetero-junction sample involves many factors such as the coupling strengths in the individual arrays C_ℓ and C_r, the inter-array coupling constants $C_{\ell \to r}$ and $C_{r \to \ell}$ (between the two interface channels) and the mismatch $\Delta\beta$ in the propagation constants of isolated channels of the two arrays. In the samples chosen for the experiments, these parameters were: $C_\ell = 440m^{-1}$, $C_r = 360m^{-1}$; $C_{\ell \to r} \approx (310m^{-1}$ and $540m^{-1})$ and $C_{r \to \ell} \approx (940m^{-1}$ and $1420m^{-1})$ for the two array separations $d_g = 5.2\mu m$ and $3.4\mu m$, respectively. Finally, $\Delta\beta \approx 2600m^{-1}$.

In order to understand the nature of the interface solitons, linear beam propagation dynamics for single channel excitation of the two boundary channels was investigated. Linear propagation in the hetero-structures with similar parameters was discussed earlier in Chapter 6

and the results of BPM simulations were presented in Figure 6.2. The experimentally recorded

output intensities for the two inter-array separations are shown in Figure 7.5. When the boundary

channel of the left-side array is excited, some fraction of energy clearly couples to the right-side

array boundary channel even for the larger inter-array spacing $5.2\mu m$ (see Figures 7.5(c)).

Furthermore, as expected, the smaller the gap between arrays, the stronger the power transfer, as

can be seen from Figure 7.5(d). This is in sharp contrast to transfer from the right to the left

when the boundary channel of the right-side array is excited, see Figures 7.5(a) and (b). In this

case, there is almost no energy coupled across the gap in either case.
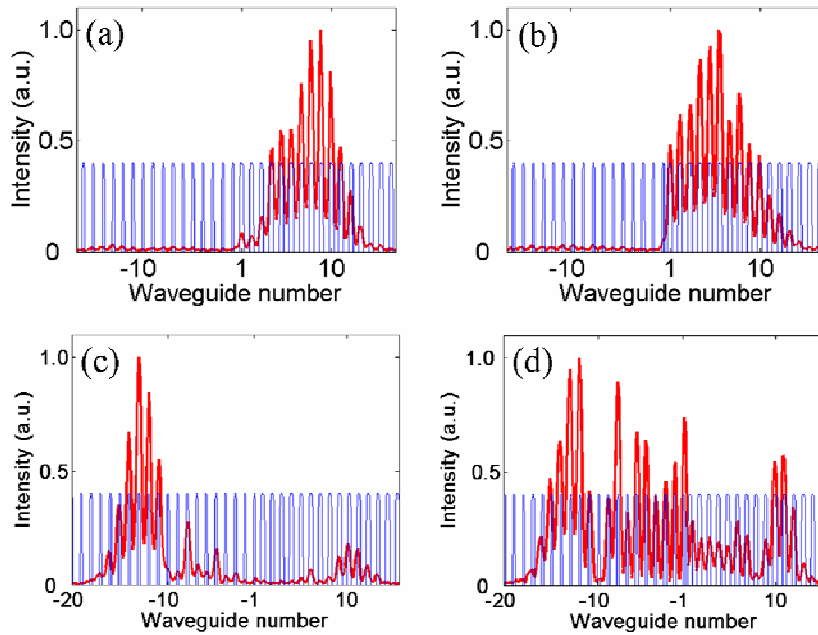
Figure 7.5: Discrete diffraction patterns recorded at the sample's output facet for the inter-array

spacing $d_g = 5.2\mu m$ (a), (c) and $3.4\mu m$ (b), (d). The boundary channel of the right-side (a), (b)

and the left-side (c), (d) arrays was excited.

The differences in the discrete diffraction patterns between the two cases suggest that the nonlinear propagation (i.e. the soliton formation at the interface) will also occur differently for the two sides of the interface. This hypothesis has been confirmed by the results of the nonlinear experiments.

Consider first the surface soliton that peaks in the first channel of the right-side array because its nature is easier to explain. In the experiment, the boundary ($n = 1$) waveguide of the right-side array was excited, and, as the power of the input beam was increased, the intensity at the sample's end facet was recorded.
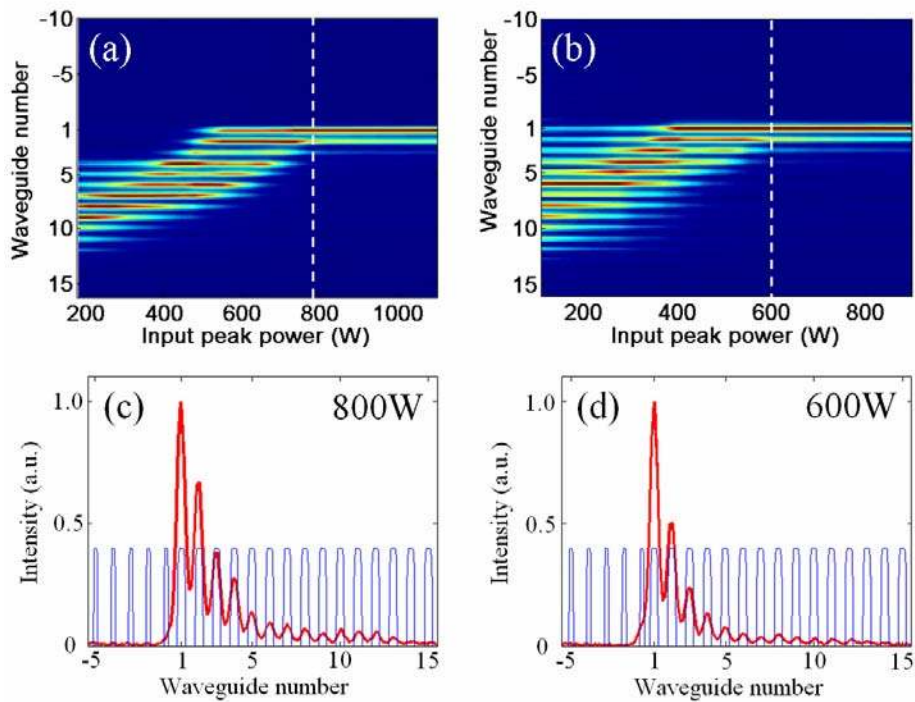
Figure 7.6: Intensity patterns observed at the sample's end facet as a function of input power for d_g = (a) $5.2\mu m$ and (b) $3.4\mu m$ when the input beam was injected into the $n = 1$ channel. (c) and (d) are the detailed recorded intensities at peak input power levels indicated by the vertical dashed lines on the respective plots.

The results of the experiments are shown in Figures 7.6(a) and (b) for the inter-array spacing $5.2\mu m$ and $3.4\mu m$, respectively. As before in similar plots in Chapter 5, the intensity pattern at each power level was normalized to unity before plotting. Therefore, the red-brown color is only an indication of the intensity maxima at particular power levels and not the measure of the real intensity.

In both samples, as the incident power was increased, a collapse of the discrete diffraction pattern toward the excitation channel occurred. The threshold input power for the formation of a strongly localized soliton for each case is identified by dashed lines in Figures 7.6(a) and (b) which correspond to the points where most of the power is confined in the initially excited boundary channel. The threshold peak power of 800W was found for hetero-structure with $d_g = 5.2\mu m$ while a 600W was measured for the sample with $d_g = 3.4\mu m$. The corresponding intensity distributions of hybrid surface solitons are shown in Figures 7.6(c) and (d). It is clear that they are associated with a discrete surface soliton at the array-continuum interface shown earlier in Figure 5.17(a) because almost no power is carried in the first channel of the left-side array. Note that the two outer boundaries of the composite structure correspond to interfaces between the corresponding arrays and a 1D slab waveguide. These boundaries were used to evaluate the threshold powers for discrete surface solitons traveling along the interface between the slab waveguide and the appropriate array. It turned out that the power threshold for the composite array with $d_g = 5.2\mu m$ (~800W) was ~1.5 times lower than that for the array-continuum boundary (1200W). Furthermore, for $d_g = 3.4\mu m$, the measured array-array discrete soliton threshold power (~600W) was only half of that for the array-continuum boundary.

Similar experiments have been conducted to observe hybrid solitons peaked in the boundary channel on the left from the interface. This time, the input beam was injected into the

first boundary channel of the left-side array ($n = -1$). Figures 7.7(a) and (b) show the distribution of the output intensity versus peak input power for the inter-array spacing $5.2 \mu m$ and $3.4 \mu m$, respectively. Again, as in the previous case, the collapse toward the excitation channel was observed as the incident power was increased. The threshold powers were found to be 2400W ($d_g = 5.2 \mu m$) and 1700W ($d_g = 3.4 \mu m$), and corresponding soliton intensities at the output facet are presented in Figures 7.7(c) and (d).
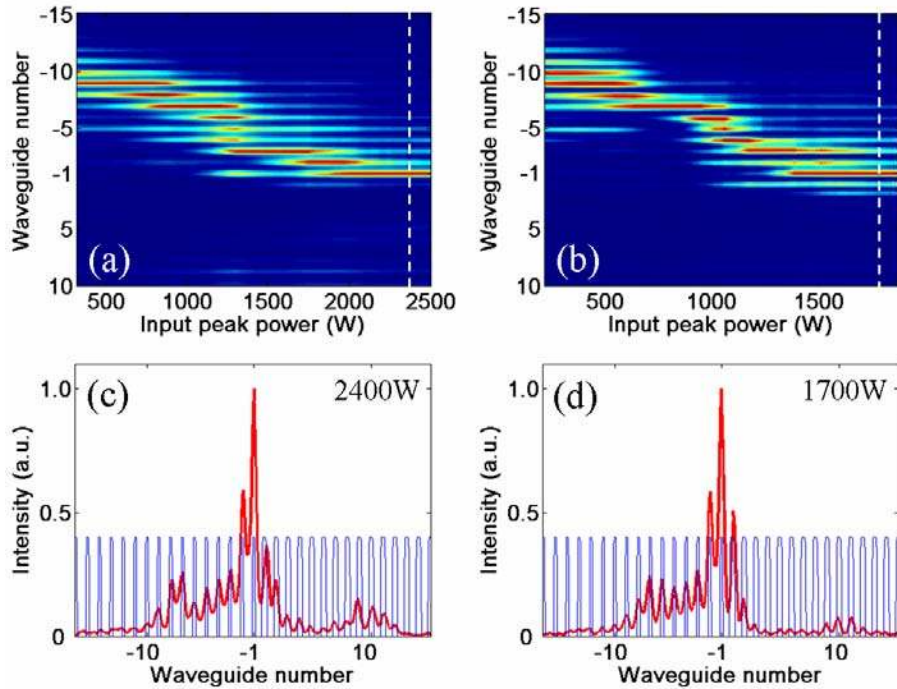
Figure 7.7: Intensity patterns observed at the samples' end facets as a function of input power for d_g = (a) $5.2 \mu m$ and (b) $3.4 \mu m$ when an input beam was injected into the $n = -1$ channel. (c) and (d) are intensities at peak power levels indicated by vertical dashed lines in the respective plots.

The discrete surface soliton threshold power was measured at the 1D array-continuum boundary, and a value of 1500W was found which is lower than the array-array interface values (2400W

and 1700W). This is in sharp contrast to the previous case of a hybrid soliton peaked in the $n = 1$ channel where the threshold power was lower than that for the array-continuum boundary. Unlike the case of a soliton peaked in the $n = 1$ channel, there are nonzero fields associated with these solitons in the channels on the other side of the interface. This identifies the observed discrete soliton as belonging to the interface between the two arrays.

It can be qualitatively shown that only one of the two soliton types discussed above can be a true soliton of the hetero-structure, i.e. the one with its field components in the two arrays propagating locked together. Such a soliton has a common propagation constant for soliton fields on both sides of the boundary. Therefore, taking into account the location of the nonlinear eigenvalue of an in-phase/in-phase hybrid soliton in the band diagram (see Figure 7.8), this condition can be written as

$$(\beta_\ell + 2C_\ell) + \Delta k_{z,\ell}^{NL} = (\beta_r + 2C_r) + \Delta k_{z,r}^{NL}, \tag{7.5}$$

where $(\beta_\ell + 2C_\ell)$ and $(\beta_r + 2C_r)$ are the propagation wavevectors which correspond to the top of the first bands of the individual arrays, and $\Delta k_{z,\ell}^{NL}$ and $\Delta k_{z,r}^{NL}$ are the nonlinear contributions to the wavevector.
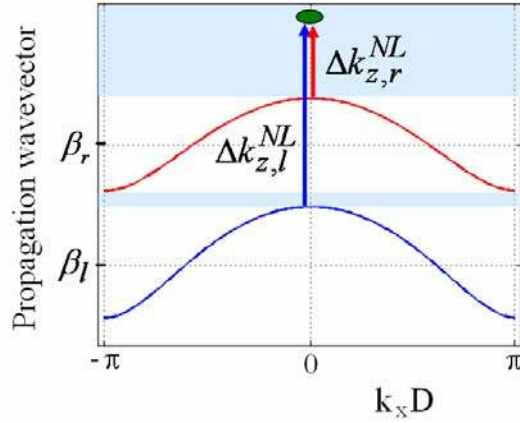
Figure 7.8: The first band of the right-side array $k_{z,r}(k_x)$ (upper curve) and of the left-side array $k_{z,\ell}(k_x)$ (lower curve), and the nonlinear changes to the wavevector $\Delta k_{z,\ell}^{NL}$ and $\Delta k_{z,r}^{NL}$ required for the formation of a hybrid soliton.

Rearranging Equation 7.5 gives the following relation

$$\Delta k_{z,\ell}^{NL} - \Delta k_{z,r}^{NL} = \Delta \beta + 2(C_r - C_\ell). \tag{7.6}$$

For the samples studied, the right side of Equation 7.6 is positive and approximately equal to $2440m^{-1}$. This implies that $\Delta k_{z,\ell}^{NL} > \Delta k_{z,r}^{NL}$. For the self-focusing Kerr nonlinearity, a positive nonlinear refractive index change results in a positive nonlinear contribution to the propagation wavevector in either array. This implies that the soliton intensity in the left-side array boundary channel must be larger than that in the right-side array boundary channel. This can only be true for a composite soliton peaked in the boundary channel of the left-side array (n = -1). Furthermore, using Equation 7.6, an approximate threshold power for this soliton can be estimated. The minimum of the optical power required to satisfy Equation 7.6 corresponds to the situation when

$$\Delta k_{z,\ell}^{NL} = \Delta\beta + 2(C_r - C_\ell)$$
$$\Delta k_{z,r}^{NL} = 0.$$

<div align="right">(7.7)</div>

The dependence of $\Delta k_{z,\ell}^{NL}$ on the optical peak power can be found based on the expression for the nonlinearly induced refractive index change of AlGaAs material as given by

$$\Delta n^{NL} = \hat{n}_2 \frac{P}{A_{eff}} \approx 10^{-6} \cdot P \ (Watts),$$

<div align="right">(7.8)</div>

where A_{eff} is the effective area of the TM fundamental mode of an isolated waveguide. To find the relation between $\Delta k_{z,\ell}^{NL}$ and Δn^{NL} for ridge waveguide geometry, first the refractive index of the core layer under the ridge is increased by the value of Δn^{NL}, then the corresponding 1D effective refractive index potential is calculated using the effective index method, and finally the nonlinear mode field is found using a 1D finite difference mode-solver. Using this approach, the following relation that connects $\Delta k_{z,\ell}^{NL}$ and Δn^{NL} was found

$$\Delta k_{z,\ell}^{NL} \ (m^{-1}) \approx 0.5 k_0 \cdot \Delta n^{NL} \approx 2 \cdot P \ (Watts).$$

<div align="right">(7.9)</div>

Using Equations 7.7 and 7.9, the minimum peak power required for hybrid soliton formation was estimated to be approximately 1200W. This number is close to the experimental values of 2400W and 1700W which are higher because of the pulsed nature of the experiment and the fact that channel fields in both arrays are excited. Note that it is the excitation of both arrays that results in power thresholds for the interface solitons being higher than that for the respective array-continuum boundary.

For the excitation of the $n = 1$ channel, which has led to discrete surface solitons peaked in the excitation channel, the condition $\Delta k_{z,\ell}^{NL} > \Delta k_{z,r}^{NL}$ cannot be satisfied. Also note the lack of

excitation of channels in the left-side array in Figure 7.6 for this case. Therefore, these solitons are associated with a 1D array-continuum boundary. The lower values of power thresholds measured for these solitons when compared to those measured for the simple 1D array-continuum interface occur because the soliton field extending into the left-side array experiences an average effective refractive index which is higher than that of the "bare" slab waveguide due to the presence of the ridges of the left-side array. The threshold soliton power is proportional to the effective index difference across the boundary.

Similar to the case of the array-continuum interface discussed in Chapter 5, discrete spatial solitons with decreasing power thresholds were observed for channels progressively deeper into a given array of the composite structure, see Figure 7.9.
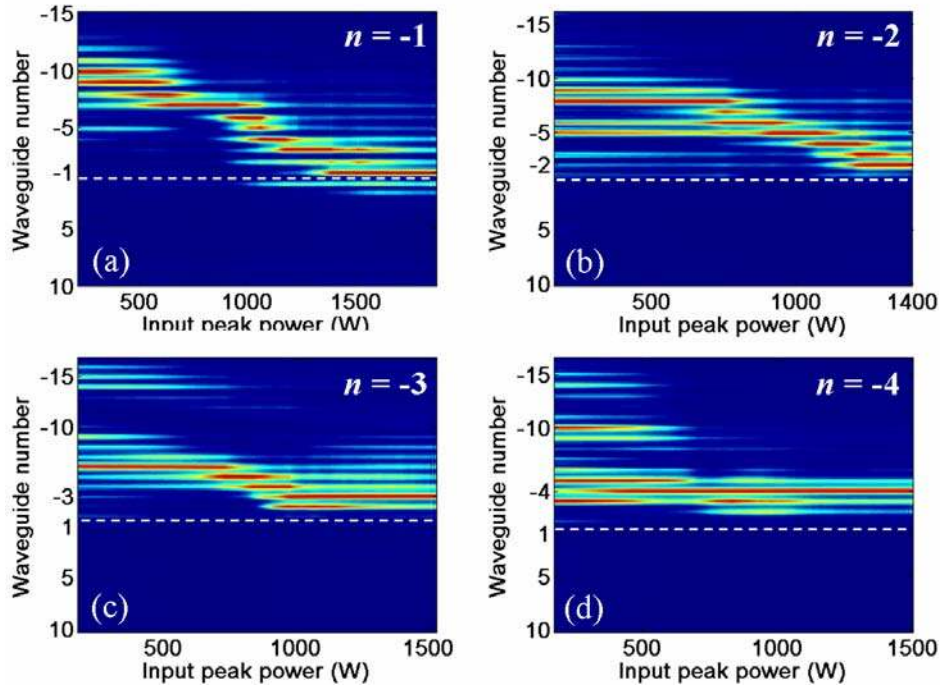
Figure 7.9: The evolution of the output intensity distribution across the array with increasing input power into the channels (a) $n = -1$, (b) $n = -2$, (c) $n = -3$, (d) $n = -4$ for the array separation $d_g = 3.4 \mu m$. Interface location is shown by dashed lines.

Power thresholds were measured for solitons with fields peaked in channels of the left-side array (n = -2, -3, -4…). They were found to be similar to those of the array-continuum case because even for the second (n = -2) channel, almost no power is coupled to the right-side array.

In contrast to this, the experimental study of solitons peaked in channels of the right-side array (n = 2, 3, 4…) yielded unexpected and interesting phenomena. The results of the experiments with the excitation of the second (n = 2) guide of the right-side array are shown in Figures 7.10(a) and (b) for the two values of the gap $d_g = 5.2\mu m$ and $3.4\mu m$, respectively.
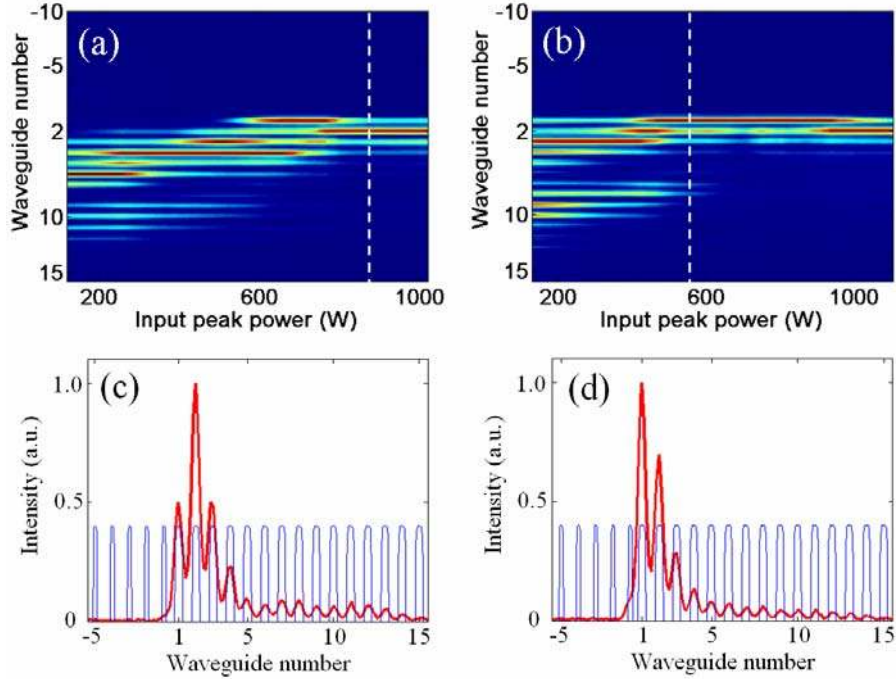
Figure 7.10: Output intensity versus peak input power for d_g = (a) $5.2\mu m$ and (b) $3.4\mu m$ when the input beam was injected into the n = 2 channel. (c) and (d) are the recorded intensities at power levels indicated by vertical dashed lines on the respective plots.

As expected in both cases, the discrete diffraction pattern collapses into the initially excited n = 2 waveguide at high powers. However, in a limited input power range before collapse

into the excitation channel to form a discrete soliton there, localization occurs in the boundary channel ($n = 1$). The smaller the gap between arrays, the larger the power range over which this localization occurs, see Figure 7.10(a) and (b)). This localization persists over a factor of two in input power for $d_g = 3.4\mu m$, suggesting that this could be a stable soliton.

In order to confirm or disprove the speculation that it is a stable soliton that was observed in the channel $n = 1$, the simulation of the nonlinear propagation with the second ($n = 2$) channel excited over a sufficiently long propagation distance (4cm, or ~10 coupling discrete diffraction lengths) was performed. The simulation results with the use of pulsed excitation are presented in Figure 7.11(a). While the propagation seems to be stable after the initial jump of the input beam to the boundary ($n = 1$) guide, the continuous leaking of energy from this channel into the right-side array finally causes the power to decay. However, for the cw excitation case shown in Figure 7.11(b), stable propagation with the intensity peak in the boundary channel is obtained, thus confirming the existence of a stable soliton. Note that simulations also showed that at higher input powers light beam never jumps to the boundary channel and a soliton is formed at the excited $n = 2$ waveguide site, as expected.
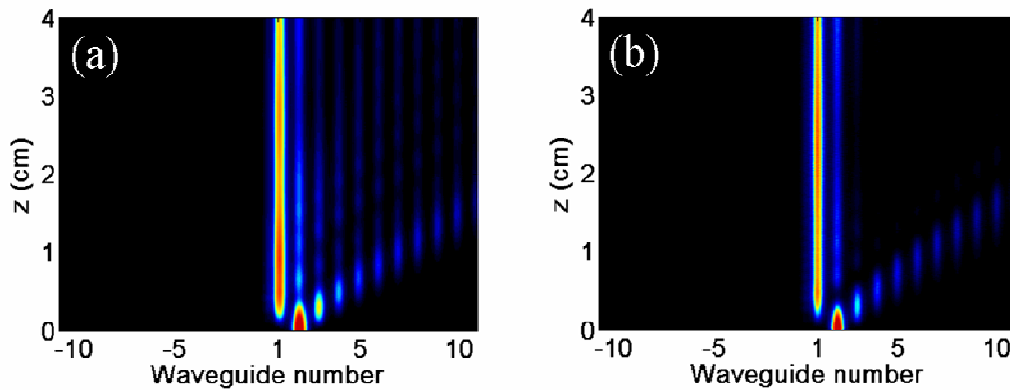
Figure 7.11: Simulated propagation for the excitation of the $n = 2$ channel with (a) pulses with 500W of peak power and (b) cw beam at 350W.

Shown in Figure 7.12 are experimental results for the excitation of the $n = 3$ and 4 channels. Clearly localization into the $n = 1$ channel also occurs for these cases, and again these solitons were found to be stable (by BPM simulation studies). For the $n = 4$ excitation, the rapid "collapse" from the $n = 1$ into the $n = 4$ channel with increased power is clearly observed. Furthermore, the power range for the formation of a soliton in the boundary channel decreases with increasing n and disappears completely deeper inside the array.
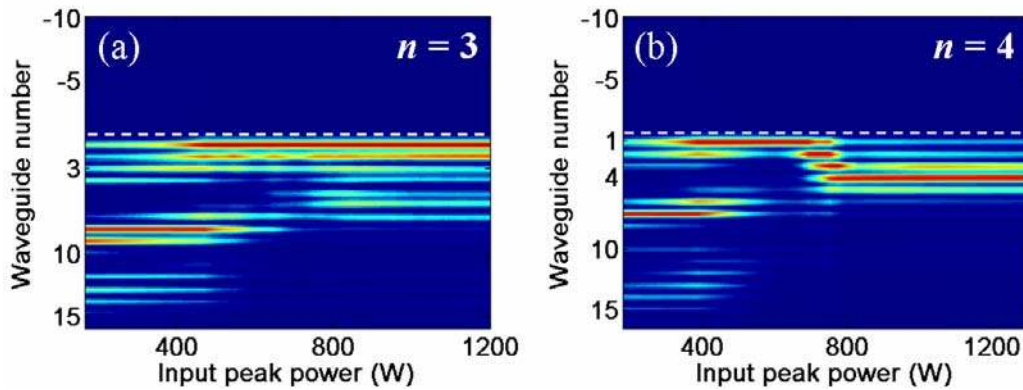
Figure 7.12: Intensity at the output facet versus peak input power for $d_g = 3.4\mu m$ when input beam was injected into (a) $n = 3$ and (b) $n = 4$ channels.

Similar experiments were performed for $d_g = 5.2\mu m$, and as shown in Figure 7.13, there is no extended power range over which localization occurs in the $n = 1$ channel at typical powers for the formation of a discrete soliton. Hence, this is clearly a surface effect which has a strong dependence on the size of the gap.
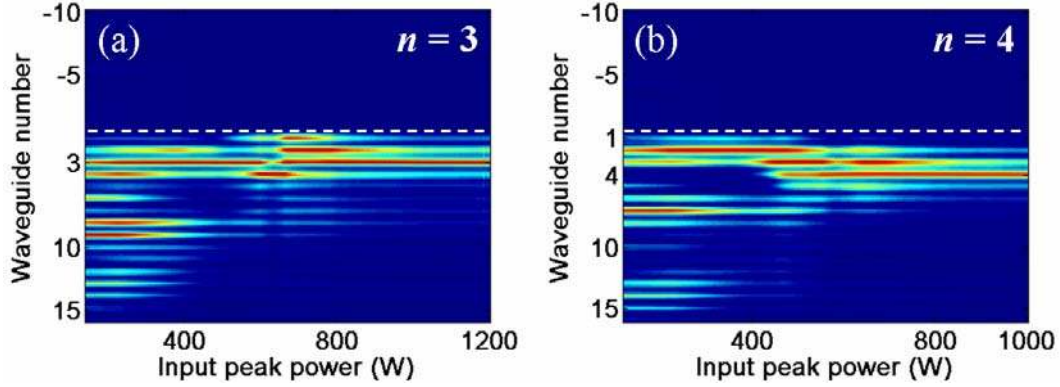
Figure 7.13: Intensity at the output facet versus peak input power for $d_g = 5.2\mu m$ when input beam was injected into (a) $n = 3$ and (b) $n = 4$ channels.

A speculative explanation for this effect will now be given for the simplest $n = 2$ excitation case. The threshold power for the $n = 1$ soliton is depressed relative to that of the surface soliton at the slab waveguide – right-side array boundary. This occurs because the effective index of the left-side array region, as sampled by light guided in the $n = 1$ channel, is increased over that of the slab waveguide due to the presence of the high index ridges. As a result, the soliton threshold power is the lowest in the $n = 1$ channel, as observed. Thus it is more power efficient for a soliton to form in that channel, even with excitation of channels with $n > 1$. As power is increased further, the soliton "jumps" to the excitation channel when the incident power exceeds that required to trap the soliton in the particular $n > 1$ excitation channel.

As explained in the theoretical discussion, no staggered field hybrid surface solitons exist in an AlGaAs hetero-structure at 1550nm because they require the opposite sign of the nonlinearity. This was checked experimentally for the sample which exhibits the staggered/staggered linear interface mode discussed in Chapter 6 (sample's parameters were $d_\ell = 2.4\mu m$, $d_r = 5.4\mu m$ and $d_g = 2.4\mu m$). This linear mode was excited as described in

107

Chapter 6, and the input peak power was ramped up. As shown in Figure 7.14, there was no shape change in the output pattern with increased power. If indeed a soliton had been generated, increased localization of the intensity pattern was expected. Clearly, no soliton was generated in this case.
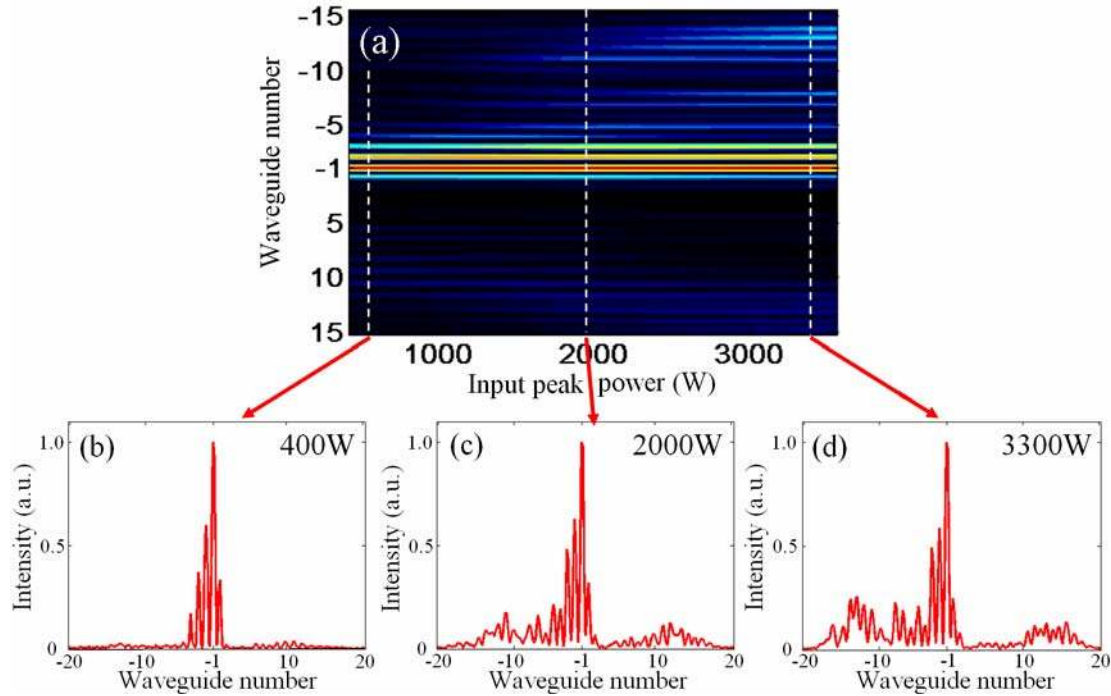
Figure 7.14: (a) Intensity at the output facet versus peak input power for the $2.4\mu m$ gap when a wide input beam was injected with a π phase shift between adjacent channels. (b) - (d) Intensity distributions measured at three separate powers indicated by dashed lines in (a).

In summary, the first results on discrete spatial solitons guided by the boundary between two dissimilar periodic arrays have been presented. Two solitons were predicted and identified experimentally, and their properties were in excellent agreement with theoretical predictions. Initially unexpected localization into the boundary channel was observed for certain excitation conditions.

CHAPTER EIGHT: CONCLUSIONS

8.1. Summary

In this dissertation both experimental and theoretical investigation of linear and nonlinear optical properties of the interface between one-dimensional Kerr-nonlinear waveguide lattice and a continuous slab waveguide, as well as properties of a boundary between two dissimilar waveguide arrays, have been presented. Most of the experiments were conducted for the first time verifying various theoretical predictions.

The major part of the dissertation was devoted to the first experimental observation of discrete surface solitons. These nonlinear surface waves have been predicted to exist at and near the boundary of a semi-infinite nonlinear waveguide lattice. It has been shown that in the linear regime such an interface cannot support surface waves. Therefore, discrete surface solitons are the direct outcome of nonlinearity. The formation process of highly confined discrete surface solitons with an increased power of an optical beam injected into single channels close to the boundary has been investigated in detail, both theoretically and experimentally. In the experiments, a collapse of the output intensity pattern associated with discrete diffraction into the array's boundary channel has been observed thus proving the existence of discrete surface solitons. The rapid nature of the collapse has confirmed the key property of these nonlinear waves, namely the existence of a power threshold predicted by theory.

The power thresholds of discrete surface solitons localized in different channels near the array's boundary have been measured experimentally for several array geometries having different values of coupling constant between adjacent waveguides. The results of the experiments were in excellent agreement with the theoretical analysis which predicts that the power threshold decreases as the localization site of a soliton moves inside the array. Also, a qualitatively good correlation of the measured threshold values with the inter-channel coupling strength has been found. A minimum in the incident threshold power required for the formation of an essentially single channel soliton was found by varying the channel width and coincided with a minimum in the inter-channel coupling strength.

Interfaces between two dissimilar waveguide arrays (waveguide array hetero-junctions) were also predicted to support discrete nonlinear surface waves called hybrid surface solitons. It has been shown that the detuning of the propagation constants of the waveguides constituting the two semi-infinite arrays shifts the dispersion relation of one array with respect to that of the other one. This can result, under the appropriate array geometries, in the formation of additional band gaps between the allowed bands of the individual arrays. Depending on the position of their nonlinear eigenvalues within the band diagram of the composite hetero-structure, different symmetry hybrid surface solitons have been theoretically predicted. For the Kerr-type nonlinearity, three different soliton solutions with different symmetry of their electric fields have been found, two of them for the self-focusing nonlinearity and the third one for the defocusing case. For the experiments, the AlGaAs hetero-junction samples, where the two arrays were made different by varying the width of their waveguides, have been designed and fabricated. In these samples, two different in-phase/in-phase solitons peaked on either side of the interface have been demonstrated experimentally. A theoretical study has revealed that only one of these two solitons

110

is a true hybrid soliton of a hetero-structure while the other one is associated with a 1D array-continuum boundary with very little power propagating in the array on the opposite side of the interface. Also, a decrease in the inter-array separation with all other parameters of the composite structure kept constant has brought some interesting results. More specifically, it has been observed that within the limited input power range, when the second waveguide of one of the arrays (with higher propagation wavevectors of its first band) is excited, the input beam jumps to the boundary channel forming a soliton there. Only when incident power was increased above a certain level, the soliton formation occurred in the excitation channel, as expected. This behavior has been found only in the samples with a sufficiently small inter-array spacing, and experimental observations have been confirmed by the results of the corresponding BPM simulations.

Decreasing the inter-array spacing has been found to lead also to the possibility of stable linear (low power) modes propagating along the hetero-interface in the linear regime. These modes located in the *k*-space in the band gaps of the composite structure were studied both theoretically and experimentally for the first time. Three different symmetry types of linear modes were numerically found with their propagation eigenvalues in different band gaps. One of them, namely the staggered/staggered interface mode, has been successfully observed in the experiments, and its intensity profile was found to be in excellent agreement with the calculated mode intensity.

8.2. Implications and future work

As was mentioned earlier in Chapter 6, the recent advances in fabrication technologies have allowed manufacturing of periodic structures with higher dimensionality such as photonic

crystals. Photonic crystals, the artificial materials with a periodic modulation of their dielectric constant, display many properties analogous to semiconductors and waveguide arrays, including allowed bands and band gaps in their band structure. A two-dimensional waveguide lattice is an example of a photonic crystal. Recently, it has been predicted that besides the 1D array – slab waveguide interface, discrete surface solitons can also exist at the boundaries of such 2D lattices. More specifically, it has been shown that discrete nonlinear surface waves are possible in the corner and at the edge of the semi-infinite square lattice of Kerr-nonlinear waveguides [54]. Subsequently, these two-dimensional surface solitons have been successfully observed at the boundaries (edges and corners) of a finite optically induced photonic lattice in photorefractive nonlinear medium [100] as well as at the edge and in the corner of a Kerr-nonlinear laser-written waveguide array in fused silica [101]. These results, both experimental and theoretical, suggest that discrete hybrid solitons should also exist at the hetero-interfaces of two (or more) dissimilar 2D waveguide lattices (and photonic crystals in general).

On the other hand, similar to a 1D interface case in the linear regime, it has been theoretically shown that simple 2D photonic crystal hetero-structures such as that composed of two semi-infinite square lattices of air cylinders embedded in a homogeneous dielectric background, and the other one made of two dissimilar lattices of dielectric cylinders in air (i.e. 2D waveguide array hetero-junction), can support linear guided modes if the separation between the two lattices is small enough [102]. Therefore, it would be of great interest to investigate new linear and nonlinear phenomena in photonic crystal hetero-structures which no doubt should be more versatile than their one-dimensional counterparts owing to the bigger diversity of possible 2D structure geometries.

Regarding 1D waveguide array hetero-junctions, the study presented in this dissertation by no means exhausts interesting linear and nonlinear phenomena that can be observed in such systems. For example, the transmission and reflection properties of array hetero-junction have been studied theoretically and it was proposed that this structure can be used as a spatial filter where certain spatial frequency components are allowed to cross the interface while other are reflected [103]. This happens because the z-component of the propagation wavevector has to be conserved when light wave crosses the interface between the two lattices. In Reference 103, the general case of two 1D semi-infinite lattices with a transition/interface region composed of several waveguides is considered. Using the coupling mode theory, the power transmission and reflection coefficients of AlGaAs hetero-interface, described in this dissertation, can be readily derived. These coefficients depend on such parameters as coupling constants C_ℓ, C_r, $C_{\ell \to r}$, and $C_{r \to \ell}$, the propagation constants' mismatch $\Delta\beta$, and on the wavevector of the light wave in the input array. Therefore, it would be of interest to study experimentally how the power transmission of a real beam (with a finite spatial extent and hence with a definite spectrum of spatial frequencies) across the hetero-interface depends on the inter-array separation d_g and the mismatch $\Delta\beta$.

On the other hand, some of the nonlinear soliton phenomena associated with the 1D array-continuum interface such as vector discrete surface solitons are yet to be observed. These self-trapped states are formed through the coexistence of two orthogonally polarized fields. Discrete vector solitons were first predicted and successfully observed in the bulk of one-dimensional Kerr-nonlinear waveguide arrays in 2003 [104]. Later in 2005, vector discrete nonlinear surface waves were predicted to exist at the boundary of such waveguide lattices [105]. In particular, the possibility of linearly polarized vector surface waves localized in the first

113

waveguide of a semi-infinite array and comprised of in-phase TE and TM components propagating locked together has been demonstrated. Moreover, it has been found that, when only a single waveguide is excited with the appropriate power levels for the TE and TM components, these vector surface waves can propagate in a stable fashion even when the relative phase difference between the two components is as high as $\pm 20^0$.

LIST OF REFERENCES

[1]   J. Frenkel and T. Kontorova, "On the theory of plastic deformation and twinning," J. Phys. **1**, 137 (1939).

[2]   J. E. Fermi, J. R. Pasta, and S. M. Ulam, "Studies of nonlinear problems - Report No. LA1940," (Los Alamos National Laboratory, Los Alamos, 1955).

[3]   N. W. Ashcroft and N. D. Mermin, *Solid State Physics* (Saunders College, Philadelphia, 1976).

[4]   M. Toda, "Vibration of a chain with nonlinear interaction," J. Phys. Soc. Jap. **22**, 431 (1967).

[5]   M. Toda, "Mechanics and statistical mechanics of nonlinear chains," J. Phys. Soc. Jap. S **26**, 235 (1969).

[6]   S. Aubry, "Unified approach to interpretation of displacive and order-disorder systems .2. Displacive systems," J. Chem. Phys. **64**, 3392 (1976).

[7]   J. A. Krumhansl and J. R. Schrieffer, "Dynamics and statistical-mechanics of a one-dimensional model Hamiltonian for structural phase-transitions," Phys. Rev. B **11**, 3535 (1975).

[8]   A. S. Davydov, "Theory of contraction of proteins under their excitation," J. Theor. Biol. **38**, 559 (1973).

[9]   A. S. Davydov, *Biology and Quantum Mechanics* (Pergamon, Oxford, 1982).

[10]   M. Peyrard and J. Farago, "Nonlinear localization in thermalized lattices: application to DNA," Physica A **288**, 199 (2000).

[11]   M. A. Collins, "Solitons in chemical physics," Adv. Chem. Phys. **53**, 225 (1983).

[12]   M. A. Collins and D. P. Craig, "A model of localization, soliton propagation, and self-trapping in an electrically excited atomic lattice," Chem. Phys. **75**, 191 (1983).

[13]   A. S. Davydov and N. I. Kislukha, "Solitary excitons in one-dimensional molecular chains," Physica Status Solidi B **59**, 465 (1973).

[14]   F. K. Abdullaev, B. B. Baizakov, S. A. Darmanyan, V. V. Konotop, and M. Salerno, "Nonlinear excitations in arrays of Bose-Einstein condensates," Phys. Rev. A **64,** 043606 (2001).

[15]   A. Trombettoni and A. Smerzi, "Discrete Solitons and Breathers with Dilute Bose-Einstein Condensates," Phys. Rev. Lett. **86**, 2353 (2001).

[16]   P. St. J. Russell, "Photonic Crystal Fibers," Science **299**, 358 (2003).

[17]   D. N. Christodoulides, F. Lederer, and Y. Silberberg, "Discretizing light behavior in linear and nonlinear waveguide lattices," Nature **424**, 817 (2003).

[18]   D. Mandelik, H. S. Eisenberg, Y. Silberberg, R. Morandotti, and J. S. Aitchison, "Band-Gap Structure of Waveguide Arrays and Excitation of Floquet-Bloch Solitons," Phys. Rev. Lett. **90**, 053902 (2003).

[19]   H. F. Taylor and A. Yariv, "Guided Wave Optics," Proc. IEEE **62**, 1044 (1974).

[20]   A. Yariv, "Coupled-mode theory for guided wave optics," IEEE J. Quantum Electron. **9**, 919 (1973).

[21]   A. L. Jones, "Coupling of optical fibers and scattering in fibers," J. Opt. Soc. Am. **55**, 261 (1965).

[22]   S. Somekh, E. Garmire, A. Yariv, H. L. Garvin, and R. G. Hunsperger, "Channel optical waveguide directional couplers," Appl. Phys. Lett. **22**, 46 (1973).

[23]   D. N. Christodoulides and R. I. Joseph, "Discrete self-focusing in nonlinear arrays of coupled waveguides," Opt. Lett. **13**, 794 (1988).

[24]   T. Peschel, U. Peschel, and F. Lederer, "Discrete bright solitary waves in quadratically nonlinear media," Phys. Rev. E **57**, 1127 (1998).

[25]   N. K. Efremidis, S. Sears, D. N. Christodoulides, J. W. Fleischer, and M. Segev, "Discrete solitons in photorefractive optically induced photonic lattices," Phys. Rev. E **66**, 046602 (2002).

[26]   N. K. Efremidis and D. N. Christodoulides, "Discrete Ginzburg-Landau solitons," Phys. Rev. E **67** (2003).

[27] E. A. Ultanir, G. I. Stegeman, and D. N. Christodoulides, "Dissipative photonic lattice solitons," Opt. Lett. **29**, 845 (2004).

[28] H. S. Eisenberg, Y. Silberberg, R. Morandotti, A. R. Boyd, and J. S. Aitchison, "Discrete Spatial Optical Solitons in Waveguide Arrays," Phys. Rev. Lett. **81**, 3383 (1998).

[29] J. W. Fleischer, M. Segev, N. K. Efremidis, and D. N. Christodoulides, "Observation of two-dimensional discrete solitons in optically induced nonlinear photonic lattices," Nature **422**, 147 (2003).

[30] R. Iwanow, R. Schiek, G. I. Stegeman, T. Pertsch, F. Lederer, Y.Min, and W. Sohler, "Observation of discrete quadratic solitons," Phys. Rev. Lett. **93**, 113902 (2004).

[31] A. Fratalocchi, G. Assanto, K. A. Brzdakiewicz, and M. A. Karpierz, "Discrete propagation and spatial solitons in nematic liquid crystals," Opt. Lett. **29**, 1530 (2004).

[32] A. Zangwill, *Physics at Surfaces* (Cambridge University Press, Cambridge, New York, 1988).

[33] I. Tamm, Phys. Z. Sowjetunion **1**, 733 (1932).

[34] W. Shockley, "On the surface states associates with a periodic potential," Phys. Rev. **56**, 317 (1939).

[35] S. G. Davison and M. Steslicka, *Basic theory of surface states* (Oxford University Press, New York, 1992).

[36] A. A. Maradudin and G. I. Stegeman, "Surface acoustic waves," in *Surface Photons*, W. Kress and F. W. De Wette, eds. (Springer-Verlag, Berlin, 1991), pp. 5-35.

[37] V. M. Agranovich and D. L. Mills, *Surface Polaritons* (North-Holland, Amsterdam, 1984); W. L. Barnes, A. Dereux, and T. W. Ebbesen, "Surface plasmon subwavelength optics," Nature **424**, 824 (2003).

[38] D. Kossel, "Analogies between thin-film optics and electron-band theory of solids," J. Opt. Soc. Am. **56**, 1434 (1966).

[39] J. A. Arnaud and A. A. Saleh, "Guidance of surface waves by multilayer coatings," Appl. Opt. **13**, 2343 (1974).

[40] P. Yeh, A. Yariv, and A. Y. Cho, "Optical surface waves in periodic layered media," Appl. Phys. Lett. **32**, 104 (1978).

[41] P. Yeh, A. Yariv, and C. S. Hong, "Electromagnetic propagation in periodic stratified media. I. General theory," J. Opt. Soc. Am. **67**, 423 (1977).

[42] A. D. Boardman, P. Egan, F. Lederer, U. Langbein, and D. Mihalache, *Nonlinear Surface Electromagnetic Phenomena,* H. E. Ponath and G. I. Stegeman, eds. (North-Holland, Amsterdam, 1991), p.73.

[43] M. Miyagi and S. Nishida, Sci. Rep. Res. Inst. Tohoku Univ. Ser. B **24**, 53 (1972).

[44] W. J. Tomlinson, "Surface wave at a nonlinear interface," Opt. Lett. **5**, 323 (1980).

[45] N. N. Akhmediev, "A novel class of non-linear surface waves-asymmetric modes in symmetric layered structures," Zh. Eksp. Teor. Fiz. **83**, 545 (1982).

[46] N. N. Akhmediev, V. I. Korneev, and Y. V. Kuz'menko, "Excitaiton of nonlinear surface waves by Gaussian light beams," Sov. Phys. JETP **61**, 62 (1985).

[47] U. Langbein, F. Lederer, and H. E. Ponath, "A new type of nonlinear slab-guided waves," Opt. Commun. **46**, 167 (1983).

[48] C. T. Seaton, J. D. Valera, R. L. Shoemaker, G. I. Stegeman J. T. Chilwell, and S. D. Smith, "Calculations of nonlinear TE waves guided by thin dielectric films bounded by nonlinear media," IEEE J. Quantum Electron. **21**, 782 (1985).

[49] G. S. Garcia Quirino, J. J. Sanchez-Mondragon, and S Stepanov, "Nonlinear surface optical waves in photorefractive crystals with a diffusion mechanism of nonlinearity," Phys. Rev. A **51**, 1571 (1995).

[50] M. Cronin-Golomb, "Photorefractive surface waves," Opt. Lett. **20**, 2075 (1995).

[51] S. Suntsov, K. G. Makris, D. N. Christodoulides, G. I. Stegeman, A. Hache, R. Morandotti, H. Yang, G. Salamo, and M. Sorel, "Observation of Discrete Surface Solitons," Phys. Rev. Lett. **96**, 063901 (2006).

[52] K. G. Makris, S. Suntsov, D. N. Christodoulides, G. I. Stegeman, and A. Hache, "Discrete surface solitons," Opt. Lett. **30**, 2466 (2005).

[53] S. Suntsov, K. G. Makris, D. N. Christodoulides, G. I. Stegeman, R. Morandotti, M. Volatier, V. Aimez, R. Arès, C. E. Rüter, and D. Kip, "Optical modes at the interface between two dissimilar discrete meta-materials," Opt. Express **15**, 4663 (2007).

[54] K. G. Makris, J. Hudock, D. N. Christodoulides, G. I. Stegeman, O. Manela, and M. Segev, "Surface lattice solitons," Opt. Lett. **31**, 2774 (2006).

[55]   R. Boyd, *Nonlinear optics* (Academic Press, Boston 1992).

[56]   K. Okamoto, *Fundamentals of Optical Waveguides* (Academic Press, San Diego, 2000).

[57]   R. G. Hunsperger, *Integrated Optics: theory and technology* (Springer Verlag, Berlin, 2002).

[58]   S. M. Jensen, "The non-linear coherent coupler," IEEE J. Quan. Electron. **18**, 1580 (1982).

[59]   S. Trillo and S. Wabnitz, "Nonlinear nonreciprocity in a coherent mismatched directional coupler," Appl. Phys. Lett. **49**, 752 (1986).

[60]   A. Villeneuve, J. S. Aitchison, B. Vögele, R. Tapella, J. U. Kang, C. Trevino, and G. I. Stegeman, "Waveguide design for minimum nonlinear effective area and switching energy in AlGaAs at half the bandgap," Electron. Lett. **31**, 549 (1995).

[61]   Y. Silberberg and G. I. Stegeman, "Nonlinear coupling of modes - A new approach to all-optical guided wave devices," J. Opt. Soc. Am. A **3**, P41 (1986).

[62]   Y. Silberberg and G. I. Stegeman, "Nonlinear coupling of waveguide modes," Appl. Phys. Lett. **50**, 801 (1987).

[63]   S. Trillo, S. Wabnitz, E. M. Wright, and G. I. Stegeman, "Soliton switching in fiber nonlinear directional couplers," Opt. Lett. **13**, 672 (1988).

[64]   F. J. Fraile-Pelaez and G. Assanto, "Coupled-mode equations for nonlinear directional couplers," Appl. Opt. **29**, 2216 (1990).

[65]   S. R. Friberg, Y. Silberberg, M. K. Oliver, M. J. Andrejco, M. A. Saifi, and P. W. Smith, "Ultrafast all-optical switching in a dual-core fiber nonlinear coupler," Appl. Phys. Lett. **51**, 1135 (1987).

[66]   A. M. Weiner, Y. Silberberg, H. Fouckhardt, D. E. Leaird, M. A. Saifi, M. J. Andrejco, and P. W. Smith, "Use of femtosecond square pulses to avoid pulse breakup in all-optical switching," IEEE J. Quant. Electron. **25**, 2648 (1989).

[67]   P. LiKamWa, A. Miller, C. B. Park, J. S. Roberts, and P. N. Robson, "All-optical switching of picosecond pulses in a GaAs quantum well waveguide coupler," Appl. Phys. Lett. **57**, 1846 (1990).

[68]   J. S. Aitchison, A. Villeneuve, and G. I. Stegeman, "Nonlinear directional couplers in AlGaAs," J. Nonlin.Opt. Phys. **4**, 871 (1995).

[69]   G. P. Agrawal, *Nonlinear Fiber Optics* (Academic Press, San Diego, 1989).

[70]   M. Remoissenet, *Waves called solitons: concepts and experiments* (Springer-Verlag, Berlin, 1996).

[71]   P. St. J. Russell, "Optics of Floquet-Bloch waves in dielectric gratings," Appl. Phys. B **B39**, 231 (1986).

[72]   P. St. J. Russell, "Interference of integrated Floquet-Bloch waves," Phys. Rev. A **33**, 3232 (1986).

[73]   H. S. Eisenberg, Y. Silberberg, R. Morandotti, and J. S. Aitchison, "Diffraction Management," Phys. Rev. Lett. **85**, 1863 (2000).

[74]   A. Yariv and P. Yeh, "Electromagnetic Propagation in Periodic Stratified Media. II. Birefringence, Phase Matching, and X-Ray Lasers," J. Opt. Soc. Am. **67**, 438 (1977).

[75]   D. Mandelik, H. S. Eisenberg, Y. Silberberg, R. Morandotti, and J. S. Aitchison, "Band-Gap Structure of Waveguide Arrays and Excitation of Floquet-Bloch Solitons," Phys. Rev. Lett. **90**, 053902 (2003).

[76]   D. Mandelik, H. S. Eisenberg, Y. Silberberg, R. Morandotti, and J. S. Aitchison, "Observation of Mutually Trapped Multiband Optical Breathers in Waveguide Arrays," Phys. Rev. Lett. **90,** 253902 (2003).

[77]   V. E. Zakharov and A. B. Shabat, "Exact theory of two-dimensional self-focusing and one-dimensional self-modulation of waves in nonlinear media," Sov. Phys. JETP **34**, 62 (1972).

[78]   V. E. Zakharov, "Stability of periodic waves of finite amplitude on the surface of a deep fluid," J. Appl. Mech. Tech. Phys. **9**, 506 (1967).

[79]   F. Lederer and J. S. Aitchison, "Discrete solitons in nonlinear waveguide arrays" in *Optical Solitons: Theoretical Challanges and Industrial Perspectives*, V. E. Zakharov and S. Wabnitz eds. (Springer, Berlin, 1998), p. 349-365.

[80]   F. Lederer, S. Darmanyan, and A. Kobyakov in Spatial Optical Solitons (eds. S. Trillo and W. E. Torruellas) (Springer-Verlag, New-York, 2001) pp. 269-292.

[81]   J. S. Aitchison, D. C. Hutchings, J. U. Kang, G. I. Stegeman, and A. Villeneuve, "The nonlinear optical properties of AlGaAs at the half band gap," IEEE J. Quantum Electron. **33**, 341 (1997).

[82] J. U. Kang, A. Villeneuve, M. Sheik-Bahae, G. I. Stegeman, K. Alhemyari, J. S. Aitchison, and C. N. Ironside, "Limitation due to three-photon absorption on the useful spectral range for nonlinear optics in AlGaAs below half band gap," Appl. Phys. Lett. **65**, 147 (1994).

[83] K. H. Park, M. W. Kim, Y. T. Byun, D. Woo, S. H. Kim, S. S. Choi, Y. Chung, W. R. Cho, S. H. Park, and U. Kim, 'Nondestructive propagation loss and facet reflectance measurements of GaAs/AlGaAs strip-loaded waveguides," J. Appl. Phys. **78**, 6318 (1995).

[84] D. G. Revin, L. R. Wilson, D. A. Carder, J. W. Cockburn, M. J. Steer, M. Hopkinson, R. Airey, M. Garcia, C. Sirtori, Y. Rouillard, D. Barate, and A Vicet, "Measurements of optical losses in mid-infrared semiconductor lasers using Fabry-Pérot transmission oscillations," J. Appl. Phys. **95**, 7584 (2004).

[85] A. E. Siegman, *Lasers* (University Science Books, Mill Valley, 1986).

[86] W. T. Silfvast., *Laser fundamentals* (Cambridge University Press, Cambridge, UK; New York, 2004).

[87] J. C. M. Diels, J. J. Fontaine, I. C. Mcmichael, and F. Simoni, "Control and measurement of ultrashort pulse shapes (in amplitude and phase) with femtosecond accuracy," Appl. Optics **24**, 1270 (1985).

[88] J. C. Diels, J. J. Fontaine, and W. Rudolph, "Ultrafast diagnostics," Rev Phys Appl **22**, 1605 (1987).

[89] N. G. Vakhitov, A. A. Kolokolov, "Stationary solutions of the wave equation in a medium with nonlinearity saturation," Izv. Vuz. Radiofiz. **16,** 1020 (1973) [English Translation: Radiophys. and Quant. Electronics **16**, 783 (1975).

[90] L. Bergè, "Wave collapse in physics: principles and applications to light and plasma waves", Phys. Rep. **303**, 259 (1998).

[91] J. B. Pendry, Focus issue: "Negative refraction and Metamaterials," Opt. Express **11**, 639 (2003).

[92] M. Notomi, "Theory of light propagation in strongly modulated photonic crystals: Refractionlike behavior in the vicinity of the photonic band gap," Phys. Rev. B **62**, 10696 (2000).

[93]   G. von Freymann, W. Koch, D. C. Meisel, M. Wegener, M. Diem, A. Garcia-Martin, S. Pereira, K. Busch, J. Schilling, R. B. Wehrspohn, and U. Gösele, "Diffraction properties of two-dimensional photonic crystals," Appl. Phys. Lett. **83**, 614 (2003).

[94]   R. Morandotti, U. Peschel, J. S. Aitchison, H. S. Eisenberg, and Y. Silberberg, "Experimental Observation of Linear and Nonlinear Optical Bloch Oscillations," Phys. Rev. Lett. **83**, 4756 (1999).

[95]   R. Iwanow, D. A. May-Arrioja, D. N. Christodoulides, G. I. Stegeman, Y-H. Min, and W. Sohler, "Discrete Talbot Effect," Phys. Rev. Lett. **95**, 053902 (2005).

[96]   U. Peschel, R. Morandotti, J. S. Aitchison, H. S. Eisenberg, and Y. Silberberg, "Nonlinearly induced escape from a defect state in waveguide arrays," Appl. Phys. Lett. **75**, 1348 (1999).

[97]   R. Morandotti, H. S. Eisenberg, D. Mandelik, Y. Silberberg, D. Modotto, M. Sorel, C. R. Stanley, and J. S. Aitchison "Interaction of discrete solitons with structural defects," Opt. Lett. **28**, 834 (2003).

[98]   H. Trompeter, U. Peschel, T. Pertsch, F. Lederer, U. Streppel, D. Michaelis, and A. Bräuer, "tailoring guided modes in waveguide arrays," Opt. Express **11**, 3404 (2003).

[99]   O. Cohen, T. Schwartz, J. W. Fleischer, M. Segev, and D. N. Christodoulides, "Multiband Vector Lattice Solitons," Phys. Rev. Lett. **91**, 113901 (2003).

[100] X. Wang, A. Bezryadina, Z. Chen, K. G. Makris, D. N. Christodoulides, and G. I. Stegeman, "Observation of Two-Dimensional Surface Solitons," Phys. Rev. Lett. **98,** 123903 (2007).

[101] A. Szameit, Y. V. Kartashov, F. Dreisow, T. Pertsch, S. Nolte, A. Tünnermann and L. Torner, "Observation of Two-Dimensional Surface Solitons in Asymmetric Waveguide Arrays," Phys. Rev. Lett. **98**, 173903 (2007).

[102] L.-L. Lin and Z.-Y. Li, "Interface states in photonic crystal heterostructures," Phys. Rev. B **63**, 033310 (2001).

[103] J. Hudock, "Optical wave propagation in discrete waveguide arrays," Ph.D. thesis, University of Central Florida digital library, 2005.

[104] J. Meier, J. Hudock, D. N. Christodoulides, G. I. Stegeman, Y. Silberberg, R. Morandotti, and J. S. Aitchison, "Discrete Vector Solitons in Kerr Nonlinear Waveguide Arrays," Phys. Rev. Lett. **91**, 143907 (2003).

[105]   J. Hudock, S. Suntsov, D. N. Christodoulides, and G. I. Stegeman, "Vector discrete nonlinear surface waves," Opt. Express **13**, 7720 (2005).